

EXPANDING THE FUNCTIONALITY AND APPLICATIONS OF  
NANOPORE SENSORS

Kimberly E. Venta

A DISSERTATION

in

Physics and Astronomy

Presented to the Faculties of the University of Pennsylvania in Partial  
Fulfillment of the Requirements for the Degree of Doctor of Philosophy

2014

---

Marija Drndić, Professor of Physics and Astronomy  
Supervisor of Dissertation

---

Marija Drndić, Professor of Physics and Astronomy  
Graduate Group Chairperson

Dissertation Committee:

Marija Drndić, Professor of Physics and Astronomy  
A. T. Charlie Johnson, Professor of Physics and Astronomy  
Randall Kamien, Professor of Physics and Astronomy  
Alison Sweeney, Assistant Professor of Physics and Astronomy  
Ravi Sheth, Professor of Physics and Astronomy

UMI Number: 3634218

All rights reserved

INFORMATION TO ALL USERS

The quality of this reproduction is dependent upon the quality of the copy submitted.

In the unlikely event that the author did not send a complete manuscript and there are missing pages, these will be noted. Also, if material had to be removed, a note will indicate the deletion.



UMI 3634218

Published by ProQuest LLC (2014). Copyright in the Dissertation held by the Author.

Microform Edition © ProQuest LLC.

All rights reserved. This work is protected against unauthorized copying under Title 17, United States Code



ProQuest LLC.  
789 East Eisenhower Parkway  
P.O. Box 1346  
Ann Arbor, MI 48106 - 1346

# Acknowledgements

I have been fortunate to have an amazing group of friends, family, and colleagues who have supported me and worked with me. I would like to thank my advisor, Dr. Marija Drndić, whose guidance and encouragement have made me a better scientist and teammate and who has taught me a great deal about all aspects of scientific work. I would also like to extend thanks to my dissertation committee, Dr. Charlie Johnson, Dr. Randall Kamien, Dr. Alison Sweeney, and Dr. Ravi Sheth, for taking time to help me graduate and for challenging me to improve.

I want to express my thanks to all members of the Drndić lab, past and present, that I have worked with because they have all been excellent collaborators, amazing teachers, and have generally brightened my days. In particular, Ken Healy responded to numerous requests for help with nanopores or computers, even when it was no longer required of him; Chris Merchant taught me about nanofabrication; Meni Wanunu introduced me to the basics of nanopores and gave me my first project; Gaby Shemer kept me calm when things weren't working; Julio Rodriguez-Manzo made me a much more advanced TEM user; Adrian Balan always reminded me to think of the electronics in the system; David Niedzwiecki taught me about the biological side of things; Jessamyn Fairfield talked with me on every topic from bathroom equality to which books belong in the top 100 Sci Fi/ Fantasy novels; Lauren Willis showed me

the ropes in the lab - all the ropes, including where the literal rope is located; Matt Puster bounced ideas around with me and made each day more interesting; and Will Parkin did all the computer programming and maintenance when I found it beyond my capabilities, without commenting on my abilities or the time it took him.

I am very grateful to my collaborators, including Dr. Ken Shepard and Dr. Jacob Rosenstein, who taught me everything I know about electrical engineering, and Mehdi Zanjani, who tirelessly simulated tweaks of the same system for me whenever I changed a parameter.

I would also like to thank everyone who gave me access to and help with the tools I needed, including Doug Yates and the NSF-MRSEC electron microscopy facility, and Kyle Keenan, Hiromichi Yamamoto, Iulian Codreanu, Eric Johnston, Noah Clay and the Wolf and Quattrone Nanofabrication Facilities, and Dr. Charlie Johnson and his lab, who graciously allowed me use of their equipment. The work presented here would not have been physically possible without their support. Many thanks to Jim Nixon, Millicent Minnick, Vivian Hasiuk, Helen Jackson, Jason Seta, and Rebecca Perry for making the practical side of research easier.

I want to thank my extended family, the Cochran clan, for their patience with me and for staying in touch despite the distance, and the Gratale/Mizzone family for giving me a family nearby.

My fiancé Matt Gratale has been there for me every step of the way for the past five years. Matt: thank you for everything. I hope to somehow repay you for all the

things you do for me, and I cannot wait to begin our life together in a few weeks.

This thesis is dedicated to my parents, Patrick Venta and Jeri Cochran. They have supported me the longest and the most, and I can never fully thank them for everything they have done for me.

## ABSTRACT

# EXPANDING THE FUNCTIONALITY AND APPLICATIONS OF NANOPORE SENSORS

Kimberly E. Venta

Dr. Marija Drndić

Nanopore sensors have developed into powerful tools for single-molecule studies since their inception two decades ago. Nanopore sensors function as nanoscale Coulter counters, by monitoring ionic current modulations as particles pass through a nanopore. While nanopore sensors can be used to study any nanoscale particle, their most notable application is as a low cost, fast alternative to current DNA sequencing technologies. In recent years, significant progress has been made toward the goal of nanopore-based DNA sequencing, which requires an ambitious combination of a low-noise and high-bandwidth nanopore measurement system and spatial resolution. In this dissertation, nanopore sensors in thin membranes are developed to improve dimensional resolution, and these membranes are used in parallel with a high-bandwidth amplifier. Using this nanopore sensor system, the signals of three DNA homopolymers are differentiated for the first time in solid-state nanopores. The nanopore noise is also reduced through the addition of a layer of SU8, a spin-on polymer, to the supporting chip structure. By increasing the temporal and spatial resolution of nanopore sensors, studies of shorter molecules are now possible. Nanopore sensors are beginning

to be used for the study and characterization of nanoparticles. Nanoparticles have found many uses from biomedical imaging to next-generation solar cells. However, further insights into the formation and characterization of nanoparticles would aid in developing improved synthesis methods leading to more effective and customizable nanoparticles. This dissertation presents two methods of employing nanopore sensors to benefit nanoparticle characterization and fabrication. Nanopores were used to study the formation of individual nanoparticles and serve as nanoparticle growth templates that could be exploited to create custom nanoparticle arrays. Additionally, nanopore sensors were used to characterize the surface charge density of anisotropic nanopores, which previously could not be reliably measured. Current nanopore sensor resolution levels have facilitated innovative research on nanoscale systems, including studies of DNA and nanoparticle characterization. Further nanopore system improvements will enable vastly improved DNA sequencing capabilities and open the door to additional nanopore sensing applications.

# Contents

<b>Acknowledgements</b>	<b>ii</b>
<b>Abstract</b>	<b>v</b>
<b>List of Tables</b>	<b>x</b>
<b>List of Illustrations</b>	<b>xi</b>
<b>1 Introduction</b>	<b>1</b>
1.1 Nanopores . . . . .	1
1.2 Potential for Improvements in	
DNA Sequencing . . . . .	4
1.3 The Physics of (DNA) Translocations . . . . .	6
<b>2 Experimental Methods</b>	<b>11</b>
2.1 Nanopore Fabrication . . . . .	11
2.2 Measurement Setup and Electrical Tools . . . . .	15
<b>3 Pushing the Boundaries of Nanopore Detection</b>	<b>20</b>
3.1 Low-Volume Nanopores for Homopolymer	
Differentiation . . . . .	23

3.1.1	Introduction . . . . .	23
3.1.2	Comparison of Solid-State and Biological Pores . . . . .	24
3.1.3	Experimental Methods . . . . .	27
3.1.4	Electronic Characterization . . . . .	32
3.1.5	Analysis of Homopolymer Events . . . . .	35
3.1.6	Pores Too Small for ssDNA . . . . .	40
3.1.7	Summary . . . . .	40
3.2	Graphene as a Membrane Material . . . . .	42
3.2.1	Introduction . . . . .	42
3.2.2	Experimental Methods . . . . .	43
3.2.3	Measurements of Suspended Graphene Nanopores . . . . .	47
3.2.4	Addition of TiO <sub>2</sub> to Stabilize Membranes . . . . .	52
3.2.5	Summary . . . . .	62
3.3	Lowering Noise to Enable Increased Bandwidth . . . . .	63
3.3.1	Introduction . . . . .	63
3.3.2	Experimental Methods . . . . .	64
3.3.3	Capacitance and Noise Measurements . . . . .	67
3.3.4	Summary . . . . .	69
3.4	Conclusions . . . . .	70
<b>4</b>	<b>Nanopores for Nanoparticle Synthesis and Characterization</b>	<b>71</b>
4.1	Introduction to Nanoparticles . . . . .	71

4.2	Growing Nanoparticles using Nanopore Templates . . . . .	72
4.2.1	Introduction . . . . .	72
4.2.2	Overview of the Method . . . . .	74
4.2.3	Discussion of the Current Signals . . . . .	77
4.2.4	Proposition of a Growth Model . . . . .	81
4.2.5	Examining the Reaction Time Delay . . . . .	84
4.2.6	Effects of a Capping Agent . . . . .	85
4.2.7	Summary . . . . .	91
4.3	Nanoparticle Translocations . . . . .	92
4.3.1	Introduction . . . . .	92
4.3.2	Experimental Methods . . . . .	93
4.3.3	Crossover between Increasing and Decreasing Events . . . . .	101
4.3.4	Simulating Nanorod Translocations to Extract Charge . . . . .	106
4.3.5	Summary . . . . .	111
4.4	Conclusions . . . . .	112
<b>5</b>	<b>Appendix</b>	<b>114</b>
5.1	Resist-based Lithographies . . . . .	114
5.2	Plasma and Reaction Ion Etching . . . . .	119
5.3	STEM Thinning . . . . .	121
5.4	Atomic Layer Deposition . . . . .	122
5.5	Chemical Vapor Deposition . . . . .	124

# LIST OF TABLES

3.1	Comparison of solid-state and biological nanopores . . . . .	26
5.1	Photolithography and electron beam lithography recipes . . . . .	118
5.2	Recipes for plasma etching of silicon nitride . . . . .	120
5.3	Recipes for plasma etching of organics . . . . .	120
5.4	TEM settings for STEM thinning of silicon nitride membranes . . .	122
5.5	Recipe for atomic layer deposition of TiO <sub>2</sub> . . . . .	124
5.6	Recipe for chemical vapor deposition of graphene . . . . .	125

# LIST OF ILLUSTRATIONS

1.1.1 Schematic of a nanopore experiment . . . . .	2
1.2.1 Structure of the four bases of DNA and the DNA double helix . . . . .	3
1.3.1 Theoretical conductance for varying nanopore dimensions . . . . .	8
2.1.1 Membrane fabrication procedure . . . . .	12
2.2.1 Electronics and noise sources . . . . .	16
2.2.2 Chip capacitance dependence on assorted parameters . . . . .	19
3.0.1 Three main avenues to improve nanopore detection . . . . .	22
3.1.1 Comparison of solid-state and biological pores . . . . .	25
3.1.2 SiN <sub>x</sub> thinning calibration . . . . .	29
3.1.3 Views of a thinned membrane . . . . .	30
3.1.4 TEM images of sub-2 nm diameter nanopores . . . . .	30
3.1.5 Noise characterization . . . . .	33
3.1.6 Power spectral densities of various nanopores . . . . .	34
3.1.7 Histograms and example events for homopolymers . . . . .	36
3.1.8 Histograms of homopolymer event duration . . . . .	38

3.1.9	Percent of the open pore current blocked by homopolymers . . . . .	39
3.1.10	Current trace for a pore too small for translocations . . . . .	41
3.2.1	Graphene nanopore experimental setup . . . . .	45
3.2.2	Characterization of CVD grown graphene . . . . .	45
3.2.3	Graphene suspended over SiN <sub>x</sub> hole . . . . .	46
3.2.4	Characterization of graphene pinholes . . . . .	47
3.2.5	Equivalence circuit of graphene membranes with pinholes . . . . .	48
3.2.6	Measurement of DNA translocation with graphene nanopores . . . . .	49
3.2.7	Time trace of ionic current before and after DNA addition . . . . .	49
3.2.8	DNA translocation through a SiN <sub>x</sub> nanopore . . . . .	50
3.2.9	Characterization of TiO <sub>2</sub> -covered graphene nanopores . . . . .	53
3.2.10	TEM image of crystallized TiO <sub>2</sub> around a nanopore . . . . .	53
3.2.11	Current vs time traces of DNA translocation for TiO <sub>2</sub> -covered graphene nanopores . . . . .	56
3.2.12	Example events through TiO <sub>2</sub> -covered nanopores . . . . .	58
3.2.13	Characterization of translocation events . . . . .	60
3.2.14	Ionic current distributions for varying applied voltage . . . . .	61
3.2.15	Event lengths as a function of $V_B$ . . . . .	61
3.3.1	Theoretical SU8-coated device capacitance . . . . .	65
3.3.2	Optical image of an SU8-coated nanopore chip . . . . .	66
3.3.3	Capacitance measurements of SU8-coated nanopore devices . . . . .	68

3.3.4 Noise measurements of an SU8-coated nanopore device . . . . .	69
4.2.1 Process for synthesizing nanoparticles inside nanopores . . . . .	75
4.2.2 Reaction rate as a function of gold chloride concentration . . . . .	77
4.2.3 Control traces without all reagents present . . . . .	78
4.2.4 Ionic current signals characterizing nanoparticle formation . . . . .	79
4.2.5 Fitting Richard's model growth to experimental results . . . . .	84
4.2.6 Effect of salt concentration on time delay . . . . .	86
4.2.7 Lack of a trend between pore diameter and delay time . . . . .	86
4.2.8 Ionic current output during particle formation in the presence of $\alpha$ -lipoic acid . . . . .	87
4.2.9 TEM images of nanoparticles synthesized under varying conditions .	88
4.2.10 High salt gold aggregates . . . . .	89
4.2.11 Determination of lattice spacing in a synthesized nanoparticle . . . . .	90
4.2.12 TEM profiles indicate the nanoparticle is confined to the nanopore .	90
4.3.1 Characterization of nanorod translocation experiment . . . . .	96
4.3.2 Electrical output from nanorod translocation experiments . . . . .	97
4.3.3 Nanorod absorbance at varying salt concentrations . . . . .	98
4.3.4 Histograms of nanorod dimensions . . . . .	99
4.3.5 Crossover from increasing to decreasing current events as nanopore diameter increases . . . . .	104
4.3.6 Measurement of the nanopore surface charge density . . . . .	107

4.3.7	Event duration as a function of nanorod length . . . . .	108
4.3.8	Simulation of nanorod translocations . . . . .	109
5.1.1	Schematic of resist-based lithography process . . . . .	117
5.2.1	Schematic of the plasma etching process . . . . .	120
5.4.1	Diagram of the growth procedure in ALD . . . . .	123

# CHAPTER 1

## Introduction

The research discussed in this dissertation centers around nanopore sensors. Specifically, two themes are discussed: increasing the sensitivity of nanopore sensors and expanding the application of nanopore sensors to the study of nanoparticles. To address the first point, experimental results are included that characterize nanopore sensors made with novel thin materials such as graphene and thinned silicon nitride and the results of the use of such nanopores to differentiate between homopolymers. The second point is illustrated with experimental results of nanoparticle formation inside nanopores as well as nanorod translocation through nanopores. These results suggest researchers are only beginning to tap the potential of nanopore sensors.

### 1.1 Nanopores

Nanopore sensors are at their simplest Coulter-counters created on nanometer length scales.<sup>21</sup> Figure 1.1.1 gives an outline of a nanopore experimental setup. A single pore is formed in a thin membrane, and that membrane is placed to separate two chambers of ionic solution so that the only path between the two chambers is through the pore (Figure 1.1.1a). When a voltage bias is applied between the two chambers and the

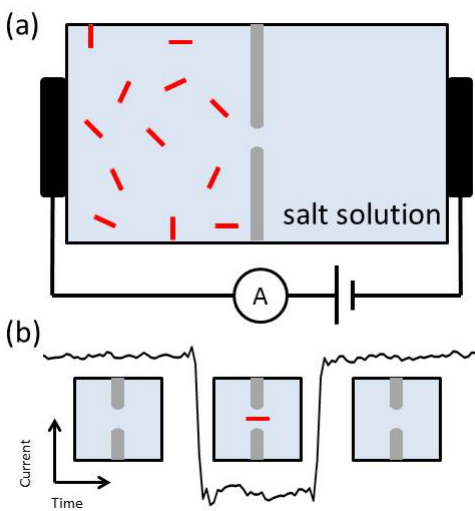


Figure 1.1.1: (a) Schematic of the experimental setup in a nanopore experiment. A nanometer-sized pore in a thin membrane is placed to separate two chambers of saline solution. A potential bias is applied across the pore, and the current is monitored using Ag/AgCl electrodes. If charged particles are introduced to the system, they can be pulled through the pore by the potential, causing a change in the measured current. (b) Schematic of the output current versus time from a nanopore experiment. The insets illustrate the plateau correspondence to particle translocation. Initially (far left), the nanopore is open and ions flow freely between chambers, creating a steady state open pore current. When a particle enters the pore (center), the current density in the pore changes (in this example, it decreases), and a change in the output current is observed. After the particle exits the pore (far right), the current returns to its open pore value.

resulting ionic current is measured, a steady state current is observed. If charged particles are introduced into the system, they can be pulled through the pore by the voltage bias. As they pass through the pore, or translocate, the current density in the pore changes noticeably (Figure 1.1.1b). These current changes, or events, contain information on the particles dimensions and charges.

Nanopores have proven to be a unique and valuable tool for a variety of single-molecule studies.<sup>10,25–27,48,52,59,60,63,96,109,132,140</sup> To date, nanopores have resolved many details of DNA and RNA structure.<sup>2,59,140</sup> They can detect microRNAs,<sup>142</sup> discriminate between classes of nucleic acids,<sup>35,142</sup> detect DNA binding,<sup>68</sup> measure molecular

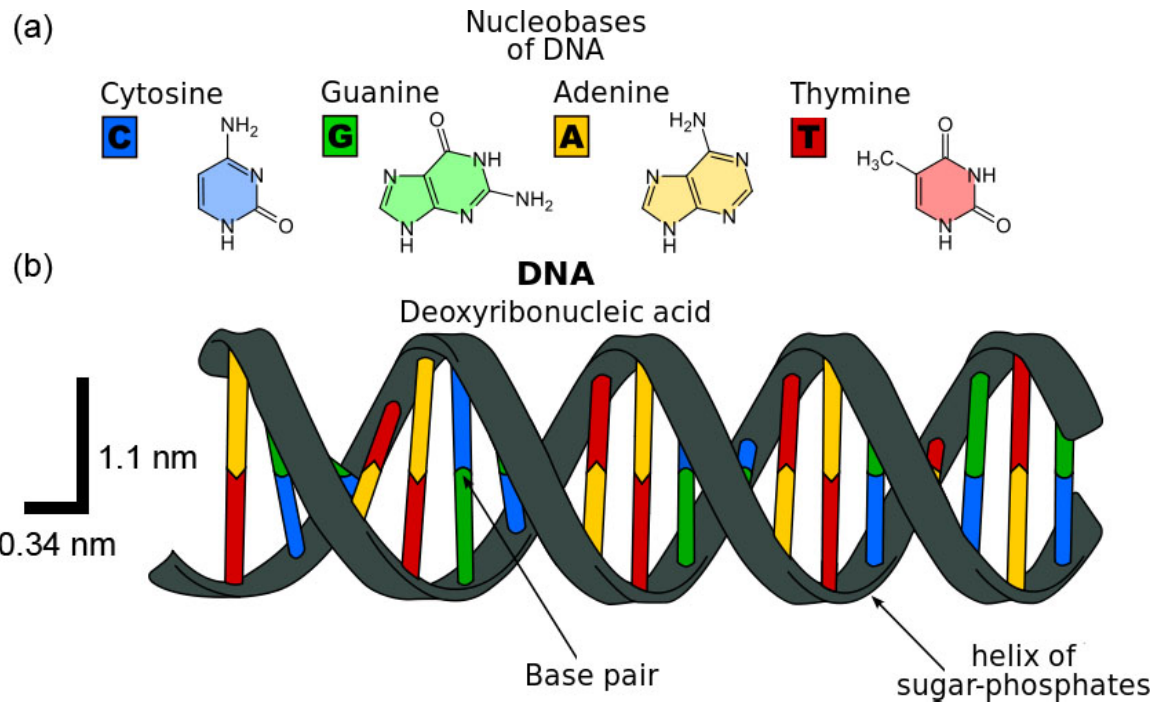


Figure 1.2.1: Structure of the four bases contained in DNA and the DNA double helix. (a) The chemical structures of the four nucleic acid bases in DNA. (b) DNA helical structure. A backbone of sugar-phosphates contains a string of nucleotides. Two of these strands pair up in a double helix - adenine pairs with thymine and cytosine pairs with guanine. Each base pair is separated by 0.34 nm, and the double helix has a diameter of 2.2 nm. Image credit: User:Sponk / Wikimedia Commons / CC-BY-SA-3.0

forces,<sup>30,64</sup> and detect various kinds of molecules such as the proteins that comprise anthrax toxin.<sup>43</sup> They are beginning to be used for the characterization of other proteins, as well.<sup>23,75,77,104</sup>

## 1.2 Potential for Improvements in DNA Sequencing

One clear application for nanopore sensors is DNA sequencing. DNA is a biopolymer composed of a string of nucleotides (adenine, thymine, cytosine, and guanine) connected through a sugar-phosphate backbone.<sup>84</sup> The diameter of double-stranded DNA (dsDNA) is 2.2 nm, and the spacing between bases on the DNA chain is 0.34 nm.<sup>84</sup> The chemical structure of the bases that distinguish the four nucleotides is shown in Figure 1.2.1. The structures are similar, and in the case of guanine and adenine the structure differs by only the placement of an amine group, and an extra oxygen atom and hydrogen atom in the guanine molecule. Because there are 3.2 billion bases in the human genome,<sup>101</sup> DNA sequencing methods must distinguish these sub-nanometer differences between nucleotides in a biopolymer strand that is roughly one meter long.

Sanger sequencing has been the standard sequencing method for decades.<sup>115</sup> In Sanger sequencing, a DNA fragment is sequenced from millions of identical copies of the same DNA, produced either by cloning or amplification through the polymerase chain reaction (PCR). The identical DNA fragments are added to a solution that contains all the ingredients for DNA replication as well as modified versions of each of the four nucleotides, called chain termination nucleotides, that are uniquely tagged and terminate DNA replication. As replication proceeds, these modified nucleotides are

incorporated into the new DNA fragments at specific bases, but randomly along the length of the DNA, resulting in a solution of DNA fragments that are randomly terminated and tagged with the final base incorporated. When this solution is run through a polyacrylamide gel with an applied voltage, shorter strands travel farther through the gel. The DNA fragments are thus sorted by length, and the DNA sequence can be read by examining the tag, commonly a fluorescent tag of a different color for each of the four bases, on each fragment's terminating base. This process is repeated on many DNA fragments that have been randomly sheared from the original genome of an organism, and computer algorithms are used to piece together the entire genome from the sequence of each fragment. Although higher throughput methodologies have developed that have largely supplanted Sanger sequencing for the production of whole genome sequences, these methods still have substantial limitations.<sup>88,89</sup>

Affordable DNA sequencing has long been a challenge for both researchers and the public. While sequencing costs have decreased significantly since the completion of the Human Genome Project, which sequenced an entire human genome for 2.7 billion dollars, costs still remain too high for personal health diagnostics, at \$4,000 per genome.<sup>101</sup> Researchers have been developing nanopore sensors as an alternative to traditional DNA sequencing methods<sup>10,25–27,48,52,59,60,63,96,132,140</sup> because their thin detection region allows near-single base detection,<sup>19,87</sup> the detection mechanism does not rely on costly chemical labels, and in theory the DNA does not need to be copied.

## 1.3 The Physics of (DNA) Translocations

The physics of nanopore translocations depends on a variety of parameters, most notably the diameter, length, hydrophobicity, and surface charge density of both the nanopore and translocating particle, the concentration and molecular size of the ions in solution, and the applied bias across the nanopore. In the case of biomolecules, the conformation of the biomolecule also plays a role. This section will focus on dsDNA translocations, because they have been studied in greater depth than other molecules. For a discussion of single-stranded DNA (ssDNA) translocations, see Section 3.1, and for a discussion of nanorod translocation dynamics, see Section 4.3.

The ionic current through the empty pore (open pore current) is affected by the conductivity of the solution ( $\sigma_{solution}$ ) and the thickness ( $l$ ), radius ( $r$ ), and surface charge density on the nanopore ( $\sigma_{pore}$ ). Because the nanopore acts as a resistor, the conductance of an idealized pore is given by the formula  $G = \sigma\pi r^2/l$ . However, the silicon nitride nanopores used in these studies have a measured surface charge density of  $-23 \text{ mC/m}^2$  after piranha treatment, which matches well with published values.<sup>124</sup> At such small dimensions the solution conductivity in the nanopore differs from the bulk solution conductivity due to the electrical double layer on the charged nanopore surface. This electrical double layer is a region near a charged surface in ionic solution containing increased counterions and depleted co-ions. The distance from the charged surface over which this effect dominates before counterions screen the excess charge

is called the Debye length,  $\lambda_D$ . At room temperature (25°C) in KCl solution, the formula for the Debye length can be approximated by:

$$\lambda_D(nm) = \frac{0.304}{\sqrt{I(M)}} \quad (1.1)$$

Where  $\lambda_D(nm)$  is the Debye length in nanometers and  $I(M)$  is the ionic molar concentration. At standard KCl concentrations of 1 M and average nanopore diameters (5 to 10 nm), the Debye length is 0.3 nm and the ionic concentration inside the nanopore is approximately the same as the bulk ionic concentration. At low salts and small nanopore diameters, the Debye layers of the opposing nanopore walls begin to overlap. For example, in 100 mM KCl solution, the Debye length is  $\sim 1$  nm, and 2 nm diameter nanopores have increased ionic concentration compared to bulk solution. In this regime, the only charge carrier that can pass through the nanopore is the counterion. Due to the negative charge on the nanopore walls, the electrical double layer is composed of potassium ions, and an additional surface current term is added to the equation for nanopore conductance:<sup>121</sup>

$$G = \frac{\pi d^2}{4l} \left( \sigma_{solution} + \mu_K \frac{4\sigma_{pore}}{d} \right) \quad (1.2)$$

Here,  $d$  is the nanopore diameter and  $\mu_K$  is the mobility of potassium ions. In positively charged nanopores,  $\mu_K$  in this formula would be replaced with  $\mu_{Cl^-}$ , as the negatively charged  $Cl^-$  would be attracted to the pore walls and contribute to the surface current. Figure 1.3.1 shows the theoretical open pore conductance for

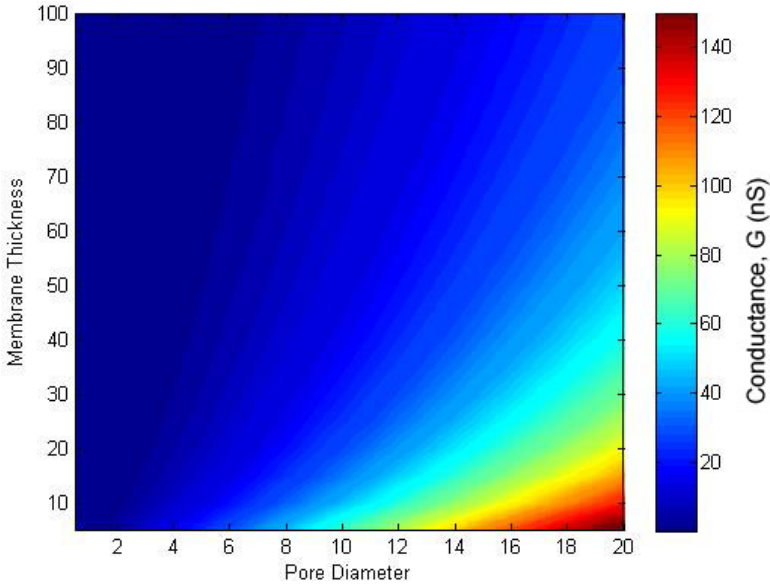


Figure 1.3.1: Theoretical nanopore conductance for varying nanopore dimensions. Equation 1.2 was used to produce this plot.

nano pores as the nanopore diameter and thickness changes.

When DNA enters the nanopore, it displaces ions that would have contributed to the open pore current, and adds its own effective current. Because DNA has a relatively low volume charge density of  $1.5 \text{ e}^-/\text{nm}^3$ , translocation events generally appear as dips in the ionic current. Only at low salt concentrations does the presence of DNA in the nanopore increase the ionic current.<sup>121</sup> Further, because the nanopore conductance depends on the nanopore membrane thickness, as in the case of a simple resistor, the change in current as DNA passes through the pore is larger in magnitude in thinner nanopores,<sup>135,142</sup>  $\Delta G = \sigma\pi(r_{pore}^2 - r_{DNA}^2)/l$ .

For the purposes of this work, DNA is pulled through a nanopore by the electromagnetic force experienced by the negative charges on its backbone due to the potential bias across the nanopore, although research groups have also used pressure,<sup>85</sup> salt gradients,<sup>143</sup> and diffusion<sup>103</sup> to drive DNA through a nanopore. The

electric field potential is concentrated near the nanopore and dissipates radially with distance from the nanopore. Due to this electric focusing, most of the motion of the DNA in solution is diffusion-dominated. Only when DNA drifts within an effective capture radius does the electric force dominate. This radius is thus the distance from the pore where the electric potential energy due to the applied bias is equal to the energy of the diffusive motion of the DNA.<sup>143</sup>

DNA typically travels very quickly through a nanopore, with dwell times between 16 and 50 ns/base.<sup>127</sup> The DNA length, applied voltage, and nanopore dimensions all play a role in this velocity. The nanopore dimensions control the electric field strength inside the pore, and combined with the applied voltage, control the driving force on the DNA molecule. The translocation time is found to follow a power law relative to the DNA length due to the hydrodynamic drag on the DNA molecule.<sup>127</sup> But for any reasonable experimental parameters, the order of magnitude remains too high for DNA sequencing with present amplifier capabilities. Many researchers have attempted to slow DNA down. The addition of glycerin to the ionic solution,<sup>62,86</sup> the exchange of heavier ions for ionic solution,<sup>69</sup> lowered temperatures,<sup>149</sup> functionalized nanopores,<sup>74,146</sup> and the use of a salt gradient across the nanopore<sup>143</sup> have all been tried with some success. The difficulty with these methods is that while the DNA velocity is reduced during translocation, the system noise is increased, which mitigates the information gained from the reduced speed.

Two methods can significantly increase the dwell time of DNA inside a nanopore.

The use of optical tweezers can slow down, and even pause, DNA translocation,<sup>64</sup> and the use of a DNA polymerase to control DNA translocation reduces the DNA velocity to  $\sim 60$  bases/s.<sup>87</sup> This extra time allows the collection of many more data points per base, which translates to more accurate base recognition.

# CHAPTER 2

## Experimental Methods

### 2.1 Nanopore Fabrication

Nanopore membrane fabrication begins with a five-layer wafer structure. Four inch diameter silicon wafers with 5  $\mu\text{m}$  wet thermal silicon dioxide deposited on either side were ordered from Nova Electronic Materials. The silicon was 50  $\mu\text{m}$  thick, aligned so that the top and bottom surfaces are normal to the  $<100>$  lattice plane, and phosphorus doped to achieve 1 – 10  $\Omega\text{cm}$  resistivity. Silicon dioxide was added as a thick insulating layer to reduce the chip noise and capacitance. These wafers were then sent to Cornell Nanoscale Facility for deposition of low-stress silicon nitride ( $\text{SiN}_x$ ). Wafers were ordered with silicon nitride thicknesses of either 25 nm, 50 nm, or 100 nm. Figure 2.1.1 shows the fabrication process, beginning with the unaltered wafers in Figure 2.1.1a.

To create suspended silicon nitride membranes, each of the four other wafer layers must be etched in turn, beginning with the silicon nitride layer opposing the membrane layer. S1818 resist (Dow Chemical) was spun on the membrane side of the wafer to protect it from processing, and either Futurrex NR7 (Futurrex) or AZ 5214-E resist (MicroChemicals) was spun on the side of the wafer to be etched (Figure

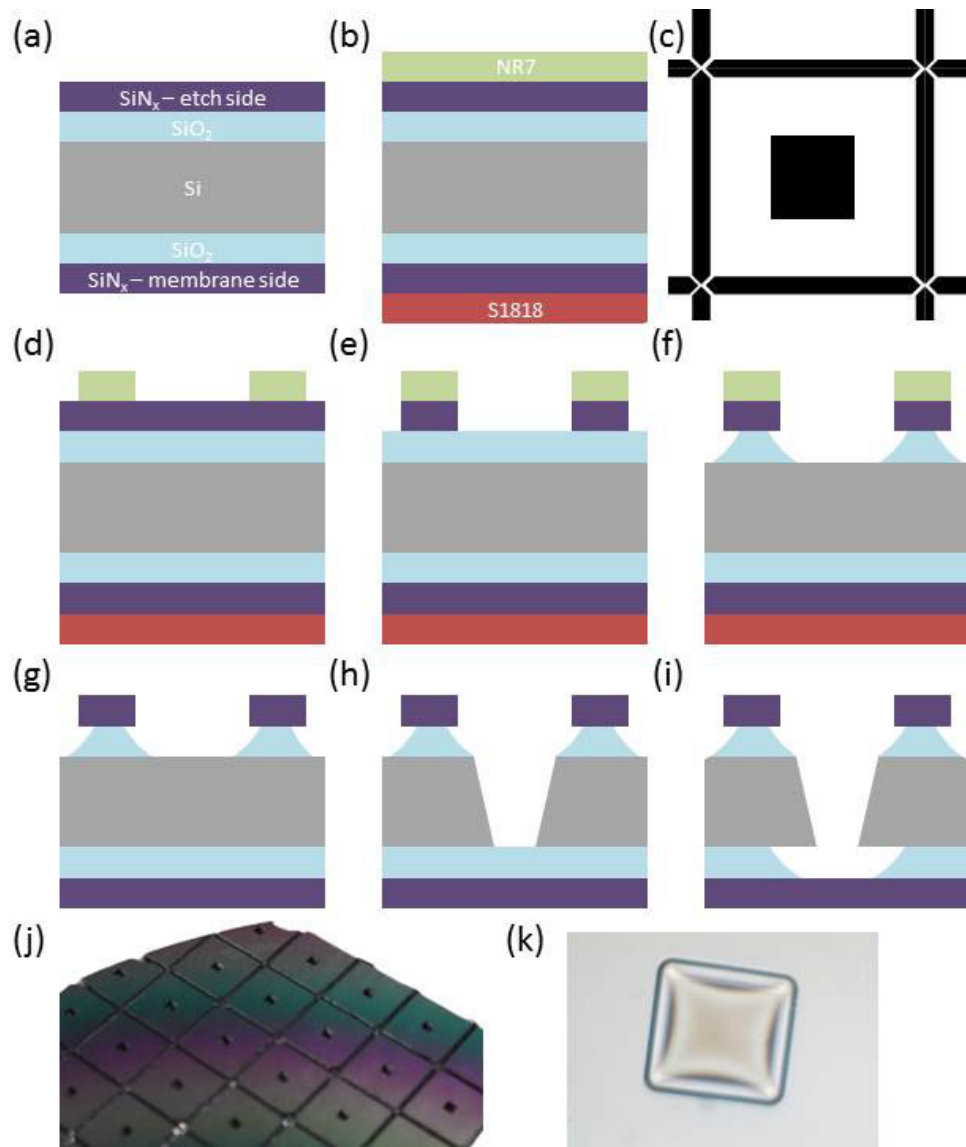


Figure 2.1.1: Membrane fabrication procedure. Membrane fabrication procedure begins with (a) a five layer wafer structure: 25 to 100 nm of silicon nitride surrounding 5  $\mu\text{m}$  silicon dioxide surrounding 500  $\mu\text{m}$  silicon. (b) resist is spun on both sides of the membrane for protection and patterning. The resist on the back side of the wafer is exposed to the pattern shown in (c) and developed to achieve the schematic shown in (d). (e) The back side silicon nitride layer is etched with plasma. (f) The first silicon dioxide layer is etched with BOE. (g) The resists are removed. (h) The silicon is etched in KOH. (i) The second silicon dioxide is etched in BOE. The final membranes, as they appear from the back side (j) and microscopically from the membrane side (k).

2.1.1b). The resist was exposed through a chrome photolithography mask to create a pattern of large squares and chip dividing lines, as shown in Figure 2.1.1c, then baked and developed to remove the unexposed resist (Figure 2.1.1d). The masks are designed to create either 10  $\mu\text{m}$  by 10  $\mu\text{m}$  or 50  $\mu\text{m}$  by 50  $\mu\text{m}$  membranes. The silicon nitride layer was directionally etched using plasma etching in either a Technics Planar Etch II or PlasmaLab 80+ (Figure 2.1.1e). The silicon dioxide was isotropically etched in buffered oxide etch (BOE, 6:1 volume ratio of 40%  $\text{NH}_4\text{F}$  in water to 49% HF in water) solution for 70 minutes (Figure 2.1.1f). The resists on both the etched and membrane sides of the wafer were then removed with Microposit Remover 1165 followed by cleaning in heated Cyantek Nano Strip (Figure 2.1.1g). The silicon was etched in 40% by weight potassium hydroxide (KOH) solution heated to 62°C. KOH etches silicon preferentially in the <100> direction, resulting in an inverted pyramidal structure with a slope of 54.7°. This preferential etching also makes the silicon etching a slightly self-limiting reaction, as once the patterned volume of silicon is etched, the KOH must etch in the slower <111> direction to increase the membrane size. Due to slight variations in the initial patterning exposure and KOH concentration, this etching can take between 20 and 24 hours, and is terminated when light is visible through the etched membranes. The wafer now looks like the schematic in Figure 2.1.1h. A final BOE etch is performed, with Shipley S1818 resist again spun on the membrane side of the wafer to protect it. This second BOE etch is 30% longer than the first to allow the hydrofluoric acid (HF) molecules to penetrate the deep trenches

in the wafer. After removing the resist as described above, the wafer now contains hundreds of suspended silicon nitride membranes, depicted schematically in Figure 2.1.1i and imaged in Figure 2.1.1j and 2.1.1k.

Nanopores were drilled in these membranes in a JEOL 2010F field emission transmission electron microscope (TEM). By condensing the electron beam at high magnification, the silicon nitride is ablated and a pore is formed.<sup>125</sup> In thin materials (thinned silicon nitride or graphene), this process can be slowed and controlled by reducing the current density of the electron beam with a higher spot size and smaller condenser aperture.

For some experiments, regions of the suspended silicon nitride membrane were thinned (see Section 3.1, Section 3.3 and Section 4.2). In Section 3.1 and Section 4.2, thinning was accomplished by patterning a 200 nm x 200 nm square using electron beam lithography, then etching the exposed square using plasma etching. The resist was removed before testing. In Section 3.3, membranes were either thinned using this method or by atomic ablation using scanning tunneling microscopy (STEM). In this method, the membrane is imaged in dark field STEM at the highest current settings listed in the JEOL 2010F manual. The high electron current density removes atoms from the membrane, and creates a thinned square as the electron beam rasters.

Unless otherwise noted, all nanopore devices were cleaned using hot piranha solution (3:1 sulfuric acid:35% hydrogen peroxide) followed by repeated water rinsing before testing. This both removes contaminants and makes the silicon nitride hy-

drophilic by attaching  $\text{OH}^-$  groups to silicon atoms. Increased hydrophilicity allows better solution flow through the nanopore. Additionally, for all experiments presented herein, KCl in water was used as the ionic current medium.

## 2.2 Measurement Setup and Electrical Tools

The noise in nanopore measurements primarily comes from three sources: the amplifier electronics, the nanopore device, and the surrounding environment. Figure 2.2.1a shows the general components of the nanopore experimental setup, Figure 2.2.1b shows a power spectral density (PSD) graph for a low-noise system below, with common noise signatures shown in red, and above shows the cumulative integrated power spectral density. The power spectral density is the Fourier transform of the autocorrelation function of the ionic current and gives a measure of the “power” of the current noise as a function of frequency. The cumulative integral of the power spectral density gives the expected root-mean-square (rms) noise when measuring at a given bandwidth.

Standard American electronics operate at a frequency of 60 Hz. Thus all electronics near the measurement setup can couple 60 Hz noise into the system, including the room lighting. A 60 Hz noise spike will be seen in a poorly shielded system. This noise can be eliminated by surrounding the nanopore system in a Faraday box, and isolating the Faraday box from ground using an optical table. The box used in early experiments (Section 3.2 and Section 4.2) is made of 2 mm thick steel. Later

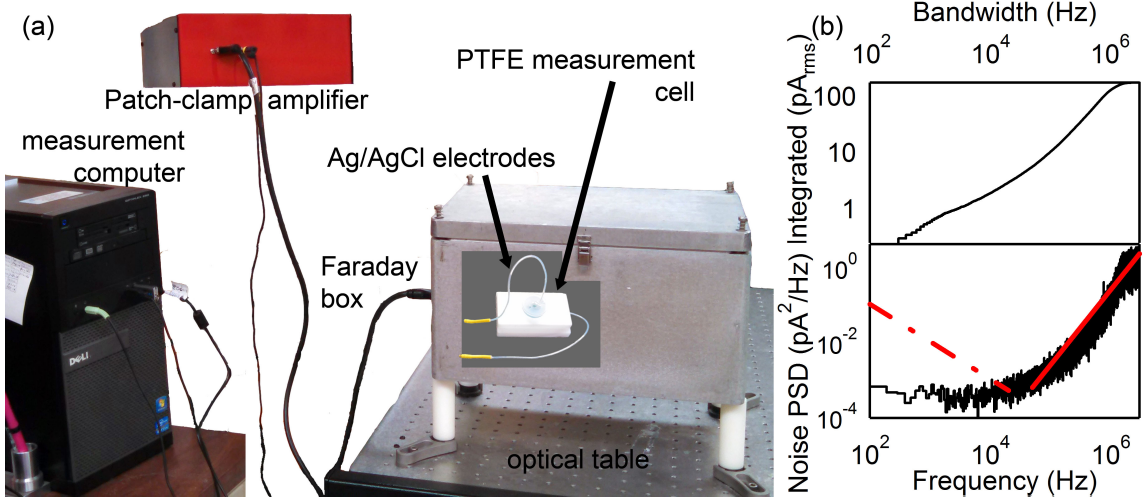


Figure 2.2.1: (a) The electronic and noise-cancelling system components. The nanopore setup consists of a patch-clamp amplifier that applies a voltage to the system and measures the output current, a measurement computer to acquire and analyze the data, a Faraday box and optical table to reduce vibrational and electronic noise, and a measurement cell with Ag/AgCl electrodes. (b) The bottom graph shows the power spectral density for a low-noise system. Common noise signatures found in nanopore experiments include  $1/f$  noise (red dashed line) due to poor wetting, 60 Hz noise due to improper shielding, and  $f^2$  noise (red solid line) due to capacitive feedback in the amplifier and across the nanopore chip. The cumulative integral of the PSD shown above gives the expected rms noise at a particular bandwidth.

experiments (Section 3.1, Section 3.3 and Section 4.3) employed a 7 mm thick cast aluminum box. Cast aluminum was chosen for its high purity and low resistivity, and the thickness was chosen to be thick enough for good electrical isolation, but lightweight enough so that it could be suspend on an optical table.

There is intrinsic noise associated with any patch-clamp amplifier that appears as high frequency noise proportional to  $f^2$ .<sup>117</sup> This is due to amplifier feedback. Patch-clamp amplifier electronics contain a voltage noise density that appears at the system input along with the program voltage, so that the voltage applied to the nanopore

system is in reality  $V_{program} + V_{noise}$ . Because the nanopore chip acts as a capacitor, when this voltage noise crosses the nanopore it is converted to current noise as shown in Equation 4.4. For higher frequencies of voltage noise, the current noise will reflect a proportionately larger response.

$$I(t) = \frac{dQ(t)}{dt} = \frac{CdV(t)}{dt} \quad (2.1)$$

The nanopores themselves contribute noise in two ways: low frequency  $1/f$  noise can appear due to poor pore wetting which reduces the number of mobile charge carriers along the surface<sup>51</sup> (drawn as a dashed line in Figure 2.2.1b), and high frequency  $f^2$  noise can appear due to capacitance through the nanopore chip (drawn as a solid line in Figure 2.2.1b). The nanopore chips fabricated as described in Section 2.1 have a capacitance on the order of tens of picoFarads. The theoretical capacitance for a variety of nanopore chip parameters is shown in Figure 2.2.2. The major contribution to nanopore capacitance comes from the large area of the supporting structure exposed to solution. The silicon support acts as a conductor, so the effective dielectric thickness of the nanopore chip comes from the 5  $\mu\text{m}$  of silicon dioxide layer added to reduce capacitance. Ecoflex 5 silicone elastomer is painted on the chip surface to minimize the exposed area, but the control over hand painting limits the exposed radius to approximately 0.5 mm. The membrane size and silicon nitride thickness have a smaller contribution to the chip capacitance.

The measurement cell can also add to the system noise through electrical cou-

pling or through series resistance. Two measurement cells were used here, one made of polytetrafluoroethylene (PTFE) and one made of polydimethylsiloxane (PDMS). Both employed a bottom fluid channel and a top close-contact chamber, with the nanopore sealed between the two with silicone elastomer. Electrical coupling can occur when condensation on the measurement cell contacts nearby electronics, creating a bridge of ionic solution to the nanopore system. The Ag/AgCl electrodes are inserted into the solution of each chamber, but their distance from the nanopore creates a series resistance through the solution. To minimize this, electrodes were placed close to the nanopore chip. In this configuration, the series resistance through the ionic solution was found to be  $15\text{ k}\Omega$ .

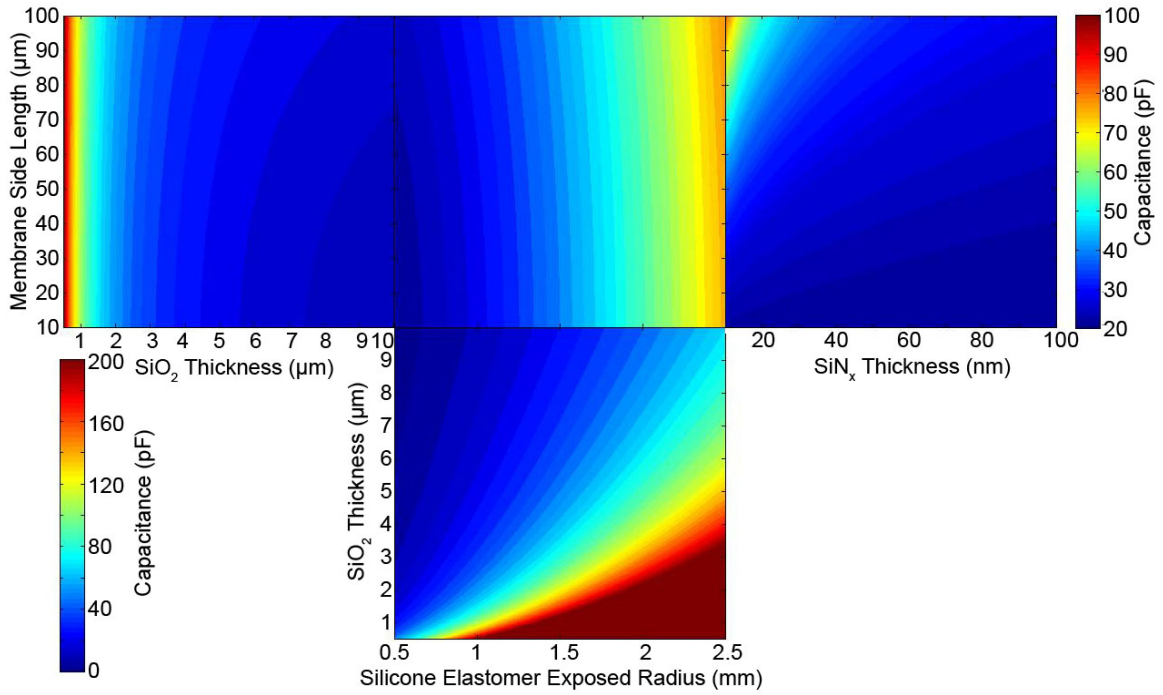


Figure 2.2.2: Nanopore chip capacitance as a function of  $\text{SiO}_2$  thickness, membrane size, silicone elastomer radius, and silicon nitride thickness. Capacitance was calculated by dividing the chip schematic into parallel and series capacitors, and any part of the chip covered with silicone elastomer was assumed to contribute no capacitance. The left three plots use the scale bar on the left. Because silicon nitride thickness and membrane size affect the capacitance less, the right plot uses the scale bar shown on the right. The parameters that were not varied assumed 1 mm radius of silicone elastomer, a membrane size of 10  $\mu\text{m}$  by 10  $\mu\text{m}$ , a 5  $\mu\text{m}$  thick layer of  $\text{SiO}_2$ , and an 85 nm thick layer of  $\text{SiN}_x$ .

# CHAPTER 3

## Pushing the Boundaries of Nanopore Detection

By increasing the detecting abilities of solid-state nanopores, not only can DNA sequencing be achieved, but a new myriad of experimental studies and practical applications become possible. Currently, to the author's knowledge, the shortest particle detected by a nanopore is  $\sim 10$  nm long.<sup>142</sup> If the detection region of a pore had increased sensitivity so that shorter particles were detectable, protein modification, folding, and dynamics could be studied with nanopores and small nanoparticle spheres could be characterized. For DNA sequencing, the nanopore detection region must contain only a single base at a time (see Figure 3.0.1a). If more than one base is detected simultaneously, the number of differentiable signals necessary for sequencing increases. For example, there are four possible signals from a single base (A, T, C, or G), and ten possible signals from two bases (AA, AT, AC, AG, TT, TC, TG, CC, CG, GG). Researchers can now distinguish between the ionic signals of the four nucleotides.<sup>87</sup> If  $\sim 20$  signals could be distinguished, nanopores could begin sequencing proteins, which are biopolymers composed of chains of amino acid residues, of which there are  $\sim 20$  common varieties, and thicker nanopore sequencers would be allowable

(see Figure 3.0.1b). Another avenue to improved nanopore detection is in time resolution. Biopolymers pass through nanoparticles at such high velocities that traditional measurement bandwidths are too low to sample each monomer (see Figure 3.0.1c). Although this temporal challenge can be overcome by slowing down translocating particles (see Section 1.3 for a complete discussion), this also increases experiment duration, and many methods for reducing particle velocity inside a nanopore also increase system noise. To avoid this issue, system noise can be decreased to allow faster signal acquisition.<sup>114</sup>

To probe these promising experimental regimes, thinner nanopores must be employed to allow a finer probe resolution, higher measurement bandwidths must be exploited, and system signal to noise ratio (SNR) must be reduced. As discussed in Section 1.3, thinner nanopores have higher current signals, and Section 2.2 discusses the possible methods of reducing noise. The following experiments use some of these methods to improve nanopore performance, the results of which brings these possible experiments closer to realization.

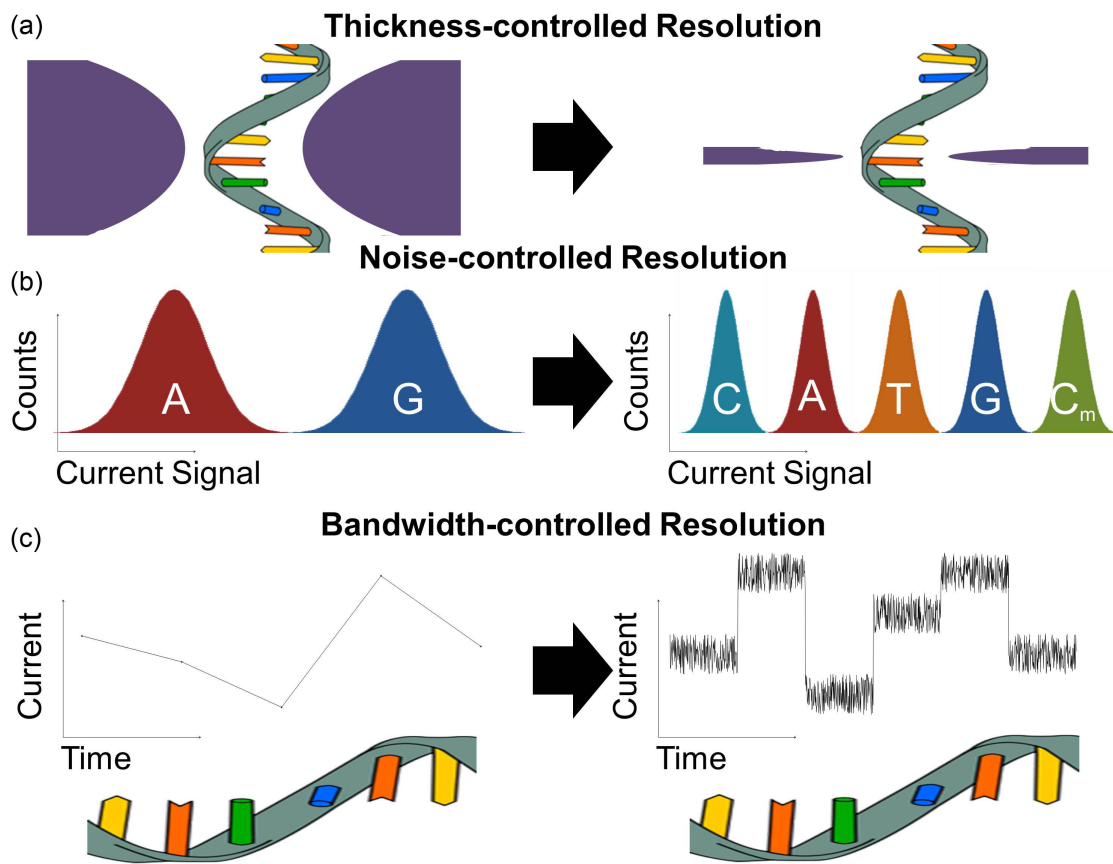


Figure 3.0.1: Three main avenues to improve nanopore detection are discussed. (a) Finer spatial resolution can be achieved by thinning the active detecting thickness of the pore. This is shown schematically as a purple nanopore that contains many (left) or a single (right) base depending on the nanopore membrane thickness. (b) Improved accuracy in discrimination between monomers can be achieved by lowering the system noise. When system noise is reduced, histograms of current levels become separated, so that more signal types can be detected, for example differentiating between two nucleotide types (left), or five (right). (c) Finer temporal resolution can be achieved by increasing the measurement bandwidth. When bandwidth is increased, more data points are achieved per spatial distance along the translocating molecule. This can mean the difference between not sampling each nucleotide on a DNA strand (left), and sampling many data points per nucleotide (right). Image credit: User:Sponk / Wikimedia Commons / CC-BY-SA-3.0

## 3.1 Low-Volume Nanopores for Homopolymer Differentiation

### 3.1.1 Introduction

Although nanopore sequencing has made a great deal of progress in recent years, the remaining challenges for both biological and solid-state nanopore-based sequencing are in spatial and temporal resolution. By combining ion channel proteins which have detecting regions less than 1.5 nm long with polymerase-based positional control, biological nanopores have recently demonstrated proof-of-principle DNA sequencing.<sup>17,87</sup> Proof-of-principle nanopore-based DNA sequencing-by-synthesis<sup>72</sup> based on single molecule mass spectroscopy<sup>110,113</sup> has also been demonstrated recently. Interest remains high to translate these successes to solid-state nanopores that offer the potential for easier manufacturability. The higher signal levels of solid-state nanopores may also make sequencing possible without enzymatic techniques to slow down translocation. This requires scaling the nanopores to sizes comparable to biological nanopores, while significantly improving detection electronics. For solid-state nanopores, previous work with sub-2 nm diameter nanopores has been largely limited to SiN<sub>x</sub> membranes with thicknesses  $\leq 10\text{nm}$ .<sup>20,49,50,153</sup> Only a few biomolecule translocation experiments have been reported on SiN<sub>x</sub> membranes with thicknesses  $\geq 10\text{nm}$ ,<sup>99,141,142</sup> but no solid-state nanopores have been reported that combine ultra-thin membranes

with nanopore diameters smaller than 2 nm.

This section demonstrates that small silicon nitride nanopores (0.8 to 2 nm diameter in 5 to 8 nm thick membranes) can resolve differences between ionic current signals produced by short (30 base) ssDNA homopolymers (poly(dA), poly(dC), poly(dT)), when combined with measurement electronics that allow a signal-to-noise ratio of better than 10 to be achieved at 1 MHz bandwidth. ssDNA translocations through nanopores of these dimensions transiently reduce the ionic conductance by up to 70 - 90%, similar to results from biological nanopores.<sup>26</sup> The reduced thickness of these nanopores leads to higher ionic conductances, increased bias current, and a reduction in the number of DNA bases present in the nanopore constriction. While identifying intramolecular DNA sequences with silicon nitride nanopores will require further improvements in nanopore sensitivity and noise levels, homopolymer differentiation represents an important milestone in the development of solid-state nanopores.

### 3.1.2 Comparison of Solid-State and Biological Pores

Since biological nanopores have been used to differentiate individual DNA bases within a specific DNA sequence or as part of homopolymers,<sup>2,80,81,87,92</sup> it is reasonable to expect that SiN<sub>x</sub> nanopores of similar dimensions may produce comparable results.

Figure 3.1.1a-c show an illustrated cross-section of a 1.2 nm diameter nanopore in a 5 nm thick SiN<sub>x</sub> membrane (Figure 3.1.1b), alongside cross-sections of  $\alpha$ -hemolysin ( $\alpha$ HL, Figure 3.1.1a) and MspA (Figure 3.1.1c) proteins.<sup>31,123</sup> All three are compa-

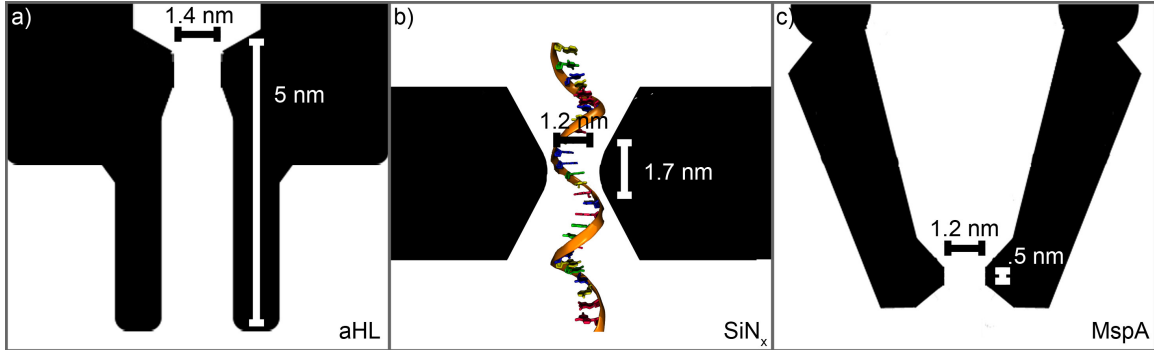


Figure 3.1.1: Comparison of the Si<sub>Nx</sub> nanopores presented here to biological nanopores. All images are on the same scale. (a) Biological nanopore  $\alpha$ -hemolysin ( $\alpha$ HL), which has a thickness of 5 nm and a diameter of 1.4 nm. (b) Representative dimensions of a Si<sub>Nx</sub> nanopore presented here. The nanopore shown is 1.2 nm in diameter and has an effective thickness ( $h_{eff}$ ) of 1.7 nm in a 5 nm thick membrane. The ssDNA is shown to scale. (c) Biological nanopore MspA, which has a thickness of 0.5 nm and a diameter of 1.2 nm.

rable in size, with small differences in diameter and thickness, as detailed in Table 3.1. The diameters of the solid-state nanopores presented here are comparable to both  $\alpha$ -hemolysin (1.4 nm) and MspA (1.2 nm), while the thickness is comparable to  $\alpha$ -hemolysin (5 nm) but thicker than MspA (0.5 nm).

The geometry of nanopores in solid-state membranes drilled using a transmission electron microscope (TEM) is governed by the interplay between surface tension of the molten Si<sub>Nx</sub> and its ablation kinetics.<sup>125</sup> This geometry can be modified by tuning the electron beam fabrication process.<sup>66,125,131</sup> Based on TEM imaging, ion conductance measurements,<sup>66</sup> and annular dark field scanning TEM (ADF-STEM) studies,<sup>142</sup> Si<sub>Nx</sub> nanopore shapes are known to deviate from a perfect cylinder. Electron tomography shows that 7 nm diameter Si<sub>Nx</sub> nanopores in 50 nm thick membranes have a truncated double-cone or hourglass structure.<sup>66</sup> Nevertheless, a simplified geometric

	$\alpha$ HL	MspA	$\text{SiN}_x$
Constriction Width (nm)	1.4 <sup>123</sup>	1.2 <sup>31</sup>	1-2
Constriction Height (nm)	5 <sup>123</sup>	0.6 <sup>31</sup>	5-8
Conductance (nS)	1 <sup>26,59</sup>	1.8 <sup>12</sup>	3-14
Signal Amplitude, $\Delta I$ (nA)	0.1-0.105 <sup>26</sup>	0.15-0.26 <sup>29,87</sup>	1-5
Operating Voltage (mV)	120	180	$\leq 1000$
Signal Conductance, $\Delta I/V$ (nS)	0.83-0.88	0.83-1.4	1-5
% Pore Blocked (%)	83-95 <sup>26</sup>	48-82 <sup>12,29,87</sup>	30-80
Nucleotide Signal Difference (pA)	5-15 <sup>26</sup>	6-11 <sup>29</sup>	200-900

Table 3.1: Comparison of physical properties and experimental results between the  $\text{SiN}_x$  nanopores presented here and published results for the two of the most commonly used biological nanopores:  $\alpha$ -hemolysin and MspA. 10% error in  $\text{SiN}_x$  nanopore diameters from TEM images is estimated due to measurement error. For nanopores that were not imaged to avoid damaging them, the error in nanopore diameter is estimated to be larger,  $\sim 0.5$  nm, due to the TEM users reading error. Error in nanopore diameter may also come from a cleaning step in piranha solution that may slightly change the nanopore size prior to ionic measurements. For the smallest  $\text{SiN}_x$  nanopores, the open pore ionic current is found to be the best measure of their effective size. Because of similar sizes but larger operating voltages in  $\text{SiN}_x$  nanopores, the signal amplitude is about ten times larger and the signal conductance is up to six times larger than in biological nanopores. All comparisons are made for 1M KCl.

model using an equivalent cylinder of reduced effective thickness ( $h_{eff}$ ) is sufficient to quantitatively explain the open and blocked current values measured during DNA translocations.<sup>66,142</sup> By fitting both the ionic open-pore and blocked-pore current data for many different diameter nanopores with the same membrane thickness,  $h_{eff}$  is estimated to be one third of the actual membrane thickness ( $h$ ).<sup>142</sup> This implies that TEM drilled nanopores in 5 nm thick  $\text{SiN}_x$  membranes have  $h_{eff} \sim 1.7\text{nm}$ . To make a  $\text{SiN}_x$  effective constriction as thin as the constriction in MspA, a nanopore would need to be drilled through a 1.5 nm thick  $\text{SiN}_x$  membrane , giving  $h_{eff} \sim 0.5\text{nm}$ , which roughly spans four DNA bases.<sup>87</sup>

### 3.1.3 Experimental Methods

Figure 3.1.3a shows the details of the solid-state nanopore design employed in these studies. Silicon nitride membranes locally thinned from an initial thickness of 85 nm were used in this study. Membrane thinning methods have been described elsewhere.<sup>142</sup> Briefly, small squares are patterned on suspended membranes using electron beam lithography, and the squares are thinned using SF<sub>6</sub> plasma. Silicon nitride membrane thickness and etch rate were determined using a three step process. First, membranes were patterned and etched for a range of times between 160 s and 500 s (see Appendix for detailed recipes). Second, the etch depth of each membrane was found from atomic force microscopy (AFM) scans of the surface profile. After approximately 280s, the etch rate was found to change as the SF<sub>6</sub> etched through the SiN<sub>x</sub> and began to etch the underlying SiO<sub>2</sub> (see Figure 3.1.2a). Third, for all the membranes with thinned regions intact (i.e., the etch time was less than 280s, so the thinned region was not etched through), a nanopore was drilled in the membranes, and the membranes were imaged in dark field STEM. Because the thinned and unthinned regions of the membrane have the same composition, the intensity of the dark field STEM image correlates to the thickness of the silicon nitride. The initial membrane thickness,  $l_{initial}$ , can be extracted by equating the fraction of the initial thickness remaining from AFM measurements and from dark field STEM measurements.

$$\frac{I_{thinned} - I_{background}}{I_{initial} - I_{background}} = \frac{l_{initial} - l_{AFM}}{l_{initial}} \quad (3.1)$$

Here *thinned* refers to the thinned area of the membrane,  $I$  refers to the dark field STEM intensity,  $l$  refers to membrane thickness, *background* refers to the background intensity seen through the nanopore, *initial* refers to the initial, unaltered membrane, and  $l_{AFM}$  refers to the step height measured in the AFM images. Figure 3.1.2b shows the percent of the unetched membrane intensity seen in the thinned region as a function of etch time. From these measurements, the plasma etch rate was found to be 0.3 nm/s, and  $l_{initial}$  was calculated to be  $\sim 85$  nm. Using this calibration, the thickness of the thinned area of each measured nanopore could be directly measured using dark field STEM. Figure 3.1.2c shows an example of a dark field STEM image calibrated to measure the nanopore thickness.

A mass contrast image of one thinned square is shown in Figure 3.1.3b; the average line intensity profile (in red) gives the mass-thickness contrast shown in Figure 3.1.3c. Nanopores are drilled inside thinned membrane region either in TEM mode or in scanning transmission electron microscopy (STEM) mode. Nanopores drilled in STEM mode were drilled in the thinnest area of the membrane, as determined by custom software. Thin membranes are drilled more easily than the standard 25 to 100 nm thick membranes, and controlling the nanopore size to sub-2 nm diameter is best achieved with the lowest current densities in the TEM. Figure 3.1.4 shows images of several nanopores fabricated in this manner. A 10% error is estimated in determining the nanopore diameter from these images; this error takes into account the fact that the shape of the nanopores is more precisely described as an ellipse, rather than a

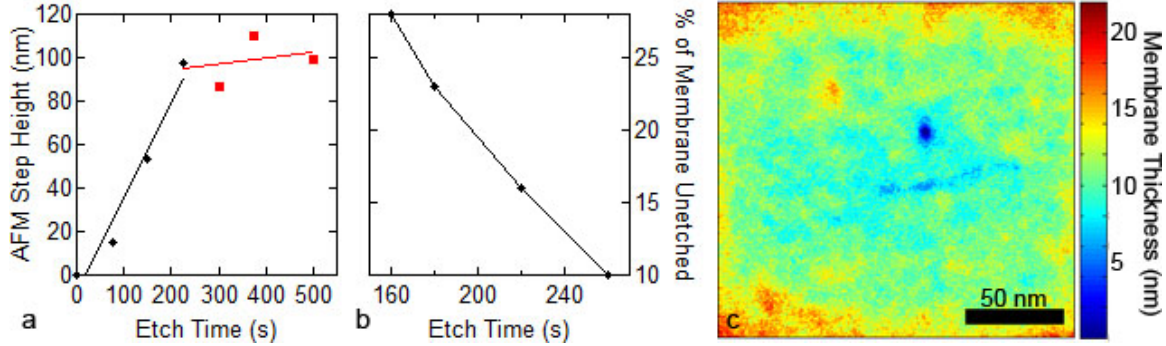


Figure 3.1.2: SiN<sub>x</sub> thinning calibration. (a) The AFM step height between the unetched and etched membrane regions as a function of etch time. The slope abruptly changes around 280s, at which point the silicon nitride is completely etched through, and the SF<sub>6</sub> begins to etch the SiO<sub>2</sub> at a slower rate. SiN<sub>x</sub> etching is plotted in black and SiO<sub>2</sub> etching is plotted in red. (b) The percent dark field STEM intensity of the etched membrane region compared to the unetched region as a function of etch time. Both intensity values have the background intensity (as measured through a nanopore) subtracted. (c) A calibrated dark field STEM image of a nanopore (blue spot) in a thinned region of a membrane. The rms surface roughness,  $h_{rms}$ , is found to be 2 nm. Nanopores drilled in STEM mode were drilled in the thinnest area of the membrane, as determined by custom software. The raw data from the mass contrast image is given in intensity. To translate to nm, the background intensity (found from the intensity through the nanopore) is subtracted from the intensities of the thinned and unthinned regions, and the intensity values outside the etched region are scaled to our original membrane thickness of 85 nm.

circle (the reported diameter is the average of the major and minor diameters). Most nanopores presented here are not imaged in order to avoid altering the nanopore size with further electron beam exposure.<sup>66</sup> Instead, the nanopore diameter is determined by relying on guides on the TEM phosphor screen and calculations from the open pore conductance.<sup>66</sup> The ionic conductance has the advantage of incorporating any size changes that may occur during cleaning procedures prior to measurement. The error in the calculated diameters for the nanopores that were not imaged is estimated to be  $\pm 0.5$  nm.

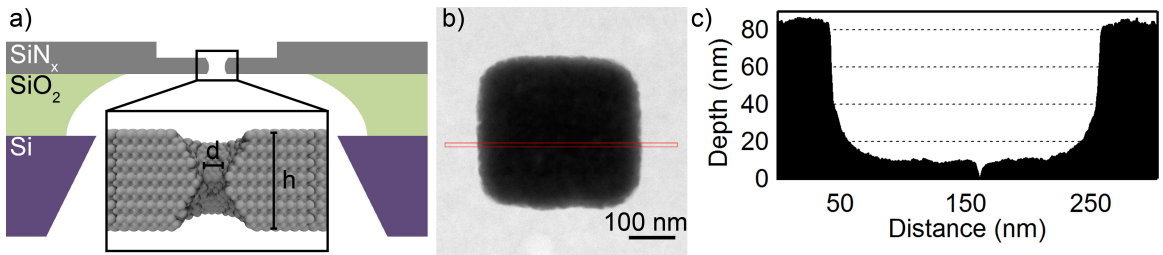


Figure 3.1.3: (a) Schematic of the stacked silicon chips used to fabricate nanopores. The window is locally thinned, and a nanopore is drilled in it. The nanopores height and diameter are defined as shown in the inset. (b) STEM mass contrast image of the thinned region of a membrane with a nanopore in it. The red line is integrated over to give a profile of the thinned region (c). The mass contrast data is scaled by the known thickness of the original membrane to give the thickness of the thinned region.

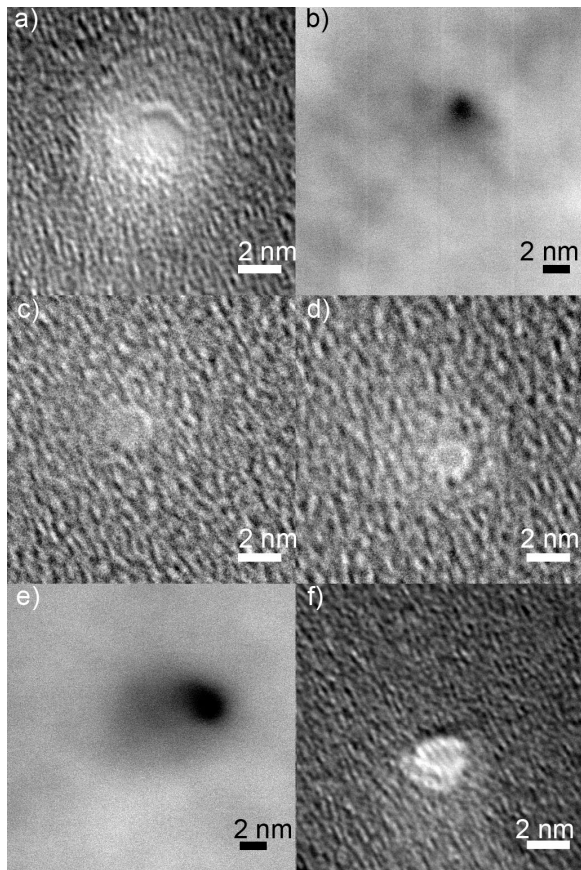


Figure 3.1.4: TEM images of sub-2 nm diameter pores in various thicknesses of  $\text{SiN}_x$ . Most pores fabricated were not imaged to avoid altering the pore size, and many may be smaller than those shown here, based on their appearance while drilling and conductance measurements. Pore diameters from these images are calculated from the average diameter of a fit to an ellipse. (a) 0.9 nm diameter pore in 30 nm thick  $\text{SiN}_x$  (b) STEM image of a 1.8 nm diameter pore in 5 nm thick  $\text{SiN}_x$  drilled in a thinner region of the thinned square (c) 1.6 nm diameter pore in 20 nm thick  $\text{SiN}_x$  (d) 1.3 nm diameter pore in 20 nm thick  $\text{SiN}_x$  (e) STEM image of a 1.3 nm diameter pore in 8 nm thick  $\text{SiN}_x$  drilled in a thinner region of the thinned square (f) TEM image of a 1.4 nm diameter pore in 5 nm thick  $\text{SiN}_x$  drilled in a thinner region of the thinned square.

The nanopore is assembled in the PTFE cell and the two chambers are filled with a salt solution composed of 1 M KCl + 1 mM ethylenediaminetetraacetic acid (EDTA) buffered to pH 8 using 10 mM tris(hydroxymethyl)aminomethane (Tris)-HCl. The PTFE cell features temperature regulation using a thermoelectric device connected to a copper block that houses the cell. Data are obtained with the copper block cooled to 2°C. Bias potentials between 600 mV and 1V are applied across the nanopore through Ag/AgCl electrodes, and ionic current is monitored as a function of time. These high voltage biases are used to increase the signal and the resulting signal-to-noise ratio.

Experiments were carried out using the VC100 high-bandwidth, low-noise voltage-clamp amplifier (Chimera Instruments, New York, NY) to apply a voltage bias and measure the current through the nanopore. This amplifier extends a traditional patch-clamp circuit topology<sup>117</sup> to support higher signal bandwidths. While its noise floor is not as low as a fully integrated design,<sup>114</sup> the new instrument is largely interchangeable with an Axopatch 200B (Molecular Devices), and it co-exists easily with the temperature controlled fluid cell. The amplifier includes a fourth order Bessel low-pass filter at 1 MHz, and signals are digitized at 4–6 MS/s. Acquired data are digitally low-pass filtered to the desired signal bandwidth before analysis in Matlab (MathWorks, Natick, MA). Not all of the datasets required the full amplifier bandwidth, but higher sample rates ensure many data points per translocation event and provide flexibility during data analysis. The limited bandwidth of popular patch-clamp amplifiers has previously been shown to lead to attenuation by as much as ∼

20% of solid-state nanopore blockades briefer than 16  $\mu$ s.<sup>142</sup>

### 3.1.4 Electronic Characterization

These experiments have translocated short ssDNA molecules from 30 to 180 bases long. Figures 3.1.5a-b show the resulting ionic currents through the nanopore for poly(dA)<sub>50</sub> molecules translocating through a 2 nm diameter nanopore in a 5 nm thick membrane at an applied bias of 1 V with data filtered to a 1 MHz bandwidth. Observed events can be coarsely classified into two groups. Shallow events were observed with blocked currents close to the open pore current, which were attributed to DNA deflection events. These events have been observed under similar measurement conditions.<sup>114</sup> The remaining deeper events correspond to DNA translocations (Figure 3.1.5b).<sup>114</sup> Only events that are unimodal are considered for analysis, i.e., events with no obvious intra-event structure,<sup>114</sup> and whose blockade currents have a standard deviation similar to that of the open pore current (300 pA<sub>rms</sub> at a 500 kHz bandwidth).

The open pore current in these measurements typically drifts by  $\sim 3\%$ , as seen in Figure 3.1.5a. Open pore ionic conductances (Figure 3.1.5c) range from 3 nS to 14 nS for nanopores with diameters between 0.8 and 2 nm and membrane thicknesses between 5 and 8 nm, matching theoretical predictions.<sup>66,67,142</sup>

To support a 1 MHz signal bandwidth, experiments are performed with a VC100 low-noise voltage-clamp amplifier (Chimera Instruments, New York, NY). Direct com-

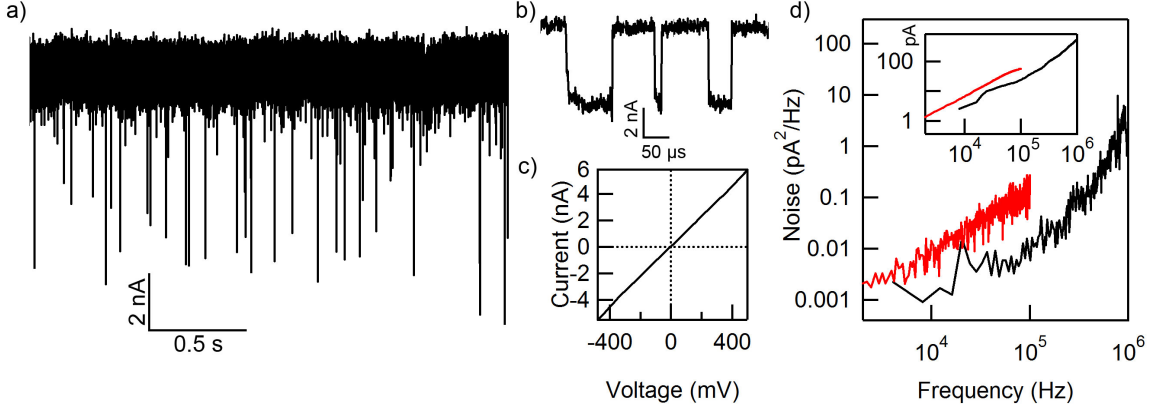


Figure 3.1.5: Characterization of noise in the  $\text{SiN}_x$  nanopores and the experimental setup using two amplifiers. (a) Raw current versus time trace for 50-mer ssDNA translocating through a 2 nm diameter nanopore in a 5 nm thick membrane with an applied bias of 1 V. The trace is digitally low-pass filtered to 1 MHz bandwidth. (b) Zoomed in events from the trace in (a). Events have minimal attenuation and high signal-to-noise ratios. (c) Current versus voltage (I-V) trace for a 2 nm diameter nanopore in an 8 nm thick membrane. The slope of this curve yields a conductance of 9.9 nS. (d) Input-referred noise power spectral density for a nanopore measured with an Axopatch 200B (red trace) and a nanopore measured with a Chimera VC100 (black trace). See Figure 3.1.6 for additional noise spectra. Inset: calculated root-mean-square current noise for both amplifiers, as a function of signal bandwidth.

parison of the noise power spectral densities of measurements with these electronics and the more conventional Axopatch 200B are possible below 100 kHz, as shown in Figure 3.1.5d, although there is variance between experiments (see Figure 3.1.6). These traces typically exhibit input-referred noise of 520 pA<sub>rms</sub> at the full bandwidth of 1 MHz, and accordingly less noise at lower bandwidths (see Figure 3.1.5d inset). When data are filtered to 100 kHz, a bandwidth closer to many published nanopore recordings,<sup>48,109,140</sup> the noise is 24 pA<sub>rms</sub>. The primary source of noise at these frequencies is the interaction between the voltage noise of the amplifier and the capacitance of the solid-state membrane chip, which is estimated to be 50 pF.

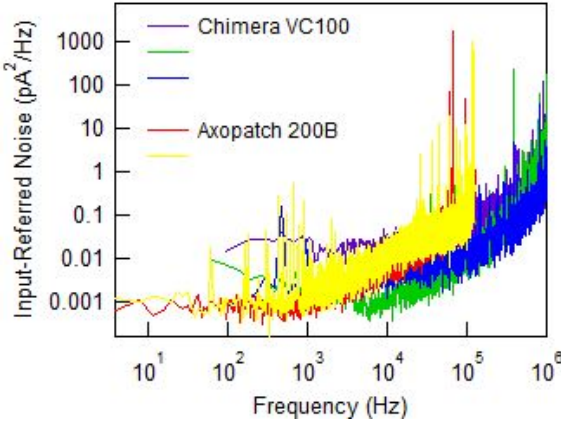


Figure 3.1.6: Input-referred noise power spectral density of various nanopores tested with either an Axopatch 200B or a Chimera VC100 amplifier. The observed noise was largely a function of electronic and ionic capacitances, and as a result it did not depend strongly on the dimensions of the nanopore. Parasitics varied slightly with each experiment, but data from the Chimera amplifier typically exhibited moderately lower noise density than the Axopatch.

For comparisons of ionic currents from different homopolymers, short, 30-base ss-DNA composed of homopolymers of either adenine ( $\text{poly(dA)}_{30}$ ), thymine ( $\text{poly(dT)}_{30}$ ), or cytosine ( $\text{poly(dC)}_{30}$ ) was used (Integrated DNA Technologies). Guanine is not included in these experiments due to G-tetrad formation in homopolymers longer than four bases. Longer ssDNA has previously been measured in solid-state nanopores, but observed differences in ionic currents have been attributed to secondary structure in the molecules (i.e., base stacking).<sup>63</sup> While ssDNA has a short persistence length ( $\sim 0.3 \text{ nm}$ )<sup>129</sup> and will coil at shorter lengths than dsDNA, the small diameters of the nanopores prevent the passage of folded ssDNA. In addition, the force on the DNA corresponding to the applied bias (1000 mV) is sufficient to overcome both the entropic and enthalpic barriers from any secondary structure in the homopolymers.<sup>93</sup> One  $\mu\text{L}$  of 100  $\mu\text{M}$  solution of one homopolymer is added to the chamber at the lower potential to yield a final concentration of 2  $\mu\text{M}$ . After adding the nucleotides, transient current reductions appear in the ionic-current trace. Between each homopolymer experiment, the nanopore is rinsed thoroughly with deionized water, and a baseline

current trace is recorded for five minutes to ensure that no blockades are seen before the next homopolymer is measured.

### 3.1.5 Analysis of Homopolymer Events

Figure 3.1.7a shows concatenated current blockades for each homopolymer, poly(dA)<sub>30</sub>, poly(dC)<sub>30</sub>, and poly(dT)<sub>30</sub>, from a 1.4 nm diameter nanopore in a 5 nm thick membrane taken at a 1 V applied bias at a signal bandwidth of 500 kHz (at which a signal-to-noise ratio of better than 10 is achieved). The events are identified using a threshold of 3 nA below the open pore current (green line in Figure 3.1.7), which excludes shallower collision events. Figure 3.1.7a shows many short, ssDNA translocation events densely packed in time, such that each event in this figure appears as a narrow spike (a magnified view of these events for each homopolymer is shown in Figures 3.1.7e-g). The current histograms determined from this data for each homopolymer are shown in Figures 3.1.7b-d. Using more than 700 events for each homopolymer, poly(dA)<sub>30</sub> gives a mean event depth of  $\langle \Delta I_A \rangle = 5.1 \pm 0.4$  nA, poly(dC)<sub>30</sub> gives a mean event depth of  $\langle \Delta I_C \rangle = 4.2 \pm 0.1$  nA, and poly(dT)<sub>30</sub> gives a mean event depth of  $\langle \Delta I_T \rangle = 4.8 \pm 0.2$  nA. The mean and error (standard deviation) values for event depth are calculated from Gaussian fits to the histograms. A Welch's t-test is performed for the difference between the mean depths for each pair of homopolymers, and the p-value is found to be less than 0.0001 in all three cases, indicating that while the distributions overlap, the difference between the means has

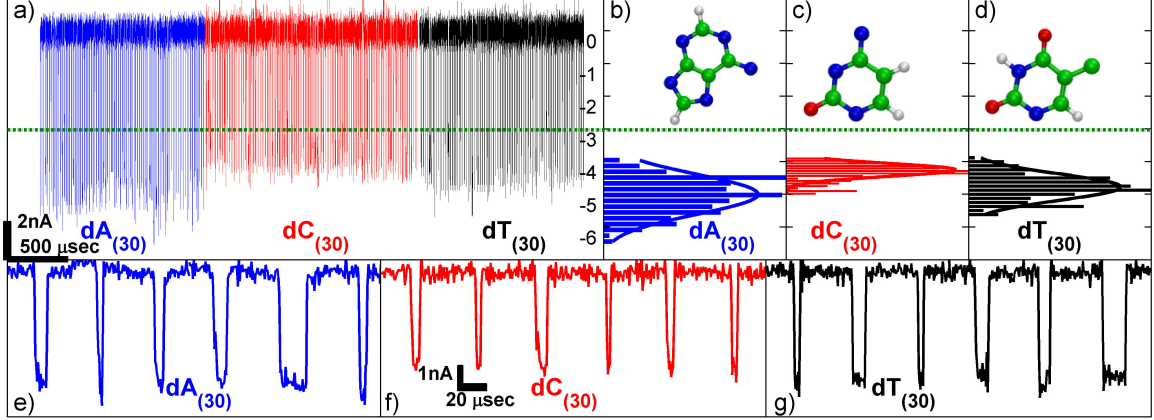


Figure 3.1.7: Results for poly(dA)<sub>30</sub>, poly(dC)<sub>30</sub>, and poly(dT)<sub>30</sub>. (a) Concatenated events from each homopolymer. The green line is the threshold for defining events. (b) Normalized histogram of event depths for poly(dA)<sub>30</sub>. The mean value is  $5.1 \pm 0.4$  nA. (c) Normalized histogram of event depths for poly(dC)<sub>30</sub>. The mean value is  $4.2 \pm 0.1$  nA. (d) Normalized histogram of event depths for poly(dT)<sub>30</sub>. The mean value is  $4.8 \pm 0.2$  nA. Mean values and errors are calculated from Gaussian fits to the histograms. Insets in (b)-(d) are diagrams of the base corresponding to the histogram. (e)-(g) Sample events from the data set shown in (a). The left trace (blue) shows events from poly(dA)<sub>30</sub>, the middle trace (red) shows events from poly(dC)<sub>30</sub>, and the right trace (black) shows events from poly(dT)<sub>30</sub>. This data is low-pass filtered to a bandwidth of 500 kHz.

strong statistical significance.

The ratios of mean event depths between homopolymers (e.g.,  $\langle \Delta I_A \rangle / \langle \Delta I_C \rangle$ ) was found to be constant across the range of nanopore dimensions considered. In particular, in three experiments on different nanopores with nanopore diameters between 1 and 2 nm and membrane thicknesses between 5 and 8 nm, the ratio of mean event depths of adenine to cytosine is  $\langle \Delta I_A \rangle / \langle \Delta I_C \rangle = 1.25 \pm 0.05$ , and the ratio of mean event depths of thymine to cytosine is  $\langle \Delta I_T \rangle / \langle \Delta I_C \rangle = 1.16 \pm 0.02$ . The current blocked by a homopolymer in the nanopore is given by  $\langle \Delta I \rangle \sim S/h$ , where  $S$  is the cross-sectional area of the homopolymer, and  $h$  is the thickness of

the nanopore. Therefore, the ratio of mean currents for two homopolymers, e.g., poly(dA)<sub>30</sub> and poly(dC)<sub>30</sub>, is then equal to the ratio of homopolymer cross-sectional areas,  $S_A$  and  $S_C$ , and independent of nanopore thickness,  $\langle \Delta I_A \rangle / \langle \Delta I_C \rangle = S_A / S_C$ . In contrast, other measurements, such as the mean current difference (e.g.,  $\langle \Delta I_A \rangle - \langle \Delta I_C \rangle \sim (S_A - S_C)/h$ ), vary for different nanopores. It is promising that homopolymer differentiation was achieved using a range of nanopore diameters and membrane thicknesses, as this suggests that some geometric variability in solid-state nanopores may be tolerable in future nanopore DNA sequencing systems.

Since all three homopolymers have the same length ( $\sim 10$  nm), they are expected to produce similar blockade durations unless they have different interactions with the nanopore surfaces. Event durations for data in Figure 3.1.7 range from 4  $\mu$ s to 200  $\mu$ s, with characteristic durations of 18  $\mu$ s for poly(dA)<sub>30</sub>, 33  $\mu$ s for poly(dC)<sub>30</sub>, and 22  $\mu$ s for poly(dT)<sub>30</sub>. Histograms of event durations for these homopolymers exhibit an exponential form,  $e^{-t/\tau}$  seen in Figure 3.1.8,<sup>91,144</sup> which has also been reported for thin SiN<sub>x</sub> nanopores<sup>114,142</sup> and graphene nanopores.<sup>94</sup> These timescales correspond to a typical DNA velocity between 0.3–0.6  $\mu$ s per base. The event durations measured are also of the same order of magnitude as previous experimental results of 20  $\mu$ s for dsDNA of similar length (25 base pairs).<sup>142</sup> Event duration was not used as a basis for homopolymer differentiation.

These results qualitatively agree with a model of blockade levels that depends predominantly on the physical size of each base. Adenine, the largest base, blocks

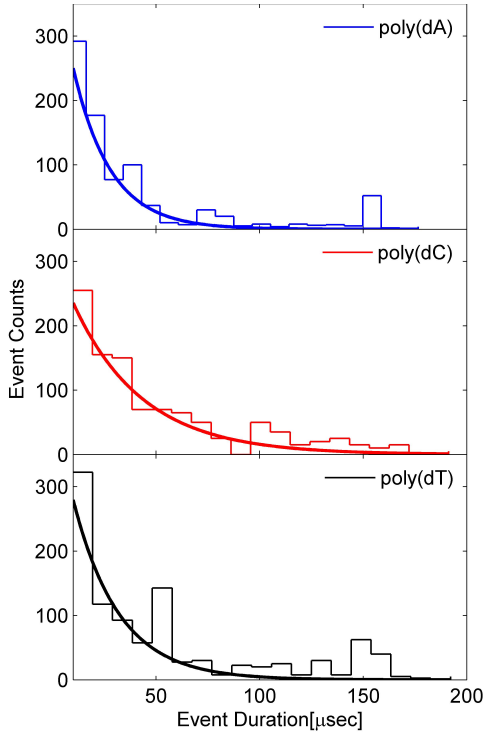


Figure 3.1.8: Histogram of event duration for each of the homopolymers. The histograms were fitted using a single exponential decay function ( $e^{-t/\tau}$ ). The time scales for the different homopolymers were 18  $\mu\text{s}$  ( $\text{poly}(\text{dA})_{30}$ ), 33  $\mu\text{s}$  ( $\text{poly}(\text{dT})_{30}$ ), and 22  $\mu\text{s}$  ( $\text{poly}(\text{dC})_{30}$ ), close to values previously obtained for similar conditions.

the most ionic current, while the two smaller bases (cytosine and thymine) block the least ionic current. The inset of Figures 3.1.7b-d shows the atomic structure of adenine, cytosine, and thymine. Additionally, as observed in Figures 3.1.7b-d, the width of the current distribution for  $\text{poly}(\text{dA})_{30}$  is larger than the width of the current distributions for  $\text{poly}(\text{dC})_{30}$  and  $\text{poly}(\text{dT})_{30}$ . This may be due to the effects of base orientation; the larger adenine base can have more conformations, possibly leading to a wider spread of current blockades compared to cytosine and thymine. For a range of thin nanopores with 0.9 to 2 nm diameters, similar blocked currents, 30 - 80% of the open pore current, are observed for various homopolymers (see Figure 3.1.9), and current differences between pairs of homopolymers are similar to those shown in Figures 3.1.7b-d. Further studies should attempt to quantitatively explain the

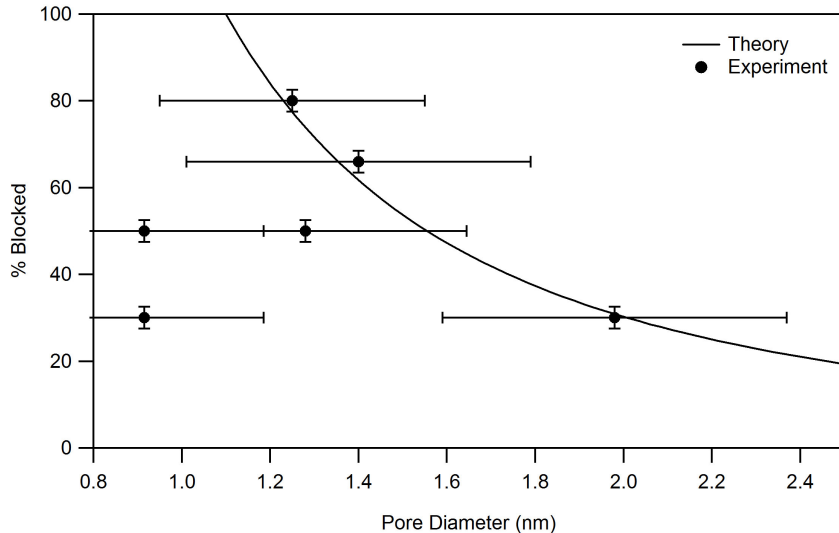


Figure 3.1.9: Percent of the open pore current blocked by homopolymers in six experiments. All nanopores are between 5 and 10 nm thick, and the nanopore diameter is determined from ionic conductance measurements. The homopolymers used vary by experiment. The theory line,  $(1.1)^2/d^2 \times 100\%$ , where  $d$  is the pore diameter, is a calculation of the percent blocked as determined from the ratio of cross-sectional areas of the ssDNA and the nanopore.

observed differences in the magnitudes of blocked currents and optimize parameters to narrow these distributions. This could be achieved by lowering the system noise and performing systematic studies of the effects of DNA length, nanopore dimensions, applied voltage, and salt concentration. Note that standard deviations in the blockade histograms (Figures 3.1.7b-d) are comparable to the baseline current noise amplitudes, which suggests that further reduction of measurement noise may reduce the overlap of current distributions between homopolymers.

### **3.1.6 Pores Too Small for ssDNA**

A study of the translocation dynamics of ssDNA in a nanopore with a calculated diameter of 0.8 nm was attempted, but no translocations were observed (see Figure 3.1.10). The nanopore has 600 mV applied voltage across it, and approximately 2  $\mu$ M of an 180-mer ssDNA composed of 75 thymine nucleotides on either side of a 30 cytosine nucleotide block in the correct chamber to drive translocations. For over 18 minutes, although the current gradually varied by about 10% (as seen in the trace), no translocations were observed, whereas the larger nanopores readily allowed DNA translocations. The smallest nanopore in which we observed translocations had a calculated diameter of 0.9 nm. Nevertheless, for the smallest pores we made, we did not observe translocations, while the larger pores readily allowed translocations of short ssDNA. This suggests that we have entered a range of diameters smaller than the cross-sectional size of ssDNA. In order to precisely determine the minimum pore diameter that allows ssDNA to pass through, we would need to develop a more precise calibration of the nanopore diameter in this size range and establish a minimum diameter that can be statistically validated from measurements on a large number of nanopores. In addition, the limits of nanopore thinning have not been fully explored.

### **3.1.7 Summary**

In this work, solid-state nanopores having diameters of 1 to 2 nm were fabricated in membranes as thin as approximately 5 nm, comparable to the dimensions of com-

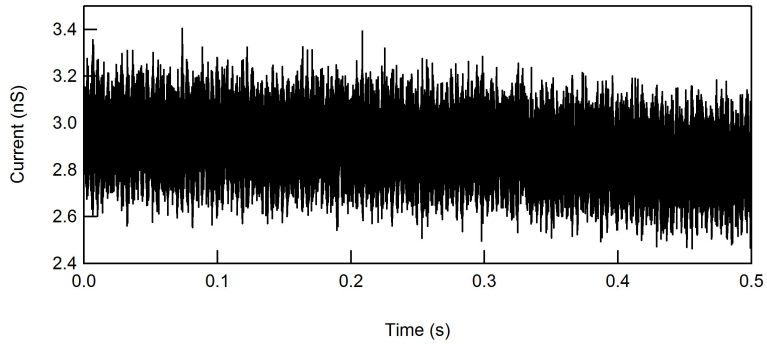


Figure 3.1.10: Ionic current vs time trace for a nanopore apparently too small to allow translocations. From conductance calculations, the estimated nanopore diameter is 0.8 nm. This nanopore was not imaged by TEM to avoid altering its size. Note that the conductance of such small diameter nanopores in thin membranes is rather high compared to the typical  $\text{SiN}_x$  nanopores of the same diameter in much thicker membranes used in most literature.

monly used biological nanopores. The ionic current was measured with reduced electronic noise and improved temporal resolution, which allowed demonstration of proof-of-principle differentiation of ssDNA homopolymers. The mean homopolymer current signals differed by 200 - 900 pA in 1 M KCl solution at applied voltages between 600 mV and 1 V. Future studies may further address the relationship between individual nucleotides properties and observed solid-state nanopore current signals, as well as improve experimental parameters to achieve differentiation of individual bases within a single DNA molecule.

## 3.2 Graphene as a Membrane Material

### 3.2.1 Introduction

Recently, the four DNA bases were shown to impede the ion current differently in nanopores,<sup>4,19,135</sup> and other theoretical and experimental works suggest that the four bases can be discriminated by measuring their transverse conductance.<sup>14,106,154</sup> In light of these works, synthetic nanopore materials with atomic thickness and electrical addressability may serve as a step toward nanopore-based DNA sequencing. Common membrane materials currently used for nanopore device fabrication are insulators such as silicon nitride<sup>76</sup> ( $\text{SiN}_x$ ), aluminum oxide,<sup>134</sup> and silicon oxide<sup>125</sup> ( $\text{SiO}_2$ ). Graphene is a thin, flexible material with good electronic conductivity and robust mechanical properties.<sup>18,45,95,100</sup> Fischbein et al.<sup>34</sup> have shown that nanopores, nanopore arrays, and other structures, can be fabricated in suspended graphene sheets by controlled electron beam exposure in a transmission electron microscope (TEM). Despite the extreme thinness of the suspended graphene sheets, nanopores were structurally robust and their shape was stable over time. Use of graphene as a nanopore membrane material could permit sensing and control of the electric potential directly at the nanopore. Additionally, atomically thin graphene nanoelectrodes have been considered for DNA sequencing based on the transverse conductance of DNA<sup>106</sup> and multilayer graphene-insulator devices could control the molecules motion sufficiently to reliably measure the conductance of each consecutive nucleotide.<sup>39,40</sup>

In this section, the first experimental realization of DNA translocation through graphene nanopores is discussed, which is the first step toward exploring the potential applications of this new membrane material. The ionic blocked current signatures from DNA translocations through sub-10 nm diameter graphene nanopores compare favorably with similar diameter SiN<sub>x</sub> nanopores. However, the current signal from bare graphene nanopores is consistently noisier than that for SiN<sub>x</sub> nanopores, and the DNA translocation signals reveal nonuniform current amplitudes. The large noise is attributed to the presence of pinholes in the graphene membranes as well as incomplete wetting. Atomic layer deposition (ALD) of several nanometers of titanium dioxide over the devices consistently reduces the nanopore noise level and improves the mechanical robustness of the device. This process preserves electrical addressability of the nanopore, which may be useful for realizing both multilayer grapheneinsulator nanopores<sup>39,40</sup> and graphene nanogap devices.<sup>106</sup>

### 3.2.2 Experimental Methods

A schematic of a typical graphene nanopore device is given in Figure 3.2.1. Forty nm thick silicon nitride membranes approximately 50 × 50 μm square were used for this experiment. Electron beam lithography (EBL) followed by an SF6 plasma etch is used to pattern a 1.5 μm diameter hole through the nitride membrane. Multilayer graphene is grown by the chemical vapor deposition (CVD) of methane over polished copper foils,<sup>79</sup> as detailed in Figure 3.2.2 and Section 5. The copper foils are etched in

solution so that bare graphene sheets, approximately 1-5 nm thick (3-15 monolayers), shown in Figure 3.2.2d, float on the surface of the liquid. Suitably sized graphene sheets, larger than 2 mm × 2 mm, are then scooped onto the prepatterned silicon nitride membranes, as shown in Figure 3.2.3. In this way the graphene is structurally supported by the nitride membrane, with only a limited area freely suspended over the 1.5  $\mu$ m hole. Nanopores are then drilled through the suspended graphene membranes by transmission electron beam ablation lithography<sup>33,34</sup> (TEBAL). CVD graphene was used, rather than exfoliated, because the centimeter-scale sheets are easy to manipulate and the process is scalable for future applications. It has been observed that CVD graphene is very hydrophobic,<sup>139</sup> and a rapid UV/ozone treatment was found to facilitate complete wetting of the graphene nanopores. Because piranha solution attacks organic materials including graphene, the graphene devices were not piranha treated. Instead, all devices underwent at least 5 min of UV/ozone treatment immediately prior to assembly in a PDMS measurement cell and exposure to electrolyte. With a pair of Ag/AgCl electrodes, a bias voltage,  $V_B$ , is applied between the two reservoirs to drive ionic current through the nanopore.

A TEM image of a representative nanopore drilled into a suspended graphene membrane is given in Figure 3.2.1b. The visible rings around the pore are from graphene layers, and their number provides an estimate of the graphene membrane thickness.<sup>34,82,95</sup> Figure 3.2.1c shows a typical measurement of the ionic current through a graphene nanopore as a function of the applied voltage,  $V_B$ . Graphene nanopores

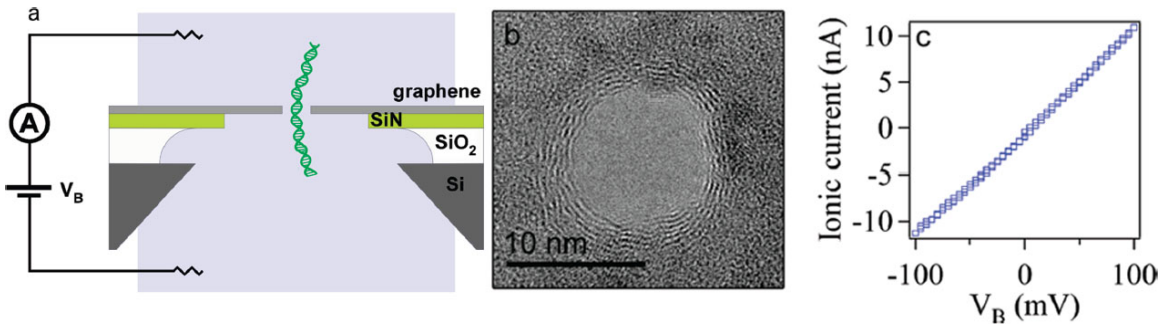


Figure 3.2.1: Graphene nanopore devices. (a) Device schematic. Few-layer graphene (1–5 nm thick) is suspended over a 1  $\mu\text{m}$  diameter hole in a 40 nm thick silicon nitride ( $\text{SiN}_x$ ) membrane. The  $\text{SiN}_x$  membrane is suspended over an approximately  $50 \times 50 \mu\text{m}^2$  aperture in a silicon chip coated with a 5  $\mu\text{m}$   $\text{SiO}_2$  layer. The device is inserted into a PDMS measurement cell with microfluidic channels that form reservoirs in contact with either side of the chip. A bias voltage,  $V_B$ , is applied between the reservoirs to drive DNA through the nanopore. (b) TEM image of a nanopore in a graphene membrane. Scale bar is 10 nm. (c) Ionic I-V measurement for this 10 nm graphene nanopore device in 1 M KCl, pH 9.

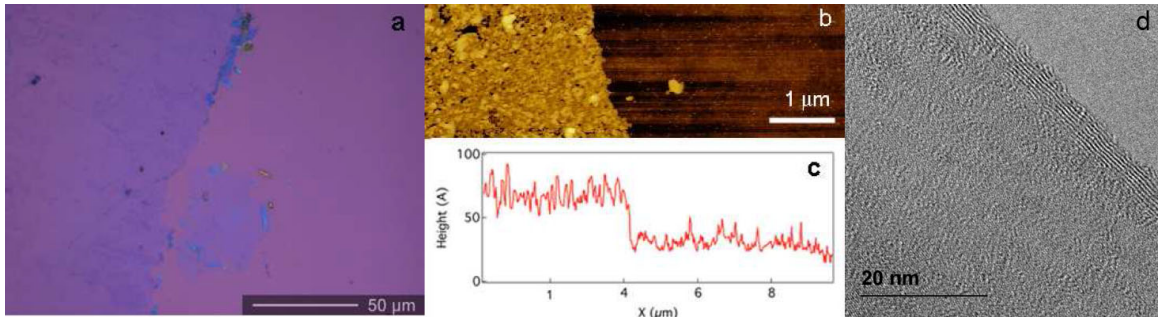


Figure 3.2.2: (a) Optical image of a large CVD graphene sheet deposited on 90 nm thick  $\text{SiO}_2$  on top of Si. Growth occurs under 10 minutes of  $\text{H}_2$  and  $\text{CH}_4$  at 1000 °C followed by rapid cooling. Substrates for graphene growth are 1 x 2 Cu foils. Foil is dissolved in 1M  $\text{FeCl}_3$  solution followed by 4M HCl treatment. (b) AFM image of edge of graphene sheet. (c) Linescan through AFM image in (b). Sheet is approximately 5 nm thick (~ 15 layers). (d) TEM image of suspended CVD graphene sheet. Lines at edge indicate sheet is ~ 8 layers thick.

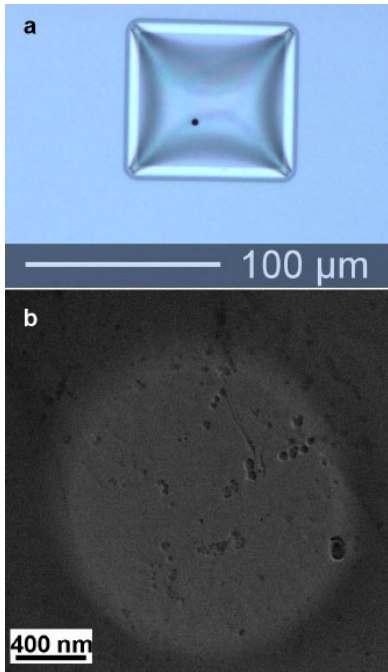


Figure 3.2.3: (a) Optical image of silicon nitride ( $\text{SiN}_x$ ) membrane with  $\sim 1.5 \mu\text{m}$  hole etched by electron beam lithography and  $\text{SF}_6$  plasma. (b) TEM image of graphene suspended over such a hole in  $\text{SiN}_x$ . Dark spots are impurities on the graphene surface.

with diameters ranging from 5 to 10 nm were found to exhibit a wide range of conductance values between  $\sim 20$  and 1000 nS (see Figure 3.2.4a). This wide conductance range does not correlate with nanopore size and cannot be explained by membrane thickness variations, which suggests that ions are able to flow through pinholes in the graphene membranes. UV/ozone treatment of graphitic material, such as carbon nanotubes (CNTs), has been shown to induce defects by an oxidative reaction.<sup>118</sup> Electron beam irradiation has also been shown to affect the properties of carbon-based materials and induce defects.<sup>46</sup> It is reasonable, therefore, that UV/ozone treatment and/or electron beam irradiation forms occasional pinholes in some of these ultrathin membranes,<sup>65</sup> though they are not readily visible under TEM observation. Measurements performed for this work, highlighted in Figures 3.2.4b and c, indicate that UV/ozone treatments create defects in graphene, which increase the electrical resistance of these

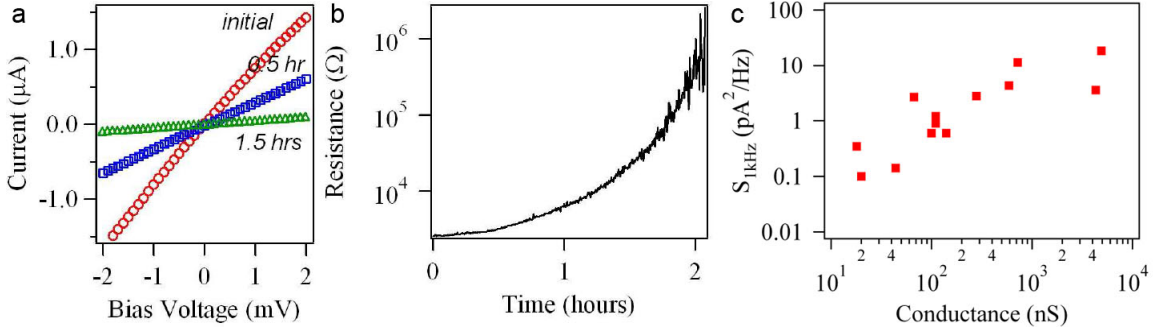


Figure 3.2.4: (a) Nanopore current noise as a function of open pore conductance. Each point is the median power spectral density over the range 1 to 2 kHz. Open pore conductance is computed using  $V_B$  and the measured open pore current for each device. (b) I-V measurement of a graphene sheet contacted by  $\sim 1$  mm long Ti/Au electrodes that are separated by approximately  $100 \mu\text{m}$ . I-V traces are taken before any UV/ozone treatment (red circle), after 0.5 hours of treatment (blue squares) and after 1.5 hours of treatment (green triangles). (c) Resistance of the sheet as a function of time during UV/ozone treatment.

sheets over time. While these pinholes increase the baseline ion current signal and associated noise, they do not otherwise hinder the ability of these devices to measure DNA translocation through the fabricated nanopores. The pinholes are too small for the DNA to pass through, so that the ion current through the pinholes simply adds in parallel with the primary nanopore current, as illustrated in Figure 3.2.5.

### 3.2.3 Measurements of Suspended Graphene Nanopores

A TEM image of an 8 nm graphene nanopore, along with a current trace showing DNA translocation through the nanopore device, is given in parts a and b of Figure 3.2.6. The electrolyte solution used for these measurements was 1 M KCl, 10 mM Tris, and 1 mM EDTA, pH 9. Fifteen kbp dsDNA (Fermentas NoLimits, Glen Burnie, MD) was added at a concentration of 1 nM to the analyte reservoir and ap-

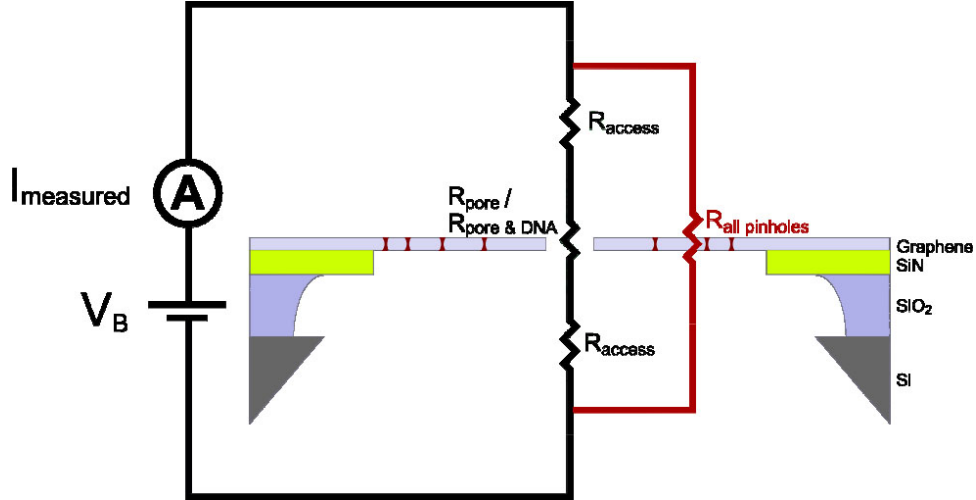


Figure 3.2.5: Equivalent circuit for graphene nanopore devices with pinholes in the graphene sheet, illustrating how they contribute to the measured current. Pinholes are represented as red holes through the graphene layer and modeled as resistances in parallel with that of the nanopore.  $R_{access}$ ,  $R_{pore}$ ,  $R_{pore\&DNA}$ ,  $R_{all\text{pinholes}}$  are the access resistance, the nanopore resistance, the nanopore resistance when DNA is in the pore and the equivalent resistance of all the pinholes in graphene, respectively.

plied a bias voltage of  $V_B = +100$  mV to the other reservoir in order to drive DNA through the pore. The ionic current signal was filtered with a 10 kHz three-pole Bessel filter and then sampled at 50 kHz. The 28 nA open pore current was seen to sharply decrease by between  $\sim 500$  pA and 1 nA as DNA molecules pass through the graphene nanopore. Translocation events are not observed before the addition of DNA molecules, as demonstrated in Figure 3.2.7. The overall noise level is much higher for this device than for silicon nitride nanopore devices previously measured (for example, see Figure 3.2.8), but the DNA capture rate is comparable for both nanopores ( $\sim 1$  event/s for 1nM and  $V_B = 100$  mV). The graphene nanopore noise is dominated by a  $1/f$  noise component, which will be discussed later.

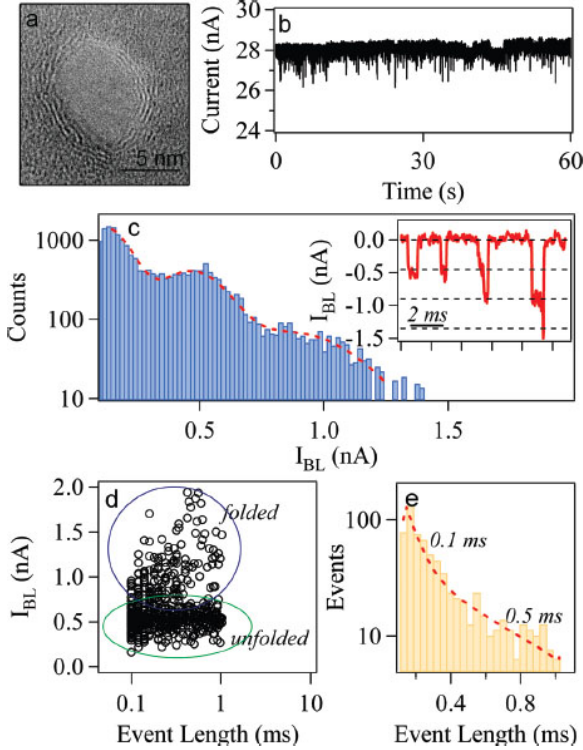


Figure 3.2.6: DNA translocation through graphene nanopores. (a) TEM image of an  $\sim 8$  nm graphene nanopore. (b) Time trace of events for nanopore device shown in (a). (c) Histogram of blocked currents for measured translocation events for the same device at  $V_B = 100$  mV in 1 M KCl solution. Data are fit using two Gaussian functions with mean values at 0.45 and 0.90 nA. Inset displays concatenated events including some unfolded and folded events which have been observed.  $I_{BL}$  values of 0.45, 0.9, and 1.35 nA are indicated with dashed black lines, indicating unfolded, singly folded, and doubly folded entries, respectively. (d) Scatter plot of event length vs event depth for the same device at  $V_B = 100$  mV. Regions of unfolded and folded events are highlighted inside the circled areas. (d) Histogram of event lengths for the same device. Data are fit (dashed red line) by a double exponential of the form  $a_1 e^{(-t/\tau_1)} + a_2 e^{(-t/\tau_2)}$  with time constants  $\tau_1 = 0.1$  and  $\tau_2 = 0.5$  ms.  $t$  is the time, and  $a_1$  and  $a_2$  are constants.

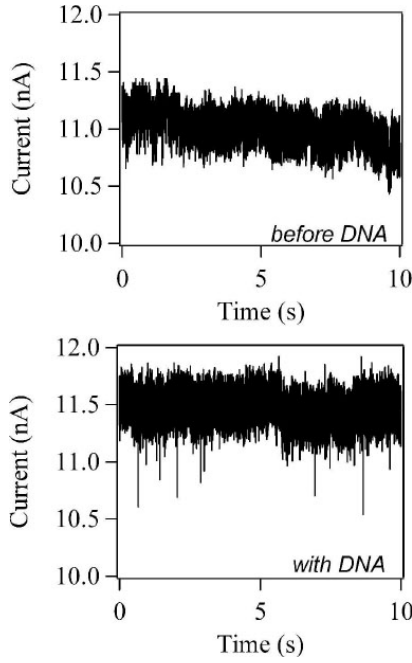


Figure 3.2.7: Time trace of ionic current for an 8 nm graphene nanopore at  $V_B = 200$  mV before and after the addition of DNA. Translocation events are only observed in the latter case. There is a slight change in the open pore current after the addition of DNA which is not significant and likely due to slight concentration differences between the solutions with and without DNA. DNA translocation is observed using 1 nM 15 kbp dsDNA in 1M KCl, 10mM Tris, pH 8.5 electrolyte solution. Current was recorded for  $V_B = 100$  mV, filtered at 30 kHz and sampled at 200 kHz.

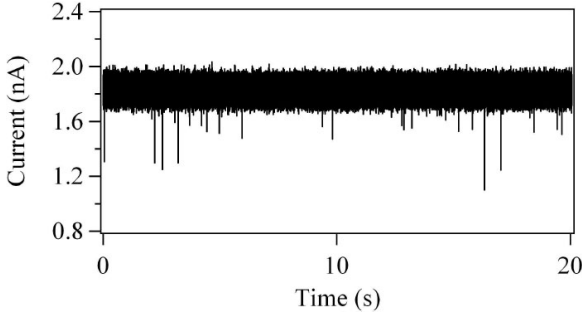


Figure 3.2.8: Time trace of DNA translocation through a 6 nm diameter, 40 nm thick  $\text{SiN}_x$  nanopore for 1 nM 15 kbp dsDNA in 1M KCl, 10mM Tris, pH = 8.5 electrolyte solution. Current was recorded for  $V_B = 100$  mV, filtered at 30 kHz and sampled at 200 kHz.

A histogram of the measured blocked current signal,  $I_{BL}$ , is shown in Figure 3.2.6c for the device shown in Figure 3.2.6a. Here,  $I_{BL}$  is defined as  $I_{BL} = \langle I \rangle - \langle I_{open} \rangle$ , where  $\langle I \rangle$  refers to the mean pore current during DNA translocation and  $\langle I_{open} \rangle$  refers to the mean pore current 0.1 ms before DNA entry. The data in Figure 3.2.6c have been fit with a double Gaussian with mean  $I_{BL}$  values of 0.45 and 0.9 nA. These mean values correspond to peaks in the histogram of the current data and indicate two event populations. Examples of both populations are represented in the inset by several representative events. These events clarify that both folded and unfolded events comprise the two populations. The blocked current fraction (i.e.,  $\langle I_{BL} \rangle / \langle I_{open} \rangle$ ) is  $\sim 5$  times smaller than expected based on the relative areas of the DNA molecule ( $A_{DNA}$ ) and the nanopore<sup>144</sup> ( $A_p$ ). An expected value of  $A_{DNA}/A_p \sim (2.2\text{nm})^2/(8\text{nm})^2 = 7.6\%$  was calculated, compared with a measured blocked current fraction of 1.6%.

Increased baseline open pore current due to pinholes is ultimately responsible for the decreased blocked current fraction. However, the magnitude of the  $I_{BL}$  values is 3 times larger than that obtained with similarly sized pores in 40 nm thick  $\text{SiN}_x$  membranes at these voltage levels.<sup>78</sup> This increase in  $I_{BL}$  is attributed to the thinner

graphene membrane, which is  $\sim$ 2 nm thick in Figure 3.2.2a. The thinner membrane decreases the overall pore resistance, therefore increasing the magnitude of the current blocked by the translocating DNA molecule. Blocked current values would be even larger for these thin membranes except that the access resistance, the resistance through the electrolyte from the nanopore to the bulk solution, is a significant part of the total resistance of the system (see Figure 3.2.5). Because of the access resistance, measured  $I_{BL}$  values are smaller than expected from the simple approximation that  $I_{BL}$  is inversely proportional to membrane thickness.

A scatter plot of event depth as a function of event length for  $\sim$  600 events measured with the same device is given in Figure 3.2.6d. Two clear groupings of events are visible, one centered on  $I_{BL} \sim 0.5$  nA (unfolded) and a second centered on  $\sim$ 1 nA (folded). A histogram of the measured event lengths for these events is given in Figure 3.2.6e. There is a large variation in the measured event lengths with no clear average value, indicating that the peak value is likely just below the measurement threshold. Two clear populations of events are observed and have been fit with exponential functions<sup>91,144</sup> using time constants of  $\tau_1 = 0.1$  ms and  $\tau_2 = 0.5$  ms. These time scales correspond to an average DNA velocity of between  $\sim$  5 and 30 ns/bp, comparable to DNA velocities through other nanopore materials.<sup>48</sup>

### 3.2.4 Addition of TiO<sub>2</sub> to Stabilize Membranes

While the results in Figure 3.2.6 are representative of these measurements of DNA translocation through suspended graphene membranes, the fraction of functional bare graphene nanopores that exhibit detectable DNA translocation is small. Of the 50 bare graphene nanopore devices that were tested, only  $\sim 10\%$  showed DNA translocation. From the remaining pores, 30% had hole defects visible under low-magnification TEM observation, 30% developed tears during the measurement, and 30% did not wet properly, indicated either by a conductance below  $\sim 1$  nS and/or a highly non-linear and hysteretic open pore current versus voltage (I-V) measurement. Therefore, despite a large interest in graphene nanopores as electrically addressable ultrathin membrane materials, the low functional yield of pores limits the usability of bare graphene nanopore devices, unless methods of improving membrane stability and wettability are realized.

To address the relatively low yield, a few nanometer thick TiO<sub>2</sub> layer was deposited on both sides of the graphene membrane using atomic layer deposition.<sup>1</sup> ALD has been used a number of times in the context of solid-state nanopores.<sup>16,76,98,130,133,134</sup> TiO<sub>2</sub> was chosen because of its excellent wettability with aqueous solutions<sup>138</sup> and superior bonding to graphitic material.<sup>152</sup> ALD has been previously shown to reduce the overall nanopore noise level<sup>15</sup> (particularly the low-frequency, 1/f component), presumably by generating a cleaner, more easily wettable surface.<sup>76</sup> An ionic I-V measurement of a 10 nm diameter nanopore in graphene coated with 5 nm TiO<sub>2</sub> is

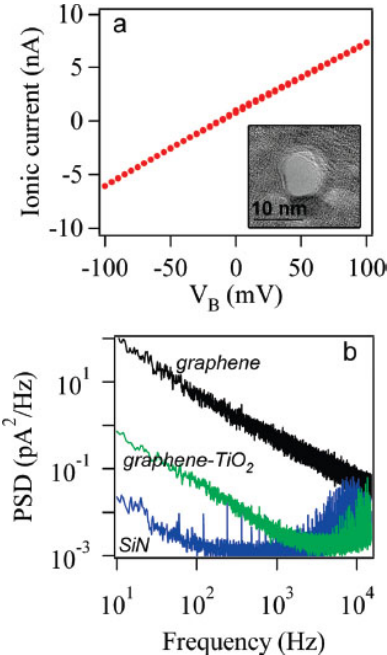


Figure 3.2.9: Characterization of  $\text{TiO}_2$ -covered graphene nanopore devices. (a) I-V measurement for a  $\text{TiO}_2$ -covered graphene nanopore. Inset is a TEM image of this 7.5 nm diameter nanopore. Scale bar is 10 nm. (b) Power spectral density of the pore current for an 8 nm diameter nanopore in a bare graphene device (black) at  $V_B = 100$  mV, a 7.5 nm diameter nanopore in a  $\text{TiO}_2$ -covered graphene device (green) at  $V_B = 100$  mV, and a 6 nm diameter nanopore in a silicon nitride device (blue) at  $V_B = 120$  mV.

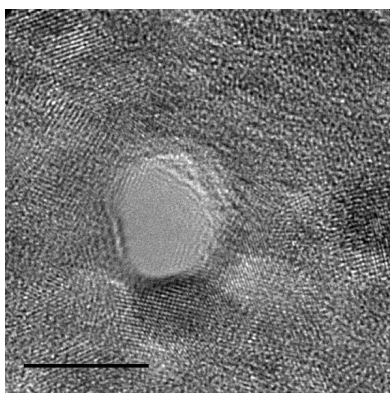


Figure 3.2.10: TEM image of crystallized  $\text{TiO}_2$  around a newly drilled nanopore  $\sim 8$  nm in diameter.  $\text{TiO}_2$  is deposited at 200°C from Ti (IV) Isopropoxide and  $\text{H}_2\text{O}$  in a Savannah 200 atomic layer deposition system (Cambridge Nanotech, Cambridge, MA). Growth rate is approximately 0.35 Å per deposition cycle. Scale bar is 10 nm.

shown in Figure 3.2.9a, along with a TEM image of the nanopore inset. Following the formation of nanopores, crystallization of the  $\text{TiO}_2$  was observed proximal to the nanopore, as previously observed with nanopores in ALD alumina membranes.<sup>133</sup> The coverage of the graphene membranes with  $\text{TiO}_2$  appears conformal based on TEM observation, as shown in Figure 3.2.10.

Representative power spectral densities (PSD) of open pore current traces are shown in Figure 3.2.9b for several devices: a 7.5 nm diameter graphene pore, an 8

nm diameter graphene-TiO<sub>2</sub> pore, and a 6 nm diameter SiN<sub>x</sub> pore. The overall noise level is typically higher for graphene devices than for SiN<sub>x</sub> nanopores tested in the same measurement cell. Particularly, the  $1/f$  noise component is especially large for bare graphene devices, extending to the  $\sim$ 10 kHz frequency range with an exponent of  $\sim 1$ , as compared with 10-100 Hz for silicon nitride pores. The low-frequency noise power,  $A$ , has been calculated for these traces using  $S_I/\langle I \rangle^2 = A/f$ , where  $S_I$  is the current noise up to  $\sim$ 5 kHz,  $\langle I \rangle$  is the mean open pore current, and  $f$  is the frequency.  $A$  was found to be  $7 \times 10^{-6}$  for bare graphene and  $2.5 \times 10^{-7}$  for TiO<sub>2</sub>-covered graphene, indicating that the covered device has an order of magnitude lower noise power than the bare graphene device. The lower noise power is attributed to the improved hydrophilicity of the TiO<sub>2</sub> surface.<sup>122</sup> Noise power values for the TiO<sub>2</sub>-covered device are larger than measured values for SiN<sub>x</sub> nanopores at a similar salt concentration.<sup>120</sup>

Noise due to device capacitance converts the voltage noise of the measurement amplifier into current noise, which typically dominates at the higher frequencies. Of all the devices measured, the graphene-based devices had a higher capacitance than the SiN<sub>x</sub> devices. The capacitance is higher for graphene because the conductive graphene sheet is capacitively coupled to the electrolyte solution. As a result, the entire 5-10 mm<sup>2</sup> graphene area, not just the 0.7 mm<sup>2</sup> area exposed to electrolyte by the measurement cell, forms a capacitor across the SiN<sub>x</sub> and SiO<sub>2</sub> layers to the underlying silicon and electrolyte. Although the  $50 \times 50$  microm<sup>2</sup> SiN<sub>x</sub> membrane is

$\sim$  100 times thinner than the rest of the chip, it does not dominate the capacitance because its area is  $\sim$  1000 times smaller than a typical graphene sheet.

Example time traces for DNA translocation through three TiO<sub>2</sub>-coated graphene nanopore devices are given in Figure 3.2.11. TEM images of the nanopores that range in diameter from 5.5 to 8 nm, and concatenated sets of translocation events for each nanopore, are inset. The open pore currents for the devices in Figure 3.2.11 do not scale with nanopore diameter, ranging from  $\sim$  2.8 nA at 100 mV (Figure 3.2.11a) to  $\sim$  96 nA at 150 mV (Figure 3.2.11c). This is a  $\sim$  20-fold difference in conductivity. The variation in open pore currents is likely a consequence of the quality difference between graphene membrane starting materials because all other fabrication and preparation steps were consistent. Nanoscale differences in graphene grain structure and thickness variation were observed across the relatively large ( $\sim$  3  $\mu\text{m}^2$  area, see Figure 3.2.3) suspended membrane from device to device arising from the nanoscale roughness of the mechanically polished copper foils as evidenced by AFM imaging. This roughness influences the density and rate of formation of pinholes during the TEBAL<sup>33</sup> and/or UV/ozone steps of the device fabrication process.

While some devices without pinholes show open pore currents in the expected range, such as in Figure 3.2.11a, others contained pinholes and gave higher open pore currents than expected. The most striking example of the range of open pore currents measured is the device in Figure 3.2.11c. It should be noted that the device in Figure 3.2.11c gave the largest measured open pore current of all devices that still gave clear

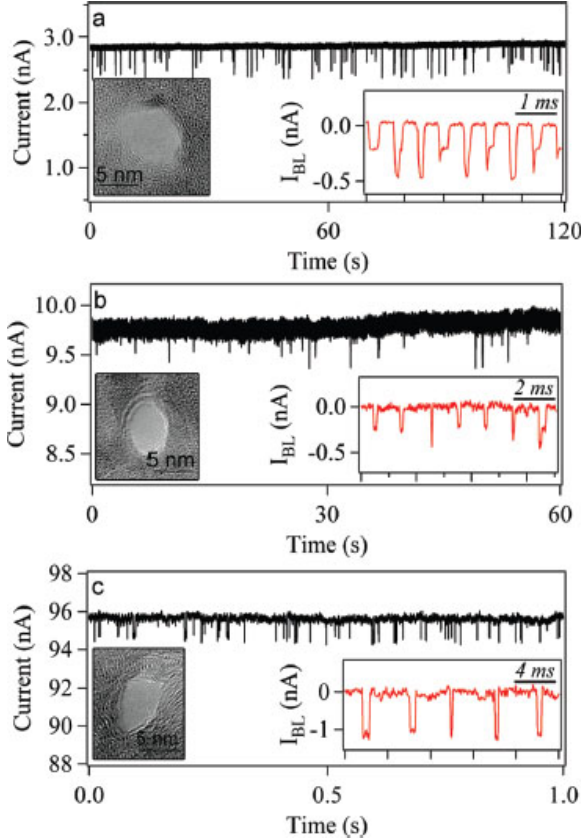


Figure 3.2.11: DNA translocations through graphene nanopores coated with 5 nm  $\text{TiO}_2$ . Time traces of ionic current showing DNA translocations for (a) a 7.5 nm nanopore with 1 nM 15 kbp dsDNA, (b) an 8 nm nanopore with 1 nM 15 kbp dsDNA, and (c) a  $5 \times 7$  nm nanopore with 20 nM 400 bp dsDNA. All devices were coated with 5 nm  $\text{TiO}_2$ . Left inset in each figure is a TEM image of the actual nanopores. Scale bars are 5 nm. Right inset in each figure shows a concatenated sequence of sample events with the open pore current subtracted.  $V_B$  for each trace is (a) 100, (b) 100, and (c) 150 mV.

translocation signals. Its inclusion is meant to demonstrate the large range of open pore currents that might be possible in functional devices. For this device we estimate, based on open pore currents and relative nanopore size, that the total pinhole area is 0.08% of the total suspended graphene area. This is a reasonable fraction given that this is the device with the largest open pore current. Rather than *a priori* excluding such devices, because of their larger-than-expected open pore currents, the devices were included here to show that measurable DNA translocation is still possible in devices containing pinholes. This is an important result because it demonstrates the tolerance for device fabrication and graphene quality. Using higher quality graphene (either CVD or exfoliated) or smaller areas of suspended graphene or eliminating the

UV/ozone process in favor of another method may improve the uniformity of open pore currents, if desired.

The data in parts a and b of Figure 3.2.11 show translocation of 15 kbp double-stranded DNA (dsDNA) through (a) a 7.5 nm and (b) an 8 nm diameter graphene-TiO<sub>2</sub> nanopore. A similar capture rate was observed when compared with bare graphene and SiN<sub>x</sub> nanopores.  $I_{BL}$  values between 200 and 400 pA were observed at  $V_B = 100$  mV for these two devices. The translocation of much shorter 400 bp dsDNA (Fermentas NoLimits, Glen Burnie, MD) was also measured, as shown in Figure 3.2.11c. Event lengths in Figure 3.2.11c are longer than expected, based on the data in parts a and b of Figure 3.2.11, due to the decrease in pore area<sup>144</sup> for this device. Here, mean  $I_{BL}$  values of over 1 nA are measured for  $V_B = 150$  mV. Translocation events for two different DNA lengths, 400 bp and 3000 bp, are additionally shown in Figure 3.2.12. The amplitude of folded entry ( $\sim 1.6$  nA) is approximately double the amplitude of unfolded entry ( $\sim 0.8$  nA), and the appearance of a large fraction of folded and unfolded translocations is in line with previous measurements in solid-state membranes.<sup>126</sup> Despite the differences in baseline current due to varying pinhole density for the pores in Figure 3.2.11, the functionality of the devices does not appear to be adversely affected. This is indicated by the similar range of  $I_{BL}$  depths for the devices shown in Figure 3.2.11, from  $\sim 500$  pA to 1.5 nA, even for devices with 2 orders of magnitude difference in open pore current, from  $\sim 3$  to 100 nA.

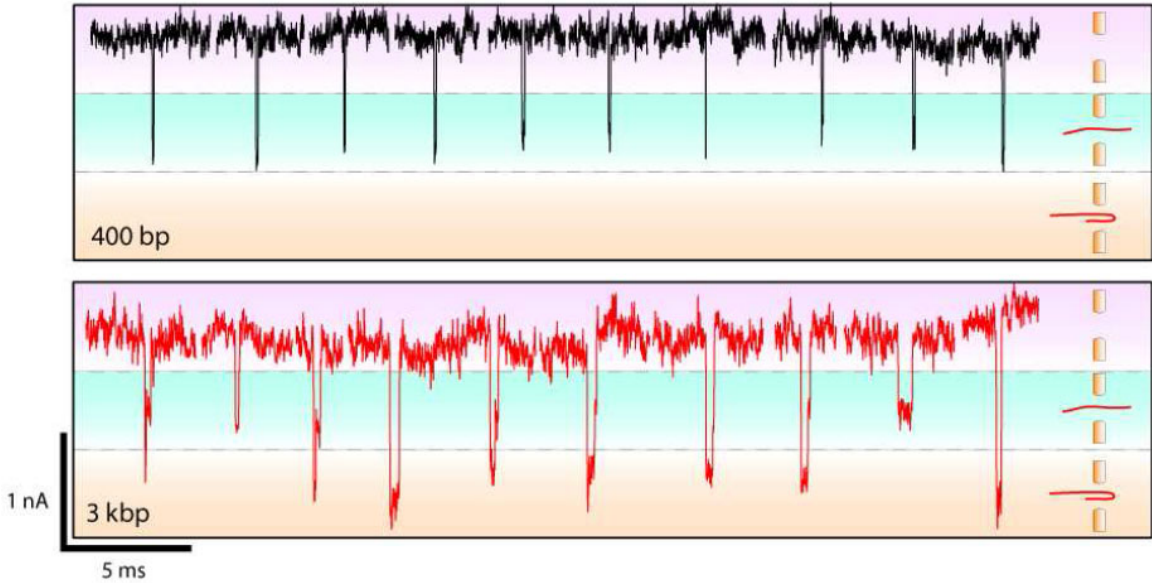


Figure 3.2.12: Translocation events for 400 and 3000 bp dsDNA with the  $\text{TiO}_2$ -coated graphene nanopore shown in Figure 3.2.11c. Top and bottom panels show data for 400 bp (same measurement presented in Figure 3.2.11c) and 3000 bp dsDNA, respectively. Events for the 400 bp exhibit a single characteristic amplitude, while some 3000 bp DNA events indicate folded entry of the DNA.<sup>130</sup> The amplitude of a folded entry ( $\sim 0.8$  nA) is approximately double the amplitude of unfolded entry ( $\sim 0.4$  nA), and the appearance of a large fraction of folded and unfolded translocations is in line with previous translocation measurements in silicon nitride membranes.

In Figure 3.2.13, two dimensional histograms of event length as a function of  $I_{BL}$  are given for 15 kbp dsDNA through a 6 nm graphene nanopore device at  $V_B =$  (a) 100 mV and (b) 400 mV. The device was coated with 5 nm of  $\text{TiO}_2$ , and 1100 and 1800 events were collected and analyzed for (a) and (b), respectively. There are two clear regimes visible in Figure 3.2.13a. Unfolded events are clustered at  $\sim 200$  pA and folded events are clustered at  $\sim 400$  pA, with a mean unfolded event length of  $\sim 200$  s. This corresponds to a translocation speed of 70 bases/ $\mu\text{s}$ . The events depicted in Figure 3.2.13b are faster and deeper than expected due to the increase in  $V_B$ . An

average  $I_{BL}$  of 1.5 nA at  $V_B = 400$  mV and a decreased mean translocation time of  $\sim 100$   $\mu$ s were measured. This is the minimum pulse duration measureable with the 10 kHz filter in this measurement setup, so the actual translocation time may be shorter.

From the histogram in Figure 3.2.13a, there is a clear peak in the blocked current at 200 pA for an applied bias voltage of 100 mV. Though the magnitude of  $I_{BL}$  is large based on the open pore current of 10 nA for this device, the blocked current is calculated to account for only 2% of the open pore current. This is one order of magnitude lower than the expected  $I_{BL}$  of 13%, based on a SiN<sub>x</sub> nanopore of the same diameter,<sup>144</sup> further supporting the existence of pinholes in the membrane which increase the baseline open pore current signal. Figure 3.2.13c shows the mean  $I_{BL}$  as a function of the applied bias voltage for the same device. Mean  $I_{BL}$  values are calculated from Gaussian fits to blocked current values, at each bias voltage, as demonstrated in Figure 3.2.14. The magnitude of the blocked current increases linearly with  $V_B$ , as previously observed in SiN<sub>x</sub> pores for DNA in the voltage regime tested.<sup>119</sup>

Mean translocation velocity,  $v_{DNA}$ , is plotted in Figure 3.2.13d as a function of  $V_B$ . The translocation velocity was observed to increase linearly with increasing applied bias voltage, as has been observed in SiN<sub>x</sub> nanopores.<sup>15</sup> Mean velocities,  $v_{DNA}$ , are calculated by fitting histograms of the measured event lengths at a given  $V_B$  and calculating velocity as the length of the molecule (in bases) divided by the most probable event length (in seconds). The event length histograms used to compute

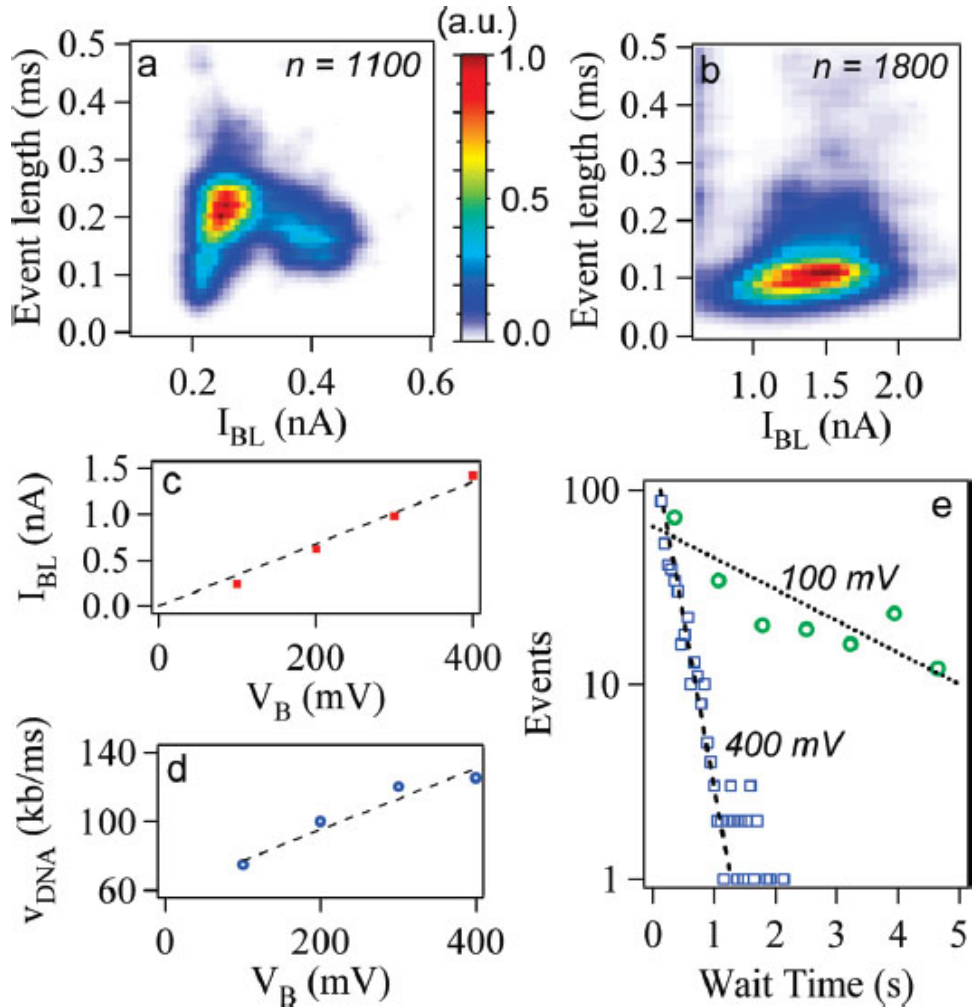


Figure 3.2.13: Characterization of translocation events for an 8 nm nanopore in a graphene membrane coated with 5 nm of  $\text{TiO}_2$ . (a) Two dimensional histogram of event length vs blocked currents for 15 kbp dsDNA at  $V_B = 100$  mV. The color scale corresponds to the normalized frequency of events. (b) Two dimensional histogram of event lengths vs blocked currents at  $V_B = 400$  mV. (c) Blocked current,  $I_{BL}$ , as a function of  $V_B$ .  $I_{BL}$  values (red squares) are extracted using a Gaussian fit from current histograms taken at each bias voltage. A linear fit is provided for reference (dashed black line). (d) Translocation velocity,  $v_{DNA}$ , as a function of  $V_B$ . Velocity values are computed using mean event length values at each bias voltage and DNA length. A linear fit is provided for reference (black dashed line). (e) Histogram of wait times for 250 events at  $V_B = 100$  mV (green circles) and 850 events at  $V_B = 400$  mV (blue squares). Data were fit with a Poisson distribution (black dashed line) of the form  $\Pi(\lambda, t) = c\lambda e^{-\lambda t}$ , with capture rates  $\lambda = 0.3 \text{ s}^{-1}$  for  $V_B = 100$  mV and  $\lambda = 4 \text{ s}^{-1}$  for  $V_B = 400$  mV, and  $c$  is a constant.

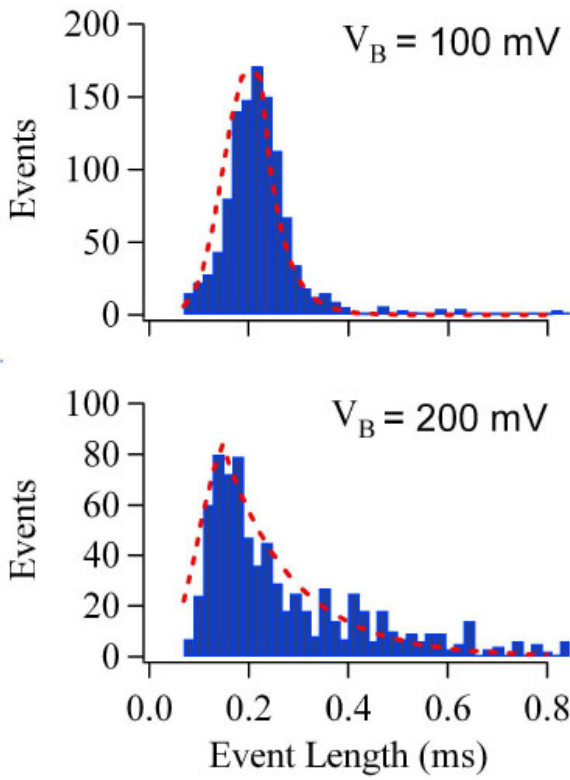
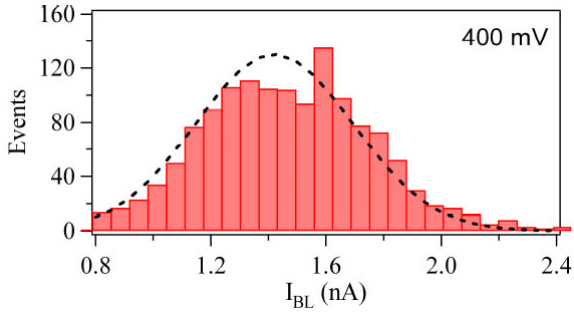
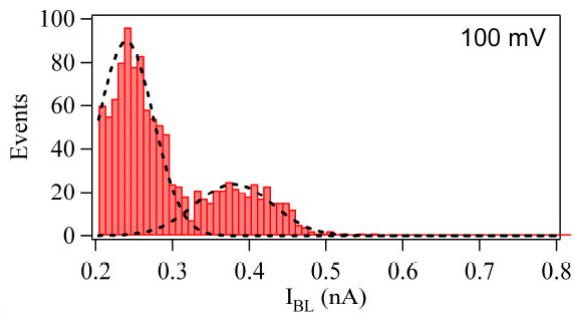


Figure 3.2.14: Ion current distributions for varying applied voltage. Mean  $I_{BL}$  as a function of bias voltage in Figure 3.2.13c is computed by fitting (black dashed line) a Gaussian to the distributions. Two peaks exist for  $V_B = 100$  mV for both folded and unfolded types of events.

Figure 3.2.15: Event length as a function of  $V_B$ . Translocation velocity as a function of bias voltage in Figure 3.2.13d is computed using most probable event length data for each bias voltage. This is derived by fitting (red dashed line) a Gaussian distribution to points before the most probable value and an exponential of the form  $e^{-t/\tau}$  to points after the most probable value for each bias voltage.

$v_{DNA}$  are given in Figure 3.2.15. A histogram of the wait time between consecutive events is given in Figure 3.2.13e for  $V_B = 100$  and  $400$  mV. In both cases the wait time follows a Poissonian distribution, indicative of the uncorrelated nature of the translocations.<sup>91</sup> Wait time decreases with increasing voltage because the distance from the pore at which DNA molecules are captured by the electric field increases with voltage.<sup>16</sup>

### 3.2.5 Summary

The first electronic measurements of DNA translocation through graphene nanopores are presented here. The current blocked by DNA translocation through graphene nanopores was found to be larger than what has been observed for SiN<sub>x</sub> nanopores of the same diameter, due to the thinness of the graphene membrane. However, bare graphene devices exhibited large ion current noise and suffered from low yield. This could be improved with the use of higher quality graphene material or smaller holes in the supporting SiN<sub>x</sub> membrane to minimize the suspended graphene area. Coating the graphene membrane with a thin TiO<sub>2</sub> layer reduced current noise and provided a more hydrophilic surface, enabling a study of the dynamics of DNA translocation through these pores. Trends of the translocation velocity, current blockage, and capture rate, as a function of applied bias voltage, agree with previous studies carried out with SiN<sub>x</sub> nanopores. Future work will focus on improving the overall reliability of these devices and on utilizing the conductivity of the graphene sheet to create

devices for probing DNA molecules.

## 3.3 Lowering Noise to Enable Increased Bandwidth

### 3.3.1 Introduction

Although differentiation between homopolymer signals is an important milestone towards validating nanopore DNA sequencing, further increases in temporal and spatial resolution are necessary to achieve differentiation of bases along a single DNA strand.

Because the current signals between bases differ by hundreds of pA,<sup>135</sup> solid-state nanopore sequencers must achieve less than this in pA<sub>rms</sub> noise to differentiate between nucleotides on the same DNA strand. Further, due to the typical DNA velocities inside a nanopore,<sup>127</sup> this low rms noise must be achieved while sampling at at least 20 MHz bandwidth to detect individual nucleotides.

The easiest method to achieve further improvements in the SNR of ssDNA translocating through solid-state nanopores is to address the highest noise source in the nanopore system. In the case of the silicon nitride nanopores described here, the largest contribution to noise in the nanopore system is the capacitive noise through the area of the nanopore chip exposed to ionic solution, as discussed in Section 2.2 and seen in Figures 2.2.1 and 2.2.2. The thick SiO<sub>2</sub> layer compensates for this, but the fabrication limitations constrain the thickness of this layer to 5  $\mu\text{m}$ , whereas to achieve sequencing-quality noise levels, this SiO<sub>2</sub> thickness must be orders of magni-

tude greater than this value.

In this section, a method of further reducing the nanopore chip capacitance is presented. Nanopore chip capacitances were reduced an order of magnitude from tens of pF to a few pF by the addition of a 100  $\mu\text{m}$  thick SU8 layer to the supporting nanopore chip. With this addition, the capacitance can be lowered enough that the chip capacitance is no longer the dominant noise source in the nanopore system. Figure 3.3.1a shows the dependencies of nanopore chip capacitance on membrane dimensions, membrane thickness, and silicone elastomer radius when the nanopore device is coated in a 100  $\mu\text{m}$  thick SU8 layer with a  $200 \times 200 \mu\text{m}$  window in the SU8 layer above the suspended membrane. Figure 3.3.1b shows the equivalent circuit diagram used to calculate the chip capacitance.

### 3.3.2 Experimental Methods

Nanopore membranes were fabricated as described in Section 2.1 using 42 nm thick silicon nitride. The membranes were designed to be smaller than previously used membranes - between  $1 \times 1$  and  $20 \times 20 \mu\text{m}$  squares. The chemical etch used to remove the  $\text{SiO}_2$  layer is isotropic, which adds an additional 10  $\mu\text{m}$  to each membrane dimension. This etching can be seen in Figure 3.3.2 as a ring around the membrane where the  $\text{SiO}_2$  was etched from between the silicon and  $\text{SiN}_x$  layers. Smaller membranes were used because larger membranes create a larger area of suspended thin dielectric that increases the chip capacitance. Before the nanopore was drilled, an

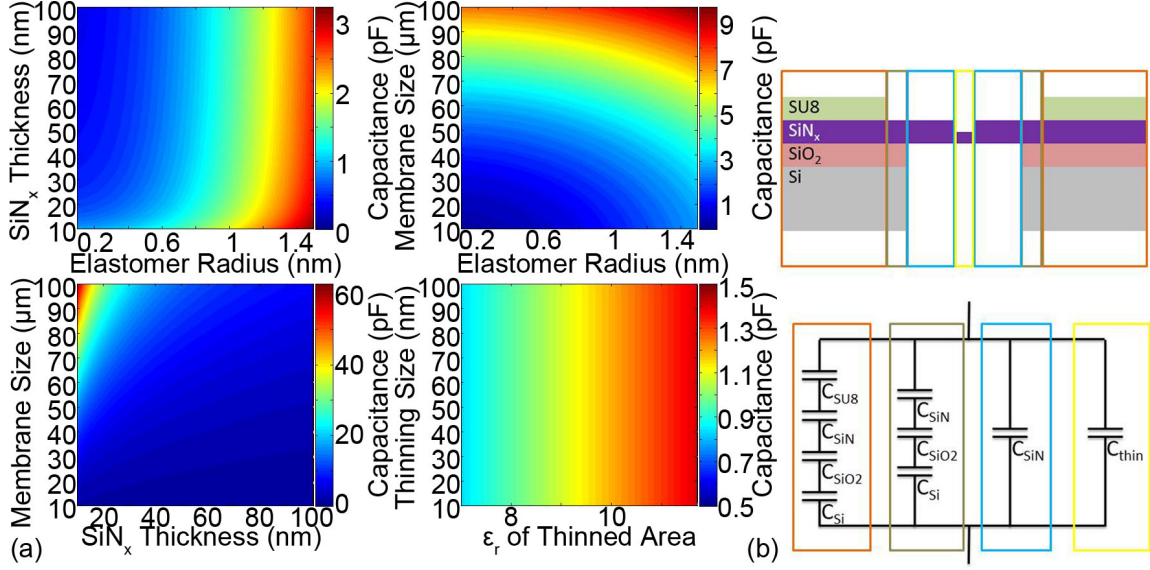


Figure 3.3.1: (a) the theoretical chip capacitance for SU8-coated nanopore devices. Graphs show the effect on capacitance of the silicon nitride thickness versus the exposed radius of the membrane not covered by silicone elastomer (top left), side length of the square membrane versus the silicon nitride thickness (lower left), side length of the square membrane versus the exposed radius of the membrane not covered by silicone elastomer (top right), and the side length of the square thinned area of the membrane versus the dielectric constant of the thinned area, ranging from silicon nitride (7) to silicon (11.7) (bottom right). The capacitance was calculated using the equivalent circuit diagram shown in (b). In each graph, all other parameters are held constant at 20 nm for the thickness of the thinned region, 100 nm for the side length of a square thinned region, 1 mm for the silicone elastomer radius, 10 nm for the side length of a square membrane, and 42 nm for the silicon nitride membrane thickness.

additional layer of 100 μm thick SU8 was added to the membrane side of the nanopore chip, and photolithography was used to expose a 200 × 200 μm square around the membrane. The TEM used for nanopore drilling has a range of motion normal to the nanopore surface of ±100 μm, which limits the thickness of SU8 that can be deposited on a chip prior to nanopore drilling in the TEM. If the SU8 is made thicker, the TEM cannot reach the plane of focus of the membrane to drill a nanopore.

After SU8 patterning, 20 × 20 nm regions of the membranes were thinned using

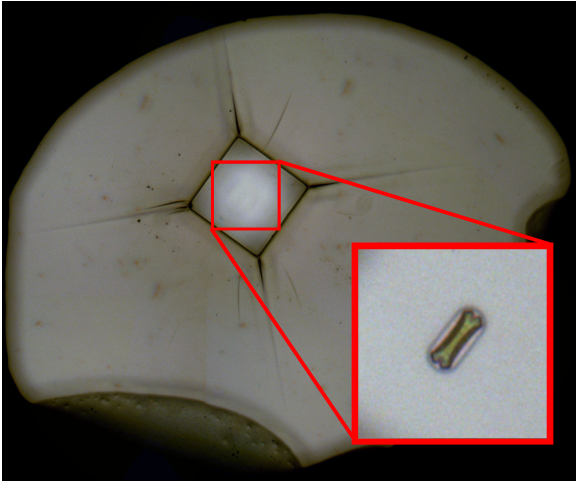


Figure 3.3.2: Optical image of an SU8-coated nanopore chip. The black area is covered with silicone elastomer. The black square is the edge of the SU8. The inset shows the silicon nitride membrane inside the uncoated square. The rim around the membrane is the edge of the isotropically etched  $\text{SiO}_2$  underneath the silicon nitride.

scanning TEM (STEM, see Section 5.3 for details), and a nanopore was drilled in the thinned region. Although plasma etching-based nanopore thinning employed previously<sup>135,142</sup> enables parallel processing of many nanopore membranes at once whereas STEM thinning must be done in series, the SU8 was found to have poor adhesion to nanopores thinned using the former method. The cause of this delamination is believed to be residues of the lithography processes left on the chip even after piranha cleaning. Because STEM thinning can be performed after SU8 deposition and requires no resist patterning, delamination of chips that employed STEM thinning was seen much more rarely (24% of chips) than in chips thinned by plasma etching (67% of chips).

STEM thinning alters the composition of the thinned area from silicon nitride to more pure silicon. Silicon has a lower knock out energy compared to nitride because silicon is a lighter element. Due to this effect, nitride is ablated more rapidly than silicon. Although this will increase the chip capacitance, the small size of the thinned region makes this contribution to the chip capacitance negligible. Figure 3.3.1 shows

the nanopore device capacitance as a function of thinned area relative permittivity, ranging from 7 for  $\text{SiN}_x$  to 11.7 for silicon.

After nanopore drilling, chips were sealed onto the PTFE measurement cell using silicone elastomer, and the elastomer was painted as close to the window as possible. Figure 3.3.2 shows an optical microscopy image of an SU8-coated nanopore device with silicone elastomer painted near the membrane. The chip and cell were then cleaned with oxygen plasma before the complete cell was assembled and 1 M KCl was added to both chambers. Piranha cleaning could not be used on these chips because piranha would dissolve the organic SU8 layer.

### 3.3.3 Capacitance and Noise Measurements

Capacitance was measured by applying a triangle wave voltage potential across the nanopore and measuring the resulting square wave potential. Recall from Equation 4.4 that current is proportional to the derivative of voltage, and the proportionality constant is capacitance. Figure 3.3.3a shows an example of the triangle wave voltage input and its resulting square wave output. The amplifier was calibrated with a 10 pF capacitor, and found to be accurate with an error of approximately  $\pm 0.5$  pF.

Three of the devices measured produced a stable open pore current with a capacitance near or below 10 pF. Figure 3.3.3b shows the four devices, their measured capacitance, and their theoretical capacitance calculated using measured values of the silicone painted radius, SU8 thickness and exposed area, membrane size, and thinned

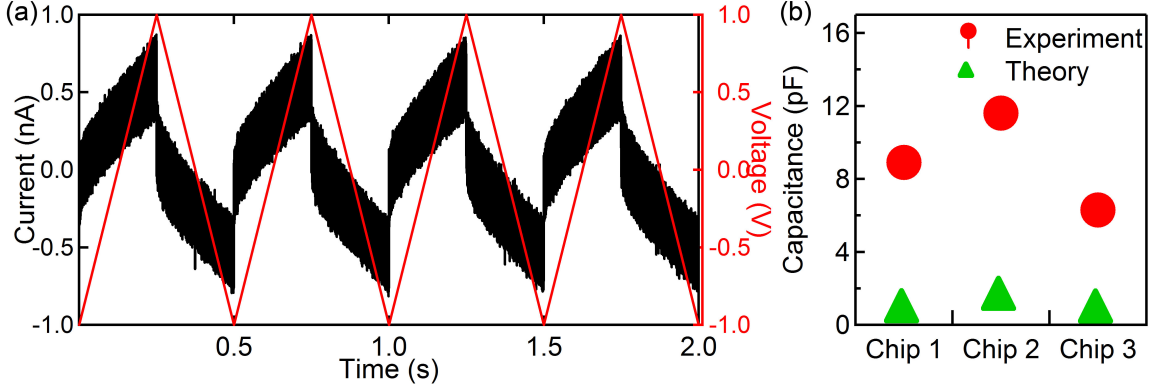


Figure 3.3.3: (a) raw current vs time and voltage vs time traces used to find the capacitance of nanopore devices. In a pure capacitor, a triangle wave voltage input creates a square wave current output. By measuring the square wave jump and using 4.4, capacitance can be calculated. (b) Capacitance results of three SU8-coated nanopore devices. All three showed stable open pore current. Experimental results are shown in red, and theoretical capacitances are shown in green.

area. Although in all cases the measured capacitance is higher than the theoretical capacitance, it should be noted that the theoretical capacitance is an idealized minimum capacitance of the experimental parameters. The experimental capacitance is further suspected to be higher due to local delamination of the SU8 coating near the suspended membrane. This local delamination allows ionic solution to seep under the SU8 layer and negate the SU8 layers capacitance reducing effects in that region. Further, the theoretical calculations of capacitance assume the chip area covered with silicone elastomer has a negligible contribution to the capacitance. At the edges of the silicone elastomer where the elastomer thins, this may not be an accurate assumption. The total rms noise as a function of frequency was also measured for all SU8-coated devices. Figure 3.3.4 shows the power spectral density (b) and the integrated rms noise (a) for a typical SU8-coated device. The rms noise value at 1 MHz bandwidth

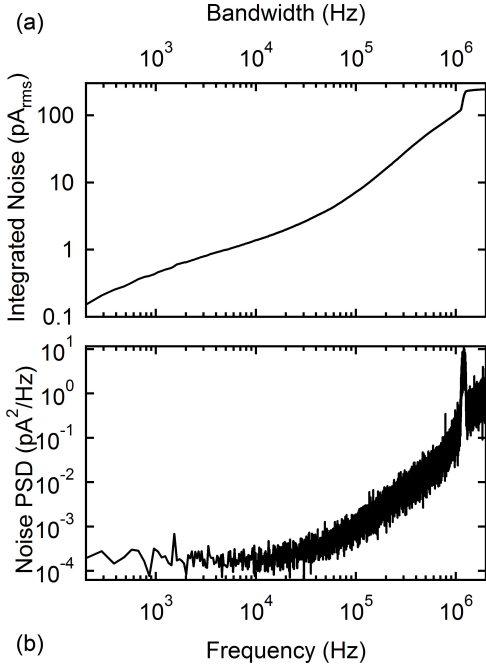


Figure 3.3.4: (a) the cumulative integral of the power spectral density of the noise (b). The power spectral density of the noise is the Fourier transform of the autocorrelation function of the current vs time trace and the cumulative integral of the power spectral density shows the expected rms noise when measuring at a given bandwidth.

is 105.3 pA<sub>rms</sub>,  $\sim$  400 pA<sub>rms</sub> lower than previously reported low-noise systems.<sup>135</sup> The average rms noise value at 1 MHz bandwidth was 214 pA<sub>rms</sub>,  $\sim$  300 pA<sub>rms</sub> lower than previously reported.<sup>135</sup>

### 3.3.4 Summary

This section discussed the noise and capacitance reduction associated with the addition of an SU8 layer to the nanopore device. Although the capacitance of SU8-coated nanopore devices is higher than anticipated, further refinements in SU8 adhesion and thicker and more precise coatings with silicone elastomer should reduce this value. The addition of an SU8 layer has accomplished an approximately four-fold reduction in nanopore chip capacitance from standard silicon nitride devices with 40 - 100 pF capacitance, resulting in a 300 pA<sub>rms</sub> reduction of noise at a measurement bandwidth

of 1 MHz.<sup>135</sup> Future work combining ultra-thin nanopores through SU8-coated devices with on-chip amplifier electronics will reach sub-100 pA<sub>rms</sub> noise levels at 1 MHz bandwidth.

### 3.4 Conclusions

This chapter has discussed the improvements made to nanopore detection limits. Temporal resolution was improved by using a new low-noise, high-bandwidth amplifier from Chimera Instruments. Spatial resolution was improved by thinning nanopore membranes to less than 10 nm and using graphene as a thin membrane material. For the first time, homopolymer differentiation was observed using solid-state nanopores, which is a key milestone in validating nanopores as DNA sequencers. During these measurements, a deeper insight into DNA translocation dynamics was achieved when adenine was found to have a wider distribution of event depths. As adenine is physically the largest base of the three studied, this suggests that the adenine molecule explores its larger conformational space while inside the nanopore. Nanopore sensors were further improved by the addition of a dielectric layer to the supporting chip. This refinement allowed the use of sub-10 pF nanopore chips. Further improvements in these directions will enable not only nanopore-based sequencing, but nanopore-based characterization of smaller biomolecules and inorganic nanoparticles.

# CHAPTER 4

## Nanopores for Nanoparticle Synthesis and Characterization

### 4.1 Introduction to Nanoparticles

Although great emphasis has been placed on the application of nanopore sensors to DNA sequencing, nanopore sensors are ideal tools for the characterization of any molecule or material in the nanometer size regime. In particular, metallic nanoparticles are ideal candidates for nanopore characterization. Metallic nanoparticles are nanometer-scale particles often created by the reduction of a metal compound to solid metal. The aggregation of metal is stopped using a capping agent, often a ligand. Metallic nanoparticles are frequently suspended in water using a charged ligand, range in size from a few hundred nanometers to a few nanometers, and come in a variety of shapes. Gold nanoparticles currently show great promise for applications in biological tagging<sup>24,53</sup> and drug delivery.<sup>44</sup>

Nanopores can aid in nanoparticle research in a variety of ways, and because solid-state nanopores can be drilled to a custom diameter, they can probe any nanoparticle size regime. To the author's knowledge, previous to the work presented here, nanoparticle formation had not been studied *in situ*, but using nanopores as small-volume

reactions, nanopores enabled nanoparticle formation studies. Nanoparticles are also difficult to precisely place or align, but using nanopore, nanoparticles can be templated in precise positions, and complex geometries such as alternating nanoparticle material compositions could be possible. Additionally, the coverage of surface ligands on anisotropic nanoparticles cannot be easily measured using traditional methods.<sup>28</sup> Using nanopores in their original application, as nanometer-scale Coulter counters, the surface charge density of anisotropic nanoparticles coated in charged ligands can be obtained. The following sections outline some of the ways nanopore sensors can aid in nanoparticle research and characterization.

## 4.2 Growing Nanoparticles using Nanopore Tem- plates

### 4.2.1 Introduction

Methods for fabricating nanoparticles generally rely on either bottom-up approaches,<sup>7,47,54,97,112,128</sup> which are generally limited in the exact positioning of nanoparticles on a chip, or top-down approaches based on electron beam lithography,<sup>22,37</sup> which are limited in the smallest particle size that can be achieved. Confining chemical reactions by limiting reagent access is another approach to synthesizing nanostructures and has been used to make organic particles in solution,<sup>41</sup> high aspect ratio nanowires,<sup>116</sup> electrofunctionalized micropores<sup>9</sup> as well as studies of

precipitation-induced ion current fluctuations in nanopores<sup>55</sup> and related mathematical modeling.<sup>147</sup> Controllable synthesis could be useful for a range of applications including transport measurements, self-assembly and catalysis. While solid-state nanopores have been mostly used for studies of electric-field-driven translocations of single molecules through the pores, these pores are nm-size regions placed at desired locations on a solid-state chip and are thus unique candidates for studies of chemical reactions in confined volumes.

This section discusses the use of nanopores as sub-zeptoliter mixing volumes for the controlled synthesis of metal nanoparticles. The nanopores are pre-drilled with the TEM near thinned marker regions patterned on a silicon nitride membrane. These markers help us locate a single nanopore on a silicon nitride membrane. Particle synthesis is controlled and monitored through an electric field applied across the nanopore membrane, which is positioned so as to separate electrolyte solutions of a metal precursor and a reducing agent. When the electric field drives reactive ions to the nanopore, a characteristic drop in the ion current is observed, indicating the formation of a nanoparticle inside the nanopore. The resulting nanoparticles are then found in the TEM using the reference markers and imaged with atomic scale resolution. While traditional chemical synthesis relies on temperature and timing to monitor particle growth, using the method presented here it is observed in real time by monitoring electrical current. The dynamics of gold particle formation in sub-10 nm diameter silicon nitride pores are described and the effects of salt concentration

and additives on the particles shape and size are investigated. The current vs. time signal during particle formation in the nanopore is in excellent agreement with the Richards growth curve indicating an access-limited growth mechanism.

#### 4.2.2 Overview of the Method

Nanopores with diameters ranging from 4 nm to 20 nm fabricated in silicon nitride ( $\text{SiN}_x$ ) membranes were used for this experiment. Figures 4.2.1a and 4.2.1b are TEM images of a single 6.5 nm diameter nanopore and a larger view showing four 200 nm large pre-patterned reference regions where  $\text{SiN}_x$  was etched. Markers were patterned by thinning squares in the membrane (Figure 4.2.1b) using electron beam lithography followed by reactive ion etching.<sup>142</sup>

The nanoparticle synthesis procedure inside the nanopore is illustrated in Figures 4.2.1 d-f. To begin, the  $\text{SiN}_x$  membrane was placed in a measurement setup so that it divided two 100  $\mu\text{L}$  PTFE chambers (designated A and B) of salt solution, and a Ag/AgCl electrode was placed in each chamber (Figure 4.2.1d). Potassium chloride (KCl) solutions with concentrations from 5mM to 1M were used as an electrolyte for measuring current through the pore. Application of a voltage difference  $\Delta V$  in the range of a few hundred mV provided an electric field through the pore, which was enough to drive measureable ion current (of the order of a few nA) across the nanopore. For Au particle synthesis, while keeping  $\Delta V < 0$ , 20  $\mu\text{L}$  of a 5 mg/mL solution of  $\text{HAuCl}_4$  (gold (III) chloride) were added to chamber A, and the solution in

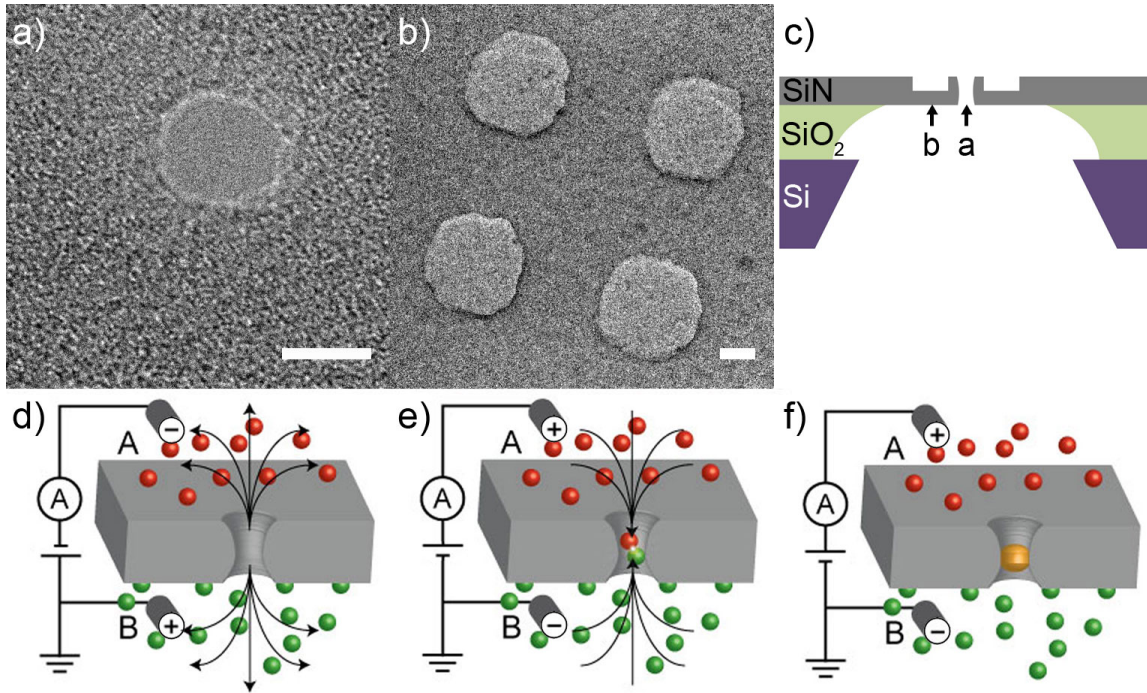
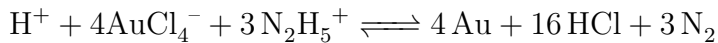


Figure 4.2.1: Electric-field-driven nanoparticle synthesis in a nanopore. (a) TEM image of a 6.5 nm diameter nanopore in a  $\text{SiN}_x$  membrane. Scale bar is 5 nm. (b) Lower magnification TEM image of a  $\text{SiN}_x$  membrane. Membrane is pre-patterned and thinned to form 200 nm x 200 nm square regions (light grey) used as markers. Scale bar is 100 nm. (c) Schematic of the membrane and support structure (not to scale). (d) (f) Schematics of the particle growth process: (d) a  $\text{SiN}_x$  membrane with a single nanometer-size pore separates two chambers, A and B, of electrolyte. For Au synthesis, negatively charged gold (III) chloride is injected in chamber A, and positively charged hydrazine is injected in chamber B. At first, a potential applied across the chambers prevents the solutions from reacting. (e) The reaction is triggered by reversing the sign of the voltage difference, which drives the reagents in to the pore where they react. (f) As the reagents react, a gold nanoparticle forms in the pore, and in the process stops further reaction by preventing the reagents from mixing.

chamber B was exchanged for 0.1 mass percent hydrazine solution, giving final concentrations of 2.94 mM  $\text{HAuCl}_4$  and 0.0312 mM hydrazine. These concentrations were chosen after varying the gold chloride concentration to find the value that minimized the time to form a particle (see Figure 4.2.2). Due to the safety hazards associated

with hydrazine and practical concerns, the hydrazine concentration was not increased further.  $\text{AuCl}_4^-$  is negatively charged at neutral pH, and hydrazine is a strong reducing agent that has a positive charge at neutral pH ( $pK_a = 7.99$ ).<sup>8</sup> Therefore, keeping  $\Delta V < 0$  mutually prevents the mixing of both reagents in the pore, shown in Figure 4.2.1d. In some experiments, 3.1 mM gold chloride in water was mixed with 0.03 M  $\alpha$ -lipoic acid in water in a 2:1 ratio. The  $\alpha$ -lipoic acid and gold form a complex that was used in place of the gold chloride, in the same volumes. To trigger particle nucleation at a desired moment, the sign of  $\Delta V$  was suddenly reversed to a positive value, and both hydrazine and gold (III) chloride ions were driven through the pore, where the following reaction takes place in the confined pore environment to form a gold particle (see Figure 4.2.1e):



The formation of gold in the pore is self-limiting, i.e., when gold completely fills the pore, the reagents can no longer access each other, and the reaction stops (Figure 4.2.1f). Both stock solutions of reagents were dissolved in the same molarity of KCl as the experiments electrolyte. All experiments were performed at room temperature. Pores were reused for multiple experiments by soaking them in aqua regia for ten minutes to remove the gold particle. Additionally, control experiments were performed in which only one chamber was filled with reagent, i.e. either hydrazine was present but gold chloride was not, or gold chloride was present but hydrazine was not (see Figure 4.2.3). In all cases, the conductance after the voltage polarity

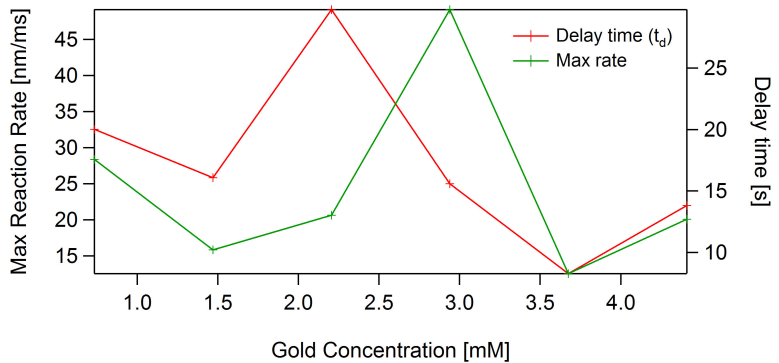


Figure 4.2.2: Delay time ( $t_d$ , red) and maximum reaction rate (green) vs. gold chloride concentration. These experiments were carried out on a 5 nm diameter pore in 5 mM KCl solution with 0.0312 mM hydrazine concentration. We chose to carry out all further experiments at a gold chloride concentration of 2.94 mM, as this concentration shows the fastest particle formation, i.e., the fastest reaction rate and one of the lowest delay times before particle formation begins.

was switched remained nonzero and approximately equal to the initial conductance, indicating that the pore remained open and no particle formed.

### 4.2.3 Discussion of the Current Signals

Prior to particle synthesis, the measured ionic conductance was first checked to agree with expected values based on the salt concentration and pore size determined by TEM imaging or conductance measurements<sup>121</sup> from previous particle formation experiments. For example, for a nanopore with a diameter of 5 nm, SiN<sub>x</sub> thickness of 25 nm, and 1M KCl solution, ion conductance was expected to be in the range of 7-8 nS. An I-V curve measured through a 15 nm diameter nanopore in 5 mM KCl solution is shown in Figure 4.2.4a (red line). The offset in the I-V trace was attributed to an offset in the electronics, which could be corrected by recalibrating the amplifier offset.

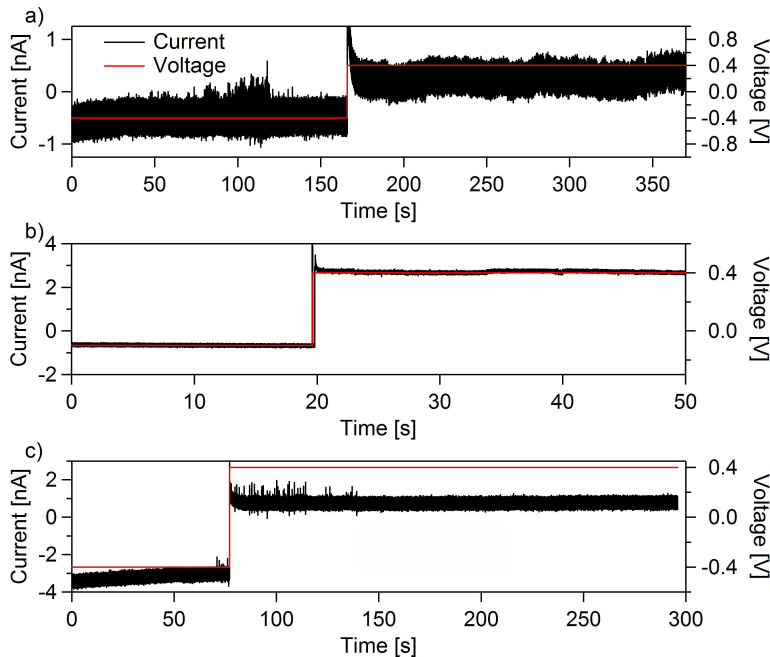


Figure 4.2.3: Control experiment graphs of current vs. time and voltage vs. time for (a) hydrazine, (b) gold, and (c) gold/ $\alpha$ -lipoic acid complex. The conductivity remains approximately the same after the voltage is changed, indicating that the pore remains open.

Figure 4.2.4b shows a voltage ( $\Delta V$ ) vs. time trace and the corresponding ion current ( $I$ ) vs. time trace during one experiment to form a gold nanoparticle in a 4.2 nm diameter nanopore. In over 80 repeated experiments performed on over 10 nanopores, the current trace during the growth of a particle was found to follow a characteristic time trace described here. In this example, in the first  $\sim 20$  s (Figure 4.2.4b) the chambers contained the 5 mM KCl solution with no precursors present, and  $I = -0.31$  nA for  $\Delta V = -100$  mV. At  $t = 5$  s, while keeping  $\Delta V$  constant and negative, hydrazine was injected to chamber A and  $I$  changed to  $-0.11$  nA (labeled 1 in Figure 4.2.4b). The ion current shifted to a smaller value when hydrazine was added because the hydrazine created a chemical gradient that changed the ionic current flow through the pore. At  $t = 10$  s, gold chloride was injected in chamber B, resulting in another current shift to  $-0.30$  nA (labeled 2 in Figure 4.2.4b). The chemical reaction

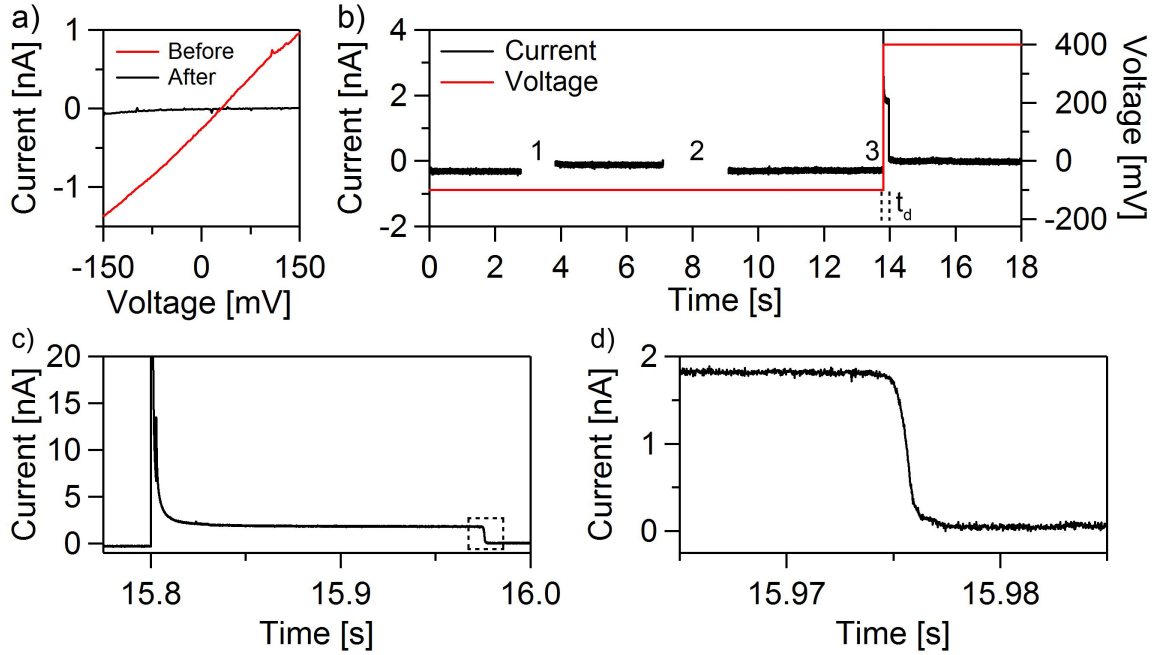


Figure 4.2.4: I-V traces and current vs. time traces during Au nanoparticle formation. (a) I-V traces for a nanopore before (red) and after (black) particle formation. For the empty pore trace, the ion current was measured in a solution of 5 mM KCl, without any hydrazine, gold chloride, or  $\alpha$ -lipoic acid. (b) Current vs. time trace and corresponding voltage vs. time trace for a nanoparticle formation experiment on a 4.2 nm diameter pore in 5 mM KCl solution. (1) Hydrazine is injected to chamber B. The ion current shifts due to the chemical gradient that has formed. (2) Gold chloride is added to the chamber A, and the current again shifts. (3) Voltage polarity is reversed in order to electrically drive the reagents into the pore. The vertical dashed lines after (3) represent the time delay,  $t_d$ , before particle formation. The current then drops to zero when the particle forms. (c) Zoom in of trace from voltage change to particle formation. The current spike is due to a capacitive response in the system. (d) Zoom in from the dashed square in (c) highlighting the particle formation event. In over 80 experiments, these events display this characteristic sigmoid shape.

was triggered at  $t = 15.8$  s by changing the polarity of  $\Delta V$  from  $-100$  mV to  $+400$  mV (labeled 3 in Figure 4.2.4b). This sudden voltage change was accompanied by an initial current spike due to a capacitive response in the electrical circuit when voltage was changed, followed by particle formation which was indicated by a sudden current

drop to zero. The current spike and particle formation are shown in Figure 4.2.4c. The capacitive response is slower than the sampling time of 20  $\mu$ s, and an exponential fit to this response gives an equivalent RC time of  $\sim 0.4$  ms. This is a well-known response that is seen when voltage is changed across a capacitor/resistive nanopore interface, and is also present in control measurements, in which no particles were formed (see Figure 4.2.3). The thick SiO<sub>2</sub> layer was specifically added to minimize capacitance thus reducing the RC time constant.

I-V traces were performed before adding reagents (to prevent particle formation at positive  $\Delta V$ ) and after the experiment to verify that the particle has formed and fills the pore (Figure 4.2.4a). After changing the voltage, the conductance is within the noise level of zero, and from a linear fit to the two lines is approximately 2% its original value, indicating the pore is now filled.

Figure 4.2.4d shows a magnified portion of the dashed box in the trace in Figure 4.2.4c that illustrates the ionic current readout of the particle formation process that follows this voltage change. In the left portion of the trace shown in Figure 4.2.4d ( $t < 15.975$  s) the nanopore is completely open, as indicated by a constant current value ( $I \sim 1.8$  nA at 400 mV). As gold nucleates, it blocks ions from traversing the pore, and the ionic current decreases ( $15.975$  s  $< t < 15.98$  s, Figure 4.2.4d). Another event time trace is shown in Figure 4.2.5a (black trace), and the derivative of that traces fit (Figure 4.2.5b). The trace in Figure 4.2.5a shows the same characteristics. Additionally, in Figure 4.2.5b, the rate of current change  $dI/dt$  is plotted. This rate

(and thus particle growth) greatly decreases at first as the nucleating cluster grows larger, until the particle is large enough to hinder incoming reagents from reacting, at which point particle growth slows down. When the gold nanoparticle completely fills the pore, ions and reagents can no longer traverse the pore, the ionic current stabilizes at zero, and the reaction stops ( $15.98s < t$ , Figure 4.2.4b). Therefore, this reaction in the pore is self-limiting. Particles formed using this method are embedded in the membrane and confined to the nanopore volume, as confirmed by TEM imaging discussed below.

#### 4.2.4 Proposition of a Growth Model

This sigmoid time dependence of the ion current during particle formation is very different from the sharp ion current decrease that is typically observed in biomolecular translocation as the biomolecule blocks the pore.<sup>48,59,132,140</sup> Below a model is presented that explains these observations. Precipitation of cobalt hydrogen phosphate in a nanopore was previously modeled for conical polyethylene terephthalate nanopores of similar minimum radii,<sup>147</sup> but the different experimental conditions, materials, and pore geometry in the experiment presented here suggest the need for a different model. The current signal observed here is found to be well described by the sigmoid Richards growth curve.<sup>111</sup> This curve was originally developed as a general model for biological growth, but it is applicable to this situation. The rate of particle growth is determined by the rate at which it accumulates gold from reagents, just as the rate of

an organisms growth is determined by the rate at which it accumulates weight from food. The generalized equation is the solution to the differential equation

$$\frac{dW}{dt} = \eta W^m - \kappa W \quad (4.1)$$

Where  $W$  is an organism's weight,  $t$  is time,  $\eta$  is the anabolic constant,  $\kappa$  is the catabolic constant, and  $m$  is an exponent determined by the biological situation. In the comparable case described here,  $W$  is the gold nanoparticles radius,  $r$ ,  $\eta$  is the particle growth constant, and  $\kappa$  is a constraint constant that represents the difficulty for reagents to meet in the narrow pore environment. Here the particles growth rate is assumed to depend on its cross-sectional area only. The force on the reagents drives them into the pore, where they encounter the particles cross-section, but there is no driving force pushing reagents to the sides of the particle parallel to the pore walls. Thus the value of the exponent  $m$  is 2. The constraint term  $\kappa W$  is linear in radius because it depends on the length of the pore region that is constricted by the presence of the particle. In the case of  $m = 2$ , the solution to equation 4.1 is called the autocatalytic function:

$$r(t) = A(1 + be^{\kappa t})^{-1} \quad (4.2)$$

Where  $A = \kappa/\eta$ ,  $b = 1 - \kappa/(\eta r_0)$ , and  $r_0$  is the radius of the nuclear particle. Since ionic current was measured instead of pore size, and the ionic current through the pore is approximately proportional to the cross-sectional area, the ionic current

is given by

$$I(t) = C(\pi r_{pore}^2 - \pi r^2(t)) = I_0 \left( 1 - \frac{A_{scaled}}{(1 + be^{\kappa t})^2} \right) \quad (4.3)$$

Where  $C$  is the proportionality constant,  $I_0$  is the open pore current and  $A_{scaled} = A^2/r_{pore}^2$ . Over 80 particle growth time traces were fit to this equation. A fit to the current vs. time data using this model is shown in Figure 4.2.5a. From Gaussian fits to the experimental values the value of  $\eta$  in these experiments was found to be  $40 \pm 1 \text{ nm}^{-1}\text{s}^{-1}$ , and the value of  $\kappa$  to be  $510 \pm 50 \text{ s}^{-1}$ . Furthermore, from the derivative of these fits (Figure 4.2.5b), the full width at half max (FWHM) of the curves can be extracted, which quantifies the duration of the particles formation, and the maximum growth rate of the particle. The FWHM was found to be  $0.7 \pm 0.6 \text{ ms}$ , and the maximum growth rate was found to be  $0.49 \pm 0.05 \text{ nm/ms}$ . While to the author's knowledge values for  $\eta$  and  $\kappa$  have never been found experimentally, these values of duration and reaction rate are much smaller than the timescales on the order of minutes and nanometers per minute, respectively, that have previously been reported for chemical synthesis.<sup>83,105</sup> To explain this, a postulate that the different kinetics is due to the driving force of the applied voltage, which pushes reagents together faster than random diffusion is proposed.

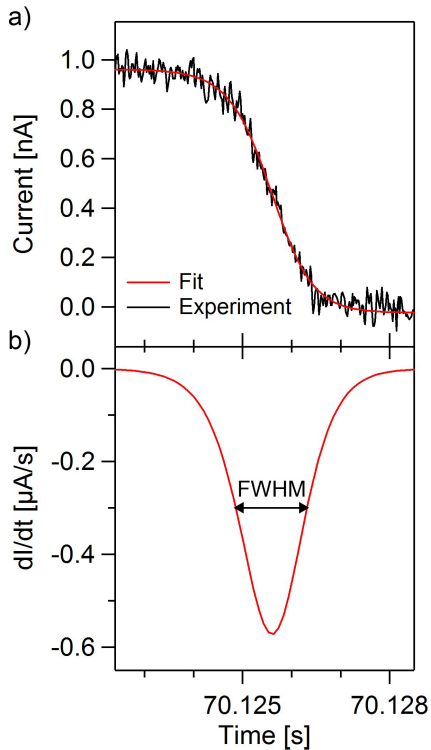


Figure 4.2.5: Richards model fit of gold nanoparticle formation event inside a nanopore. (a) Fit to equation 4.3 of a particle formation event. Experiment was performed on a 4.2 nm diameter pore in 5 mM KCl. Voltage applied during formation was 300 mV. (b) Derivative of the fit,  $dI/dt$ , is shown in panel a. The full width at half max gives a quantitative measure of the duration of particle growth.

#### 4.2.5 Examining the Reaction Time Delay

During these experiments, a time delay,  $t_d$ , of up to  $\sim 130$  s is observed between changing the voltage polarity and recording particle formation, shown as dashed lines in Figure 4.2.4b. This delay likely results from the stochastic nature of particle nucleation and formation at the surface of the pore, as observed in other precipitation experiments.<sup>55</sup> It represents the average time for a particle to nucleate large enough to stick in the pore. However, during this time, additional gold may form around the pore due to reagents and smaller gold particles that have time to traverse the pore before it fills. Reduction of this delay is thus crucial for eliminating additional particle formation at undesired places and for the particles confinement to the pore

volume.

A reduction in the ionic strength of the electrolyte solution can be used to effectively reduce  $t_d$ . To quantify this effect,  $t_d$  was recorded for each experiment in KCl concentrations of 5 mM, 50 mM, and 1 M. Figure 4.2.6 shows  $t_d$  histograms for each KCl concentration from these experiments. 87.5 % of  $t_d$  values were below 40 s, the maximum time displayed in Figure 4.2.6, for 1 M KCl, 83.9 % were below 40s for 50 mM KCl, and all values were below 40s for 5 mM KCl. By decreasing the concentration of KCl in solution from 1 M to 50 mM or 5 mM,  $t_d$  was found to decrease by 1 to 2 orders of magnitude: for 1 M,  $t_d = 15 \pm 1$  s; for 50 mM  $t_d = 2.3 \pm 0.5$  s; and for 5 mM  $t_d = 0.8 \pm 0.2$  s. These  $t_d$  values were extracted from Poisson fits. Decreasing the salt concentration increases the probability that any two oppositely charged ions interacting in the pore are reagents, thus increasing the reaction rate. The effect of pore diameter on  $t_d$  was also studied, but no observable trend was found (see Figure 4.2.7).

#### 4.2.6 Effects of a Capping Agent

The effect of surface-capping additives on nanoparticle synthesis in a nanopore was also explored. Adding an organic molecule that binds to gold was found to help limit particle growth outside the pore. This method is used extensively for controlling the growth of nanoparticles in solution,<sup>11</sup> and its application extends well to particle growth inside nanopores. The additive  $\alpha$ -lipoic acid was used as described above,

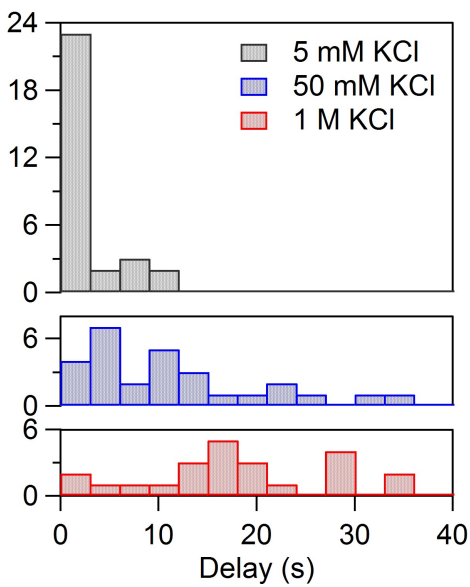


Figure 4.2.6: Histogram of the measured time delays,  $t_d$ ;  $t_d$  is the time elapsed between the time when voltage polarity is reversed and the time when ion current goes to zero and the particle fills the pore completely. Data is shown for three different salt (KCl) concentrations: 5 mM (grey, top), 50 mM (blue, middle), and 1 M (red, bottom). The concentrations of reactants were held constant. From Poisson fits: for 1 M,  $t_d = 15 \pm 1$  s; for 50 mM  $t_d = 2.3 \pm 0.5$  s; and for 5 mM  $t_d = 0.8 \pm 0.2$  s.

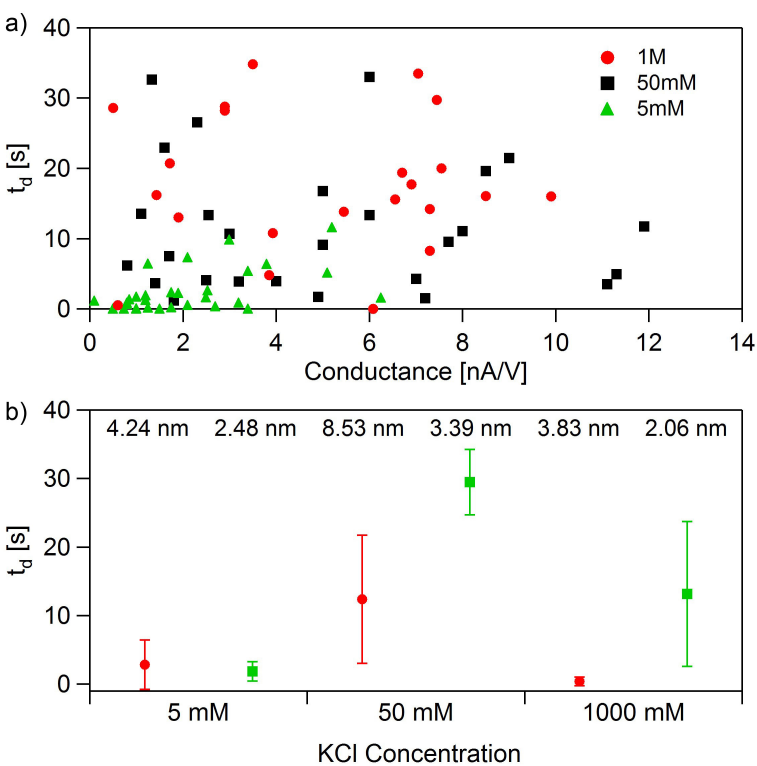


Figure 4.2.7: Delay time dependence on pore conductance and KCl concentration. We examined the effect of pore conductance (pore conductance is proportional to pore size) on  $t_d$  values. (a) Scatter plot of  $t_d$  vs. pore conductance, showing no clear correlation. (b) Average from 5 to 10 experiments of  $t_d$  for two pores of different sizes at each KCl concentration, showing no clear correlation. Pore size is given at the top of panel b.

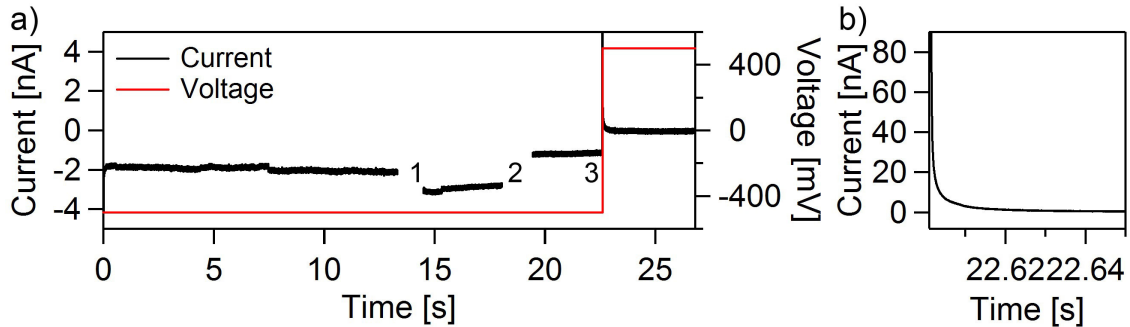


Figure 4.2.8: Current vs. time trace and corresponding voltage vs. time trace for a nanoparticle formation experiment in the presence of  $\alpha$ -lipoic acid. This experiment was performed on a 4.2 nm diameter pore in 50 mM KCl solution. (1), (2), and (3) represent the same experimental steps as in Figure 4.2.4b. (b) Zoom in of (3) demonstrating that particle formation occurs faster than the limits of detection.

which contains a disulfide group that binds to the gold surface with high affinity. It therefore caps the grown particle to prevent further aggregation of gold to the particles surface.

Figure 4.2.8a shows a time trace of nanoparticle formation in the presence of  $\alpha$ -lipoic acid. In experiments with this complex, when the polarity of the voltage is switched (Figure 4.2.8a (3)), the current shows only a capacitive curve that immediately decays to zero. That is, a particle forms very quickly (under 2 ms) and  $t_d$  cannot be measured. This is demonstrated in Figure 4.2.8b, which is the zoom in of Figure 4.2.8a, and suggests that the particle completely forms faster than the setup can resolve. I-V traces were performed before and after particle formation and verified that the particle fills the pore.

To illustrate the effects of salt concentration and additives, Figure 4.2.9 shows TEM images of particles formed at high salt concentration (1 M, a), at low salt con-

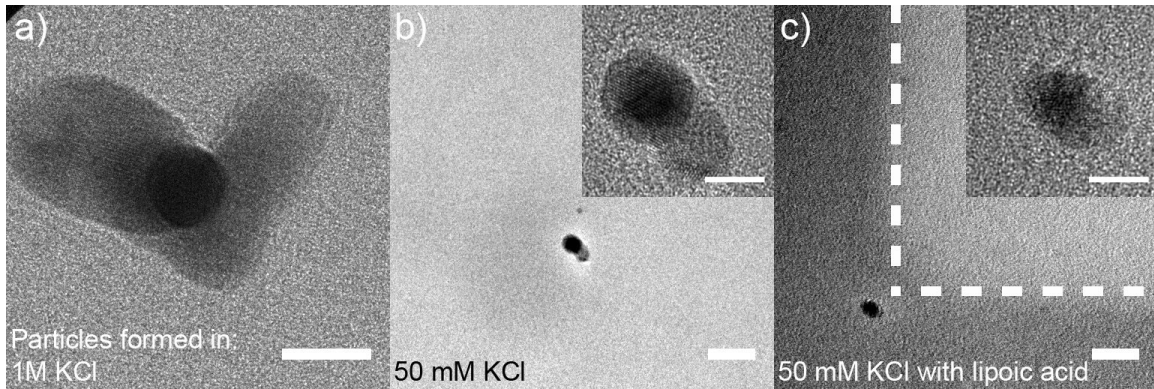


Figure 4.2.9: Transmission electron micrographs of particles synthesized in nanopores. Particles were formed using reagents in (a) 1 M KCl, (b) 50 mM KCl, and (c) 50 mM KCl with  $\alpha$ -lipoic acid. Insets are zoomed in images of the particles. Scale bar is 10 nm in panel a, 20 nm in panels b and c, and 5 nm in the insets. For low salt concentrations ( $\leq$  50 mM), the chemical reaction is tightly confined to the nanopore and gold is observed inside the pore only with no additional Au present in the vicinity, as seen in the larger views of the particle and surrounding SiN<sub>x</sub> surface of panels b and c.

centration (50 mM, b), and at low salt concentration (50 mM) with  $\alpha$ -lipoic acid (c).

At low salt concentrations with or without  $\alpha$ -lipoic acid, the nanoparticle is tightly confined in the nanopore area and there are no additional aggregates formed. See Figure 4.2.10 for examples of high salt aggregates. High resolution TEM imaging shows that the particles are crystalline (Figure 4.2.11). From Fourier analysis of intensity linescans in the boxed areas in Figure 4.2.11c the lattice spacing was determined to be  $0.25 \pm 0.05$  nm as shown in Figure 4.2.11d, where the error is in the TEMs magnification, close to the published value of the 200 lattice spacing of 0.204 nm, as determined by X-ray crystallography.<sup>145</sup>

Nanoparticles formed using low salt concentrations and the  $\alpha$ -lipoic acid gold chloride complex were restricted to the nanopore volume, and showed no signs of

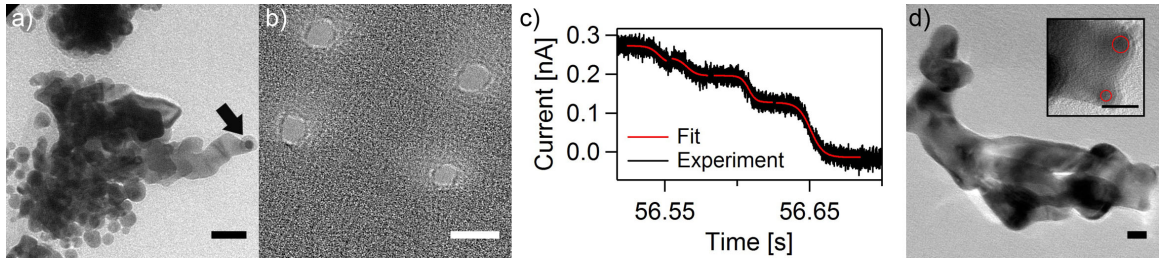


Figure 4.2.10: (a) Transmission electron micrograph of gold formed in 1M KCl. The relatively long delay time,  $t_d$ , before the pore closes allows additional reagent to traverse the pore and react, resulting in aggregate gold around the nanopore (indicated by the arrow). Scale bar is 20 nm. (b)-(d) Particle formation events in an experiment with multiple nanopores on a single chip. Experiment was done on an array of four nanopores shown in the TEM in (b) in 50 mM KCl solution without  $\alpha$ -lipoic acid. (b) Ion current trace shows stepwise reduction in the current and corresponding fits of four distinguishable formation curves. Voltage polarity was switched at  $t = 13$  s. (c) TEM after particle formation. In addition to Au formation in the pores (darker regions in the TEM image), we observe that Au forms outside of pores as well. Inset is a higher magnification image of the pores, with their locations circled in red. All scale bars are 10 nm. Note that in the absence of  $\alpha$ -lipoic acid additional gold formed outside the pore region. The formation of the four particles is suspected to be correlated. This is supported by the gold connecting the four pores, as well as the  $t_d$  of the four events having much less variation than observed in Figure 4.2.6. Future studies could include device designs where nanopores are individually controlled by electric fields.

additional particle formation over the entire silicon nitride membrane (Figure 4.2.9c).

Based on TEM imaging, particles appear to conform to the shape of the pore (see Figure 4.2.12 for TEM images of a pore before and after particle formation). Further studies involving electron tomography could investigate the effect of pore shape<sup>66</sup> on the shape of the resulting particles. Synthesized particles were also found to remain fixed inside of the pores. Even 18 days after formation, particles were observed fixed inside their pores in the TEM.

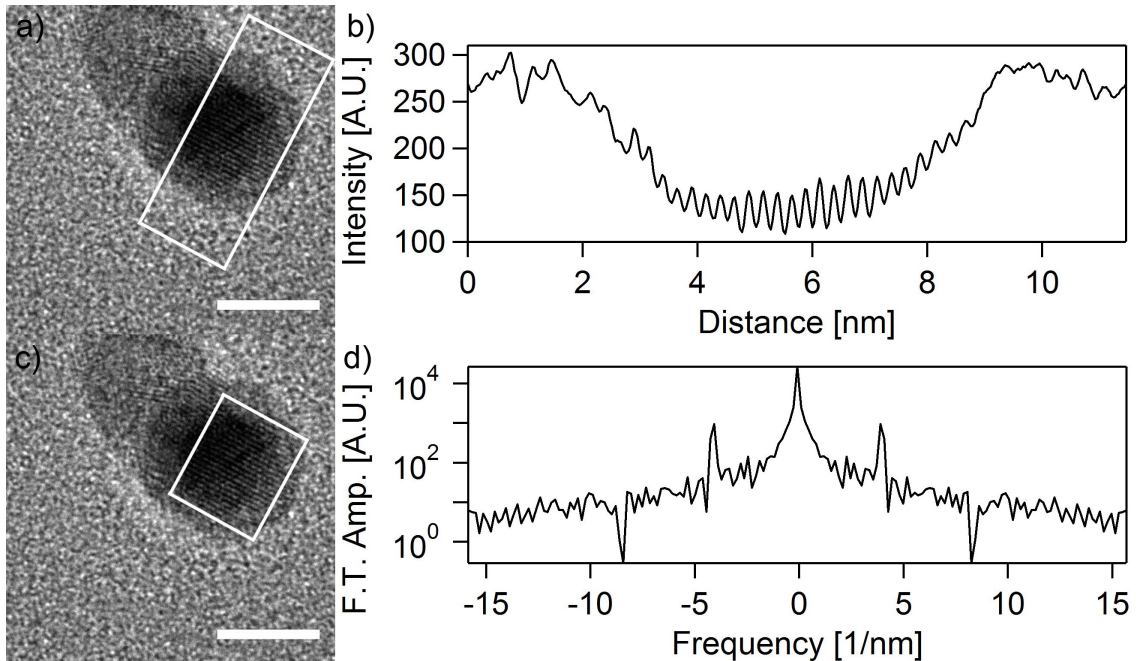


Figure 4.2.11: Determination of lattice spacing. (a) TEM image of gold nanoparticle. Area inside white box is used to create (b) profile. Particle is crystalline and shows lattice planes within the crystal whereas the SiN<sub>x</sub> membrane surrounding the particle does not show lattice planes. The intensity profile data averaged over the depth of the white box in (c) is Fourier transformed to create (d). Peak value in panel d is at 3.95 nm<sup>-1</sup>. Scale bar is 5 nm in panels a and c.

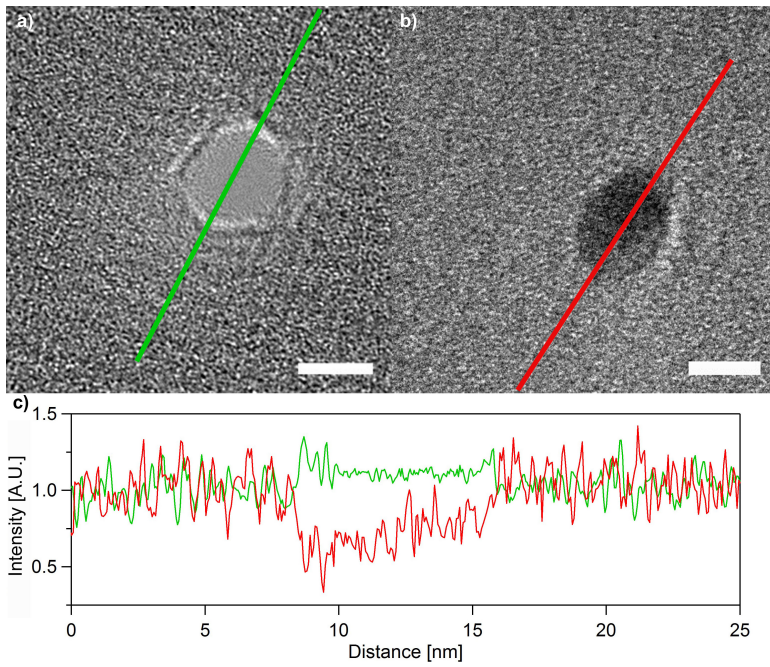


Figure 4.2.12: TEM of a pore (a) before and (b) after particle formation. (c) Profile of the intensity of the TEM images taken along red and green lines as marked. Particle was formed in 50 mM KCl with  $\alpha$ -lipoic acid.

#### **4.2.7 Summary**

To summarize, an original synthesis of nanoparticles was demonstrated with controllable size formed at a pre-determined position in a thin solid-state membrane using electric field-driven electrolyte flow. Particle formation is electrically triggered and actively monitored by current readout, and the particle growth in time is quantitatively described by the Richards curve. Particle size and position is largely determined by the properties of a corresponding nanopore drilled at a desired position on a chip. Lowering salt concentration in solution and adding a capping agent improves particle confinement within the nanopore. Nanoparticles form orders of magnitude faster with this method than has been previously reported and their formation can be monitored at timescales down to tens of microseconds. Future expansions of this work can focus on creating unique nanoparticle arrays with nanopores that are independently addressed by electric fields and expanding this method to other metals and materials. Finally, because each synthesized particle can be easily located, high resolution TEM studies of the structure and shape of individual nanoparticles as a function of synthesis conditions are now possible.

## 4.3 Nanoparticle Translocations

### 4.3.1 Introduction

Although the primary application of nanopore sensors has been towards next-generation DNA sequencing,<sup>59</sup> nanopores have previously been used for studies involving nanoparticles. As discussed in the preceding section, nanopores have found use to create and trap nanoparticles.<sup>136</sup> Nanopores have also been used to form nanoelectrodes,<sup>71</sup> study single-walled nanotubes attached to ssDNA,<sup>42</sup> detect<sup>13,38</sup> and separate<sup>107</sup> spherical gold nanoparticles, create nanoparticles<sup>136</sup> and nanorods,<sup>116</sup> and study colloids.<sup>5</sup> Carbon nanotube Coulter counters have previously been suggested as a method of characterizing spherical nanoparticle surface charge,<sup>56,57</sup> microfluidics have been used to measure spherical nanoparticle size distributions,<sup>36</sup> and larger pores have been used to measure the zeta potential of polystyrene beads.<sup>70</sup> Additionally, the translocation properties of stiff, rod-shaped viruses has been recently studied.<sup>90</sup>

In this section, we demonstrate the use of nanopores for detection of charged nanorods (NR) and develop a method to measure their surface charge. The measurement of the charge of anisotropic nanoparticles is particularly challenging. Typically, the nanoparticle charge is measured using electrophoretic light scattering (ELS) measurements. While the charge of spherical particles can be measured accurately, these measurements are inaccurate for non-spherical particles with  $\kappa a > 1$ , where  $\kappa$  is the inverse Debye length, and  $a$  is the particle size. We study translocations of gold

nanoparticles and nanorods through silicon nitride nanopores and present a method for determining the surface charge of nanorods from the magnitude of the ionic current change as nanorods pass through the pore. Positively-charged nanorods and spherical nanoparticles with average diameters 10 nm and average nanorod lengths between 44 and 65 nm were translocated through 40 nm thick nanopores with diameters between 19 and 27 nm in 1, 10, or 100 mM KCl solutions. Nanorod passage through the nanopores decreases ion current in larger diameter pores, as in the case of typical Coulter counters, but it increases ion current in smaller diameter nanopores, likely because of the interaction of the nanopore's and nanoparticle's double layers. The presented method predicts a surface charge of  $26 \text{ mC/m}^2$  for 44 nm long gold nanorods and  $18 \text{ mC/m}^2$  for 65 nm long gold nanorods and facilitates future studies of ligand coverage and surface charge effects in anisotropic particles.

#### 4.3.2 Experimental Methods

In a traditional ELS measurement, particles are suspended in solution and a potential is applied across the solution. By measuring the Doppler shift of a reference laser passing through the suspension of particles as they are pulled through the solution, the particle mobility is extracted. This mobility can be used in combination with one of two approximations to calculate the surface potential. For the case where  $\kappa a > 1$ , where  $\kappa$  is the inverse Debye length and  $a$  is the particle size, the Hückel approximation is used.<sup>102</sup> The derivation of the Hückel approximation requires the formula

for Stokes drag,<sup>102</sup> which is essentially derived from an approximate analytical solution that exists only for spherical particles.<sup>6</sup> These approximate solutions, however, are not valid for nanorods. Once the surface potential is obtained, the Grahame equation<sup>102</sup> can be used to find the surface charge density:

$$\sigma = \frac{2\epsilon_r\epsilon_0 kT}{ze\lambda_d} \sinh\left(\frac{ze\psi_0}{2kT}\right) \quad (4.4)$$

Where  $\sigma$  is the surface charge density,  $\epsilon_r$  is the relative permittivity of water,  $\epsilon_0$  is the vacuum permittivity,  $k$  is the Boltzmann constant,  $T$  is temperature,  $e$  is the elementary charge,  $z$  is the electrolyte valence,  $\lambda_d$  is the Debye length of solution, and  $\psi_0$  is the surface potential.

Using nanopores we overcome this challenge. We present a method to characterize anisotropic particle charge. Our method proceeds in two steps. First, we measure the translocation of nanorods through a nanopore of known dimensions. We then use the information about the ionic current change to simulate the nanorods' translocation assuming a given surface charge. By iteratively altering the assumed surface charge until the simulations match the experimental results, we determine the nanorod surface charge. We first validate our model by translocating spherical gold nanoparticles of known charge, measured with ELS.

We demonstrate this technique on  $\sim 10$  nm diameter gold NRs using silicon nitride nanopores. The data are gathered in bulk quantities (most data sets in this section contain over 500 events), but with information recorded on individual nanorods one

at a time.

A schematic of the nanopore experimental design is shown in Figure 4.3.1. As the nanorods pass through the nanopore, or translocate, their presence alters the current density inside the nanopore, and a current change is noted in the electrical readout (Figure 4.3.2). If the presence of the nanorods decreases the current density through the nanopore, a decrease is observed in the electrical readout, and if it increases the current density, an increase is observed. We show from these events the charge on arbitrarily shaped nanoparticles can be determined.

40 nm thick silicon nitride membranes approximately  $25 \mu\text{m} \times 25 \mu\text{m}$  in size were used in this experiment. A schematic cross-section of the completed membrane design is shown in Figure 4.3.1a. The nanopores presented here have diameters in the range of 19 nm to 27 nm to accommodate the NRs used. Figure 4.3.1b shows a TEM image of one such nanopore with a diameter of 23 nm. To account for the fact that nanopores are not perfectly circular and more accurately described by ellipses, nanopore area was measured from TEM images of the nanopore, and the nanopore diameter was calculated from a circle of equivalent area. We estimate the error in our nanopore diameter to be 0.5 nm due to measurement error. These experiments used the PTFE measurement cell, shown in Figure 4.3.1c. Salt solution composed of 1 mM, 10 mM, or 100 mM KCl with EDTA at 1/1000 the KCl concentration buffered to pH 8 using Tris-HCl at 1/100 the KCl concentration is injected into the cell and channel. This low salt concentration is used to prevent NR aggregation, and NR aggregation was

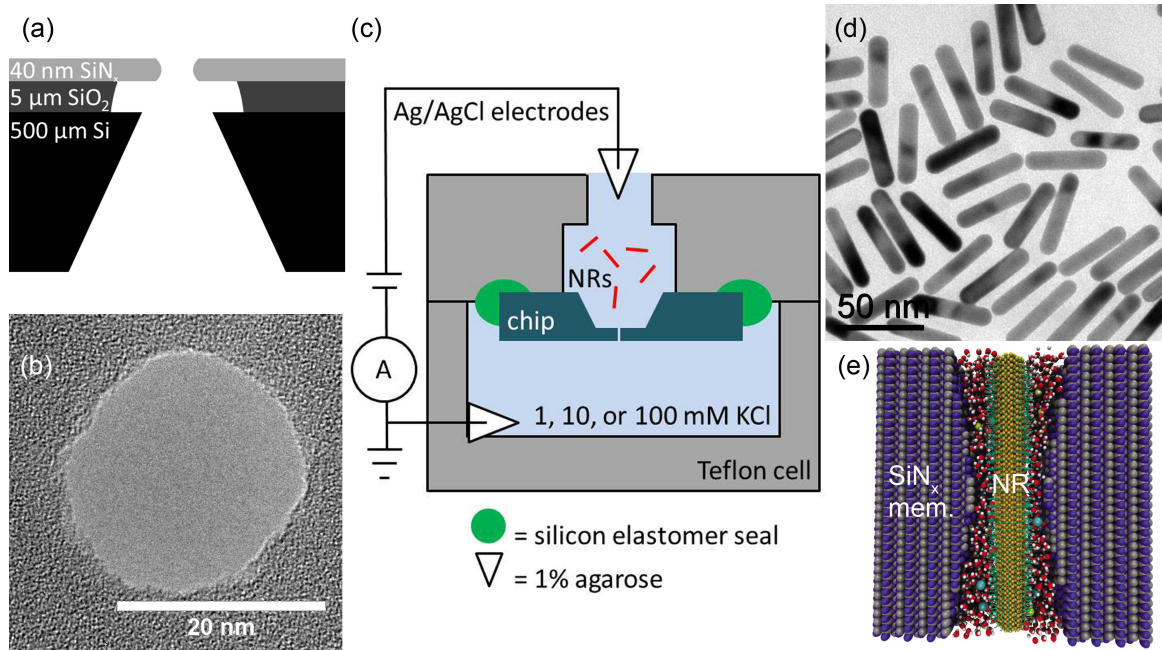


Figure 4.3.1: (a) Nanopore structure (not to scale). The nanopore is created in a 40 nm thick silicon nitride membrane, as demonstrated in the TEM image. The silicon nitride membrane is supported by 5  $\mu$ m of silicon dioxide for noise reduction, on a 500  $\mu$ m silicon wafer. (b) TEM image of a nanopore. The nanopore shown is 23 nm in diameter. (c) Experimental design. The nanopore is placed to divide two chambers of KCl solution. A voltage bias is applied between the chambers, and nanorods are introduced to the chamber at higher bias. The nanorods are drawn through the nanopore by the potential bias. (d) Nanorod characterization. Nanorod samples ranged in length between 44 and 65 nm. The nanorods pictured are 10 nm in diameter and 44 nm long. (e) Nanorod-nanopore system rendered using a molecular dynamics model of a nanorod capped with cetyltrimethylammonium bromide molecules inside a silicon nitride nanopore illustrated with a 20 nm diameter nanopore and 11 nm diameter nanorod. The silicon nitride pore is presented in purple and grey. In the center, the gold nanorod and the ligands are shown in yellow (NR) and green (ligands). In between the nanorod and the walls of the pore, water molecules and KCl ions are shown as red/white and green/yellow spheres, respectively.

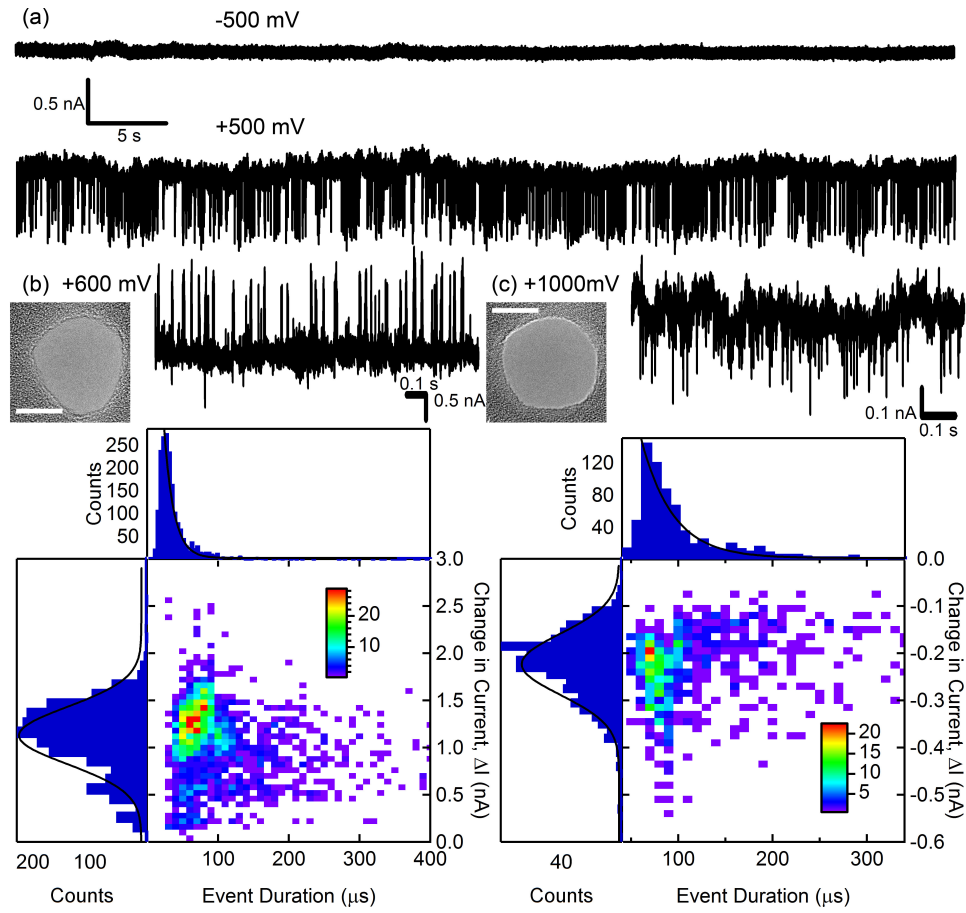


Figure 4.3.2: (a) A segment of a current trace for a nanorod experiment. This experiment used a 24 nm diameter nanopore with 65 nm long nanorods that were 10 nm in diameter. The data were taken in 10 mM KCl solution. Before nanorods are added, or when the voltage polarity is switched, no translocation events are seen, demonstrated in the top trace. After nanorods are added, spikes are seen in the current versus time trace (bottom trace). These are translocation events. This experiment was taken on the Axopatch 200B. (b) and (c) are the results from additional nanorod translocation experiments (b) This experiment was performed with 100 mM KCl, a 19.3 nm diameter nanopore, and 45 nm long, 9 nm diameter nanorods. Although occasional downward spikes can be seen in the current vs time trace, these events are rare and are attributed to noise in the system. (c) This experiment was performed with 1 mM KCl, a 20.4 nm diameter nanopore, and 45 nm long, 9 nm diameter nanorods. For (b) and (c), a segment of the raw current vs time trace is shown at the top alongside a TEM image of the nanopore used in the experiment. The scale bars in the TEM images are 10 nm. Below is plotted a 2D histogram of the change in current ( $\Delta I$ ) during an event versus the duration of the event. Along the sides are the corresponding 1D histograms.  $\Delta I$  is fit to a gaussian function, and event duration is fit to an exponential function to determine the quoted values of  $\Delta I$  and event duration. All experiments were performed at the applied bias noted in the figure.

checked using absorbance spectroscopy (see Figure 4.3.4). Bias potentials between 500 mV and 2000 mV are applied across the nanopore using Ag/AgCl electrodes separated from the solution by a 1% agarose gel, and ionic current is monitored as a function of time. Agarose gel is used to prevent any interaction of the nanorods or nanorod coating with the electrodes.

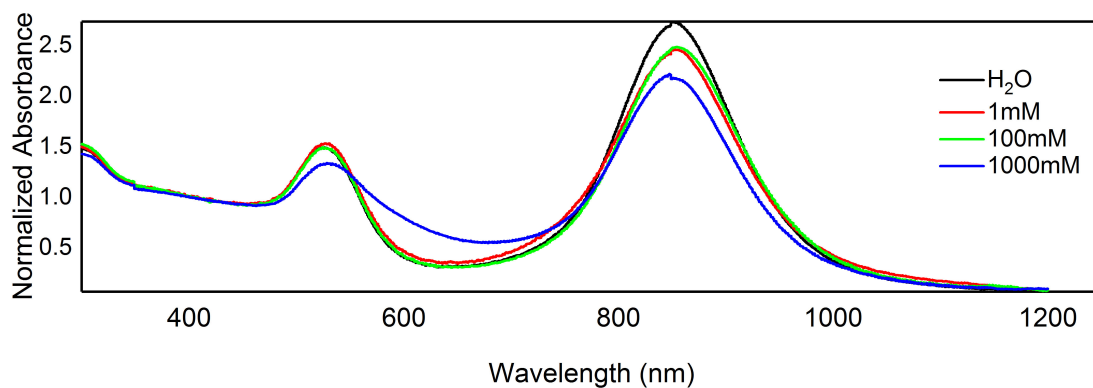


Figure 4.3.3: Absorbance of 9 nm diameter, 45 nm long nanorods (sample B) normalized to the absorbance at 400 nm wavelength, and measured at varying salt concentrations. There is no noticeable broadening or red-shifting of the nanorod absorbance peaks at 100 mM KCl solution, indicating that minimal aggregation occurs.

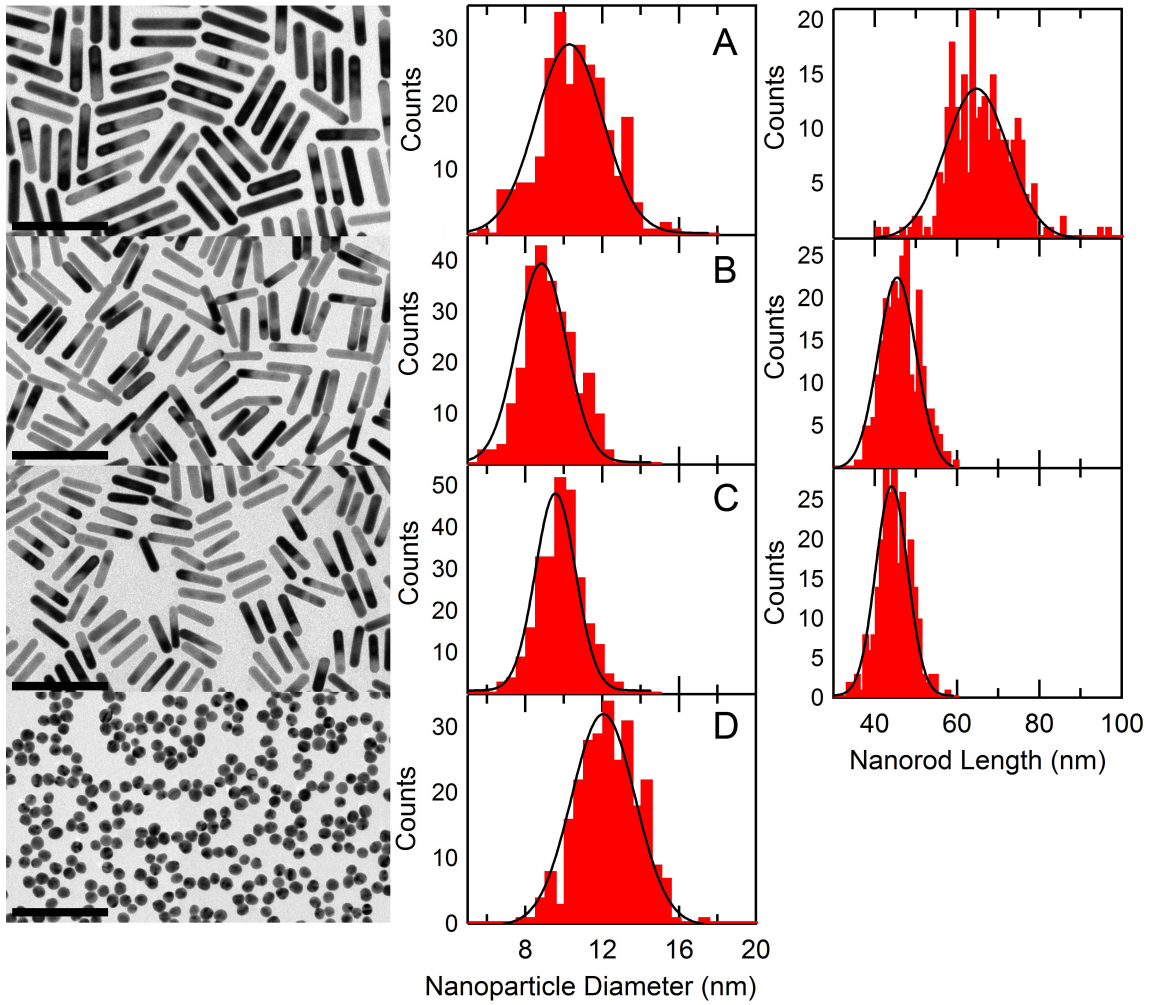


Figure 4.3.4: Analysis of nanoparticle dimensions. Nanorod and nanoparticle dimensions were measured from TEM images. Scale bar is 100 nm. At least 250 data points were acquired to create each histogram. The first column shows an example of a TEM image for each sample, the second column shows histograms of the diameters for each sample, and the third column shows histograms of the lengths for each sample. The first row is data for sample A, the second row is data for sample B, the third row is data for sample C, and the last row is data for the spherical sample D.

Gold NR synthesis has been recently described elsewhere.<sup>148</sup> All NR samples used here are  $10 \pm 3$  nm in diameter. The three NR samples used are either  $65 \pm 11$  nm in length and  $10 \pm 2$  nm in diameter,  $45 \pm 7$  nm in length and  $9 \pm 2$  nm in diameter,  $44 \pm 6$  nm in length and  $10 \pm 2$  nm in diameter, or spherical particles  $12 \pm 2$  nm in diameter, as determined by analyzing a large number of particles from TEM images (see Figure 4.3.3). A TEM image of a typical nanorod sample is shown in Figure 4.3.1d. NRs are colloidally stabilized with double layers of cetyltrimethylammonium bromide (CTAB), which gives the NRs a positive charge in solution and adds an additional 2 nm to all surfaces of the NR, making the gold nanorod-ligand system  $\sim 14$  nm in effective diameter, as simulated below and illustrated in Figure 4.3.1e. The absorbance spectrum for nanorods in a range of KCl concentrations was checked, and for the salt concentrations presented here (100 mM KCl or less), the absorbance peaks were not found to broaden or red-shift, indicating the nanorods have negligible agglomeration at these salt concentrations (see Figure 4.3.4).

Surface charge density values were extracted from zeta potential measurements. For nanorods, this value is an estimation due to violating the spherical particle assumption. The values extracted from these results were  $10 \text{ mC/m}^2$  for the 65 nm long nanorods and  $9 \text{ mC/m}^2$  for the 44 nm long nanorods. For spherical nanoparticles, this value represents a more accurate measurement of surface charge density. For the spherical nanoparticles used here, a value of  $14 \text{ mC/m}^2$  was obtained.

Either a VC100 low-noise patch-clamp amplifier (Chimera Instruments) or an

Axopatch 200B (Molecular Devices) was used to measure the current through the nanopore and apply a bias voltage. When the Chimera was used, data were sampled at 6 MHz bandwidth, and a fourth order low-pass Bessel filter was applied at 1 MHz. All data were digitally filtered with a low-pass cutoff of 10 kHz and a sampling rate of either 50 or 100 kS/s. Custom Python software defines events as a percent change in the current relative to the standard deviation of the moving average open pore conductance. For analysis purposes, we consider an event to end when the conductance value returns to within one standard deviation of its previous open pore conductance value. All current versus time trace displayed in this section are displayed with the filtering settings with which they were analyzed.

### 4.3.3 Crossover between Increasing and Decreasing Events

Figure 4.3.2 shows one data set acquired during this experiment. Figure 4.3.2a shows segments of the current versus time trace acquired during the experiment. Voltage is applied to the top electrode (Figure 4.3.1c) and measured at the bottom electrode, held at virtual ground. Before nanorods are added to the voltage-applying chamber, or when a negative voltage applied to the top electrode prevents the positively charged nanorod used here from translocating, no translocation events are seen (Figure 4.3.2, top). When nanorods are added to the voltage-applying chamber and the correct positive voltage polarity is applied to the top electrode, nanorod translocations appear as spikes in the current versus time trace (Figure 4.3.2, bottom). By

plotting the change in conductance during an event ( $\Delta G$ ) versus the event duration, the distribution of event shapes becomes clear. Figures 4.3.2b and c show two more experiments using the nanopores pictured with a segment of the current versus time trace and their histogram distributions of event duration and  $\Delta G$ .

We found that the percent change in the conductance,  $\Delta G/G_0 = (G_0 - G_{event}) \times 100\% / G_0$ , where  $G_0$  is the nanopore conductance without a nanoparticle present and  $G_{event}$  is the nanopore conductance during nanoparticle translocation, decreases with increasing pore diameter (see Figure 4.3.5a), so that events increase the conductance in small diameter nanopores (trace in Figure 4.3.5b) and decrease the conductance in large diameter nanopores (trace in Figure 4.3.5c). Figure 4.3.5a shows  $\Delta G/G_0$  vs nanopore diameter for experiments using 100 mM KCl in a range of nanopore diameters. If we use only a geometrical argument to understand the dependence on  $\Delta G/G_0$ , where the nanopore functions as a resistor and a translocating nanoparticle effectively reduces the resistor cross-sectional area ( $A$ ),  $G = \sigma A/l$ , where  $\sigma$  is the solution conductivity and  $l$  is the nanopore membrane thickness, then  $\Delta G/G_0$  should never be greater than 0 (shown as a dashed black line in Figure 4.3.5a) because a resistor with a smaller cross-sectional area should always have a lower conductivity. Further, from this model,  $\Delta G/G_0$  should asymptotically approach zero as the pore diameter grows because the nanorod cross-sectional area accounts for a smaller fraction of the nanopore cross-sectional area as the nanopore diameter grows. This geometric model is plotted as a dashed blue line in Figure 4.3.5a. Instead, we observe

that  $\Delta G/G_0$  crosses over from positive to negative values as the nanopore diameter increases, corresponding to a transition from events that increase to events that decrease the current.

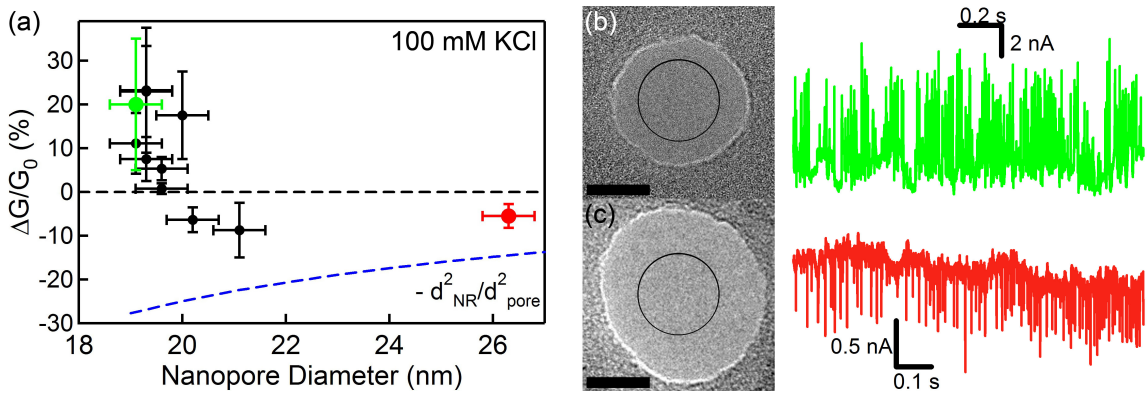


Figure 4.3.5: (a) Plot of the event percent change in the conductance during an event versus the nanopore diameter. Each marker represents a different current vs time trace collected. The nanoparticle lengths used in each experiment vary, but no trend was observed between nanoparticle length and  $\Delta G/G_0$  or nanopore diameter. The nanopore thickness (40 nm) and salt concentration (100 mM KCl) were held constant in all experiments shown. We found that the percent change in the conductance decreases as the nanopore diameter increases.  $\Delta G/G_0$  error bars correspond to the standard deviation of histograms of the relative change of conductance during nanorod translocations.  $\Delta G/G_0 = 0$  is marked with a dashed black line, and the theoretical curve based on geometric arguments ( $-d_{NR}^2/d_{pore}^2$ ) is shown as a dashed blue line, where  $d_{NR} = 10$  nm is the nanorod diameter, and  $d_{pore}$  is the nanopore diameter. The data point shown in green corresponds to (b) the top nanopore and green current vs time trace. These data were taken with the 44 nm long nanorod sample at 1 V applied bias. Although the baseline fluctuates somewhat, all data sets including (b) were analyzed with a moving baseline, and events were defined as 5 standard deviations of the noise below the baseline. The data point shown in red in (a) corresponds to (c) the bottom nanopore and red current vs time trace. This data was taken with the spherical nanoparticle sample at 1V applied bias. The scale bars in the TEM images are 10 nm, and the black outline in the TEM images is a guide to the eye of the nanorod cross-section, including the CTAB coating.

The regime of increased ionic current in smaller diameter nanopores during NR translocations is likely due to interaction between the Debye layers of the nanopore and nanorod. Our nanopores have been measured to have a negative surface charge similar to published values<sup>124</sup> due to hydroxyl groups that attach to the silicon during piranha treatment (See Figure 4.3.6 for a measurement of pore surface charge), and the nanorods have a positive surface charge due to the dissociation of the Br<sup>-</sup> ion from the CTAB coating. For small pores, the Debye layers of the nanorod and the nanopore overlap thereby increasing the net ion concentration inside the pore. If the increase in the total number of ions near the nanopore walls is greater than the number of ions that were blocked by the nanoparticle, a positive change in conductance is observed. Ionic mobility also plays a roll in the final nanopore conductance. Throughout a single experiment, we observe that either every event increases the conductance or every event decreases the conductance, but we never observe both increasing and decreasing events in the same experiment. Additionally, the same nanorod sample has shown events with increasing current in larger pores and events with decreasing current in smaller pores. This suggests that it is the nanopore diameter (relative to the constant nanorod diameter) and not the nanorod sample that is responsible for this phenomenon. Geometrically, in 100 mM KCl solution ( $\lambda_d \approx 1 \text{ nm}$ ), the electrical double layers should begin to overlap when the nanopore is  $\leq 19 \text{ nm}$ , and from Figure 4.3.5a, we see that the crossover between increasing and decreasing events occurs around 20 nm. A similar effect has been observed previously in DNA translocation

experiments by altering the salt concentration<sup>121</sup> or the pH,<sup>32</sup> and both modifications will alter the size of the electrical double layers. Events that enhance conduction in silicon nitride nanopores were observed for negatively charged gold nanoparticles<sup>38</sup> under similar conditions of low salt concentration and the ratio of nanoparticle to nanopore diameter of  $\sim 0.5 - 0.8$ , attributed to the interplay of surface charge values, salt concentration, and the ratio of nanopore to nanoparticle diameter. Event duration was also analyzed. As expected, longer NRs had longer translocation times (see Figure 4.3.7).

#### 4.3.4 Simulating Nanorod Translocations to Extract Charge

Sample simulation results for spherical nanoparticles and nanorods are shown in Figures 4.3.8a and 4.3.8b. First, to validate our method for measuring anisotropic nanoparticle surface charge, we tested the method with spherical nanoparticles. For the translocation of spherical nanoparticles through nanopores, the nanoparticle surface charge density and all other required input parameters are known. Here we focus only on systems with larger diameter pores that can be modeled as resistors and in which the nanoparticle passage causes a decrease in ionic current. We used a finite element model to calculate the electric current inside the pore. Atomistic level models have been previously used to study the solid-state nanopores<sup>3</sup> as well as different properties of nanoparticles capped with organic ligands.<sup>61,73,108,150,151</sup> Due to the computational limitations, these models prove to be useful for small sized systems

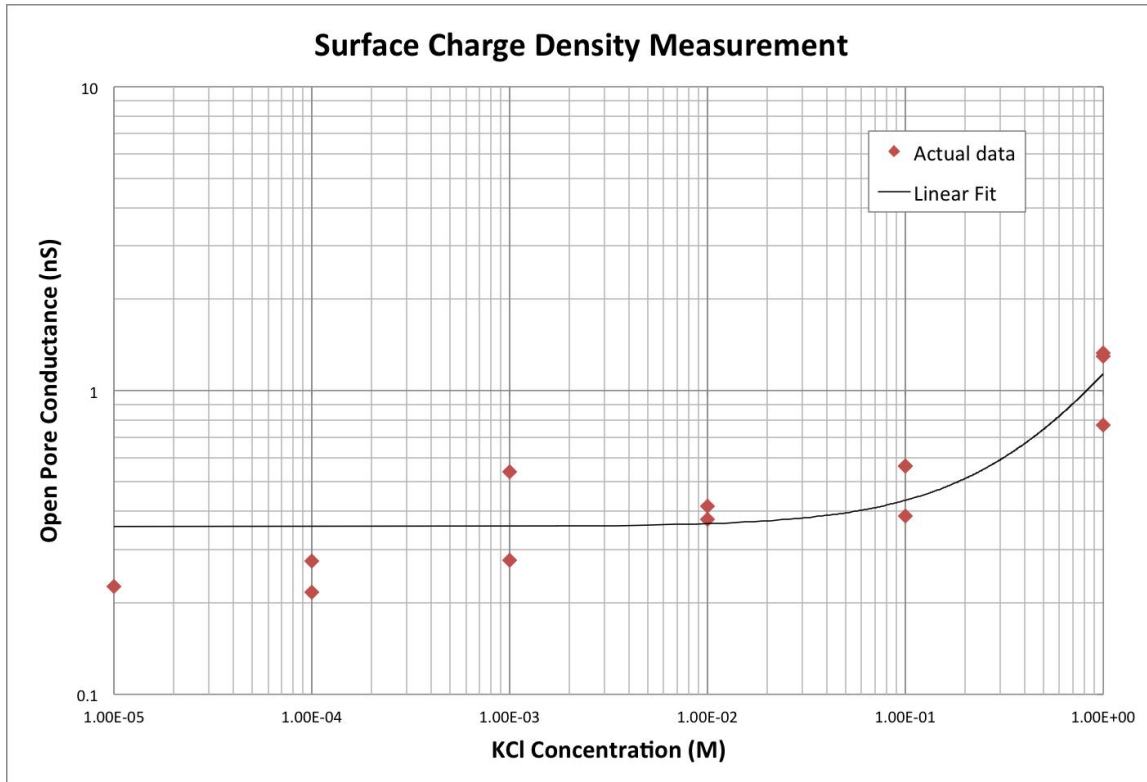


Figure 4.3.6: Measurement of nanopore surface charge. The conductance of a 5 nm diameter and 85 nm thick piranha cleaned  $\text{SiN}_x$  nanopore was measured in salt solution concentrations ranging from 1 to  $10^{-5}$  molar. The graph of nanopore conductance versus salt concentration was fit to the equation  $C = 0.780M + 0.357$ , where  $M$  is the molarity, to extract the nanopore surface charge value of  $-23.6 \pm 2.2 \text{ mC/m}^2$ .

with pores and nanoparticles of diameters below 5 nm. For larger systems, similar to the ones we study here, the kinetics of particle translocation through nanopores can be studied using continuum models. In the numerical simulations we used the finite element method to solve the coupled Navier-Stokes, Maxwell, and the Drift-Diffusion equations using COMSOL Multiphysics. For spherical nanoparticles we used an average diameter of 11 nm for the particle and 21 nm for the pore. For 100 mM KCl, we use values of  $\mu_{K^+} = 6.10 \times 10^{-8} \text{ m}^2/\text{V s}$  and  $\mu_{Cl^-} = 6.36 \times 10^{-8} \text{ m}^2/\text{V s}$  for the

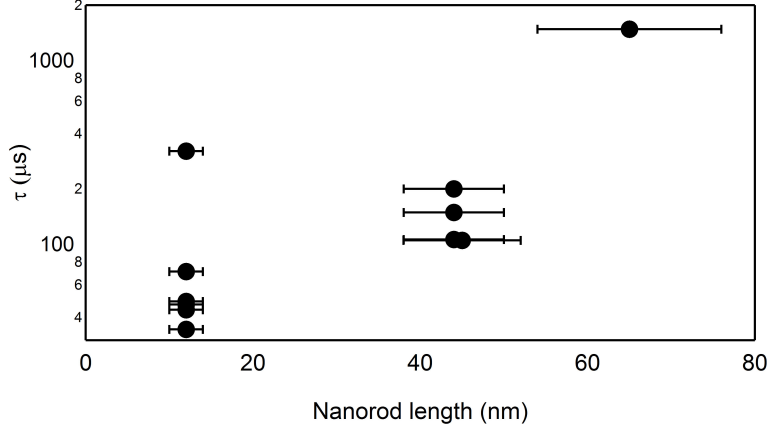


Figure 4.3.7: Analysis of event duration as a function of nanorod length, where a nanorod length of 12 nm represents a spherical nanoparticle. Y-axis error bars are smaller than the markers. Event duration is defined as the time constant,  $\tau$ , extracted from a fit of the histogram of event duration to  $e^{-t/\tau}$ . Longer nanorods are expected to have longer event durations, because their length affords them more time inside the nanopore. This matches the trend seen previously in DNA translocations.<sup>127</sup> All data sets plotted here were measured in 100 mM KCl solution.

mobilities of of electrolyte<sup>137</sup> and a value of  $\sigma = -23\text{mC/m}^2$  for the nanopore surface charge density (see Figure 4.3.6). For nanorods, we consider a pore diameter of 19 nm, an average diameter of 11 nm for nanorods with rod length of 44 nm with voltage 1 V and another rod of length 65 nm with voltage 0.5 V.

In Figure 4.3.8a, we have shown the electric potential profile obtained inside the pore in the presence of a spherical nanoparticle of diameter 11 nm. As shown in Figure 4.3.8c, at 2000 mV, for a 21 nm pore with 100 mM KCl and a translocating 11 nm spherical nanoparticle, the finite element model predicts a value of  $\Delta I = 1.0$  nA where the experimental results reveal an value of  $\Delta I = 0.7 \pm 0.5$  nA. Therefore, the simulation result lies in between the experimental measurement limits and we observe a good agreement between the simulation and the experiment.

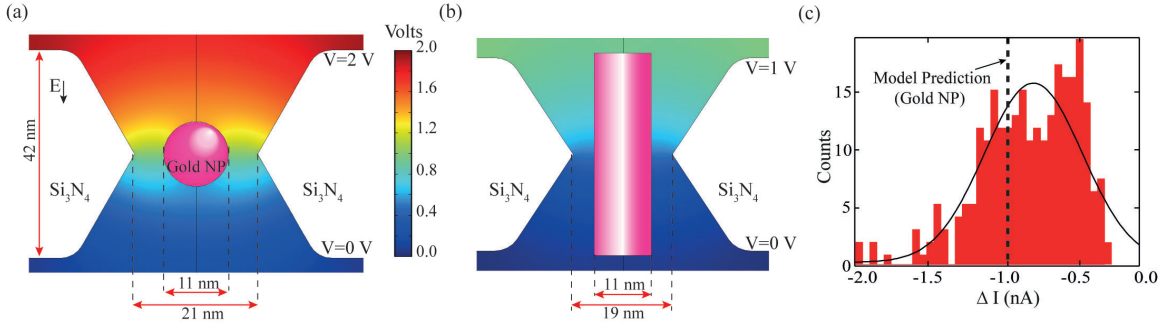


Figure 4.3.8: (a) Electric potential profile inside a nanopore during spherical nanoparticle translocation with voltage bias of 2 V, corresponding to ionic current changes shown in (c). The electric field vector points downwards in this picture. (b) Electric potential for nanorod translocation with voltage bias of 1 V, corresponding to ionic current data in Figures 4.3.5 b and c. (c) Change of ionic current,  $\Delta I$ , during spherical nanoparticle translocation from experiments and simulation. The histogram of the current change is shown with the vertical dashed line representing the simulation result.

For nanorods, we can use the finite element model to estimate the nanorod surface charge density  $\sigma_{rod}$  based on the experimental result for the current change ( $\Delta I$ ) during nanorod translocation. Since the only unknown parameter is the nanorod surface charge density, choosing a specific value for  $\sigma_{rod}$  will result in a corresponding  $\Delta I$  obtained from the model. Therefore, through trial and error, i.e. by choosing different values for  $\sigma_{rod}$  as an input parameter and calculating the corresponding  $\Delta I$  from the finite element model, a surface charge density that results in a  $\Delta I$  matching with experimental data can be found. The trial and error was started from a surface charge density value of 10 mC/m<sup>2</sup>, around that of the spherical nanoparticles, with steps of 2 mC/m<sup>2</sup> until a desirable value for  $\Delta I$  is obtained. The iteration is performed for both the upper and lower limits of  $\Delta I$  obtained from the experiments. The same procedure is repeated for translocation events of nanorods of two different lengths, 44

nm and 65 nm, inside a 19 nm pore. Based on these iterations, we obtained average values of  $26 \pm 10 \text{ mC/m}^2$  and  $18 \pm 9 \text{ mC/m}^2$  for the nanorod surface charge densities respectively. The average value of the surface charge density obtained here is larger than that of the spherical nanoparticles ( $14 \text{ mC/m}^2$ ). The surface charge density is usually proportional to the surface ligand coverage of the particles which typically scales with the surface to volume ratio.<sup>58</sup> This ratio is smaller for spherical shapes compared to cylinders, and thus we would expect lower ligand surface coverage for the spherical nanoparticles. For nanorods of different lengths but the same diameter, the surface to volume ratio is smaller for longer nanorods, consistent with surface charge densities that we obtained.

Using numerical simulations along with experimental data provides a promising method for characterizing and measuring unknown properties of nanoparticles of different shapes. The numerical method used here has also been used and validated for DNA translocation inside solid-state nanopores.<sup>137</sup> Compared to the ELS measurement, the numerical solution of the coupled Navier-Stokes and Maxwell equations in our method is more accurate than simple approximations assumed for spherical particles. At the same time, our method has the advantage that it can be generalized for particles with different shapes and geometries. Some typical limitations include the errors associated with the experimental measurements as well as the inaccuracies within the framework of continuum models, specially with regards to molecular level details for smaller nanopores, which are also common in other continuum level models

such as the ones used with ELS measurements.

#### 4.3.5 Summary

In this section, we demonstrated an original method for characterizing the surface charge on gold nanorods due to charged ligands. The method works by first measuring the current change and event duration during nanorod transit, then iteratively adjusting the surface charge value of the nanorod in simulations of translocations until the simulation matches the experiment. We first validated our method by measuring the surface charge on spherical nanoparticles and comparing it to values obtained by ELS, and found the numbers to be in good agreement. We found that in some experiments, translocation events increased the nanopore current while in others events decreased the current, for smaller and larger diameter nanopores, respectively. We surmise that this transition from positive to negative current change is due to the onset of interactions between the Debye layers of the nanoparticle and nanopore at low salt concentrations for nanopore diameters comparable to the nanoparticle size. While our model describes well the regime of  $\Delta G/G_0 < 0$  in larger diameter nanopores, future work should include more detailed simulations to quantitatively explain the observed crossover of  $\Delta G/G_0$  from positive to negative values as the nanopore diameter increases. We anticipate that future studies will make use of this new characterization method in experiments on charged nanorods.

## 4.4 Conclusions

This chapter has discussed the application of nanopore sensors to the study and characterization of gold nanoparticles. The formation of single nanoparticles was observed electronically inside a nanopore, and the event was found to fit a sigmoid Richards curve. Nanoparticle formation was found to occur stochastically, but decreasing the inert salt concentration was found to decrease the wait time before a particle formed. It is hypothesized this is due to an increased ion fraction of reagents to inert salt ions. Further, as in bulk synthesis, a capping agent was found to reduce particle agglomeration outside the nanopore volume, and to reduce the wait time before a particle formed to below detection limits.

Nanopore sensors were also used to study the charge of nanorods. To the author's knowledge, no method existed to correctly measure nanorod charge prior to these experiments. Nanorod charge was found to deviate significantly from estimates assuming a spherical shape. The crossover of translocation events that increased conductance to translocation events that decreased conductance was observed, and is explained by the interactions of electrical double layers between the nanopore and nanoparticle.

Future work into the use of nanopores to study nanoparticles could further study the crossover phenomenon, as well as quickly measure nanoparticle size distributions, create nanoparticles in templated arrays, and create nanoparticles of multiple mate-

rials.

# CHAPTER 5

## Appendix

### 5.1 Resist-based Lithographies

Both photolithography and electron beam lithography fit into the category of resist-based lithographies, as the two patterning methods have many similarities. Resist-based lithographies are used to create a pattern of exposed and covered areas on a sample in order to imprint this pattern on the sample by either adding or removing material from the exposed areas.

The most important part of resist-based lithographies is the resist. A lithography resist must be sensitive to radiation. Upon exposure, the solubility of the polymer must be altered so that either the exposed or unexposed portion of the polymer can be dissolved without damaging the other portion. For example, poly methyl methacrylate (PMMA), a common electron beam resist, develops scissions (i.e., chemical bonds are broken, resulting in a less cross-linked polymer) upon exposure to high-energy electrons, making exposed PMMA more soluble than unexposed PMMA. Solvents such as methyl isobutyl ketone (MIBK) will dissolve exposed PMMA while leaving unexposed PMMA unaltered. PMMA is an example of a positive resist; a positive resist increases in solubility upon exposure to radiation. Negative resists decrease in

solubility upon exposure to radiation.

Photolithography and electron beam lithography differ in the type of radiation that alters the resist. Photolithography employs resists that change structure under UV illumination whereas electron beam lithography employs resists that change structure when exposed to high energy electrons. Photolithography is limited in patterning resolution by the wavelength of the UV illumination used and generally cannot create patterned features smaller than a few hundred nanometers. Electron beam lithography is employed to make smaller features. The electron beam sources used in the work presented here can pattern features with dimensions as small as a few tens of nanometers.

Figure 5.1.1 shows the procedure for performing resist-based lithography. First, a resist is placed on a sample (shown in Figure 5.1.1a) and spun at high velocities to create an even thickness coating of resist (Figure 5.1.1b). The resist is then baked to remove solvent and cross link the polymer. In the case of electron beam lithography, the sample is then exposed to an electron beam, which rasters to create the desired pattern (Figure 5.1.1c). In the case of photolithography, a mask composed of opaque and transparent regions (traditionally chrome deposited on glass) is placed between the sample and a UV radiation source, and the source is turned on for a set time period (Figure 5.1.1d). The resist has now been altered in some regions. The sample is then sometimes baked again to allow the polymer some degree of relaxation and remove effects of interference patterns caused by UV reflection normal to the sample

surface. The sample is then developed in a solvent designed to remove the more soluble resist and leave the less soluble resist intact (Figure 5.1.1e). The sample can now be patterned with materials using the resist template either by removing materials using chemical etching or reactive ion etching (Figure 5.1.1g) or by building up materials using metal evaporation (Figure 5.1.1f). The resist is removed with a more powerful solvent when no longer needed, leaving only the patterned sample behind (Figure 5.1.1h).

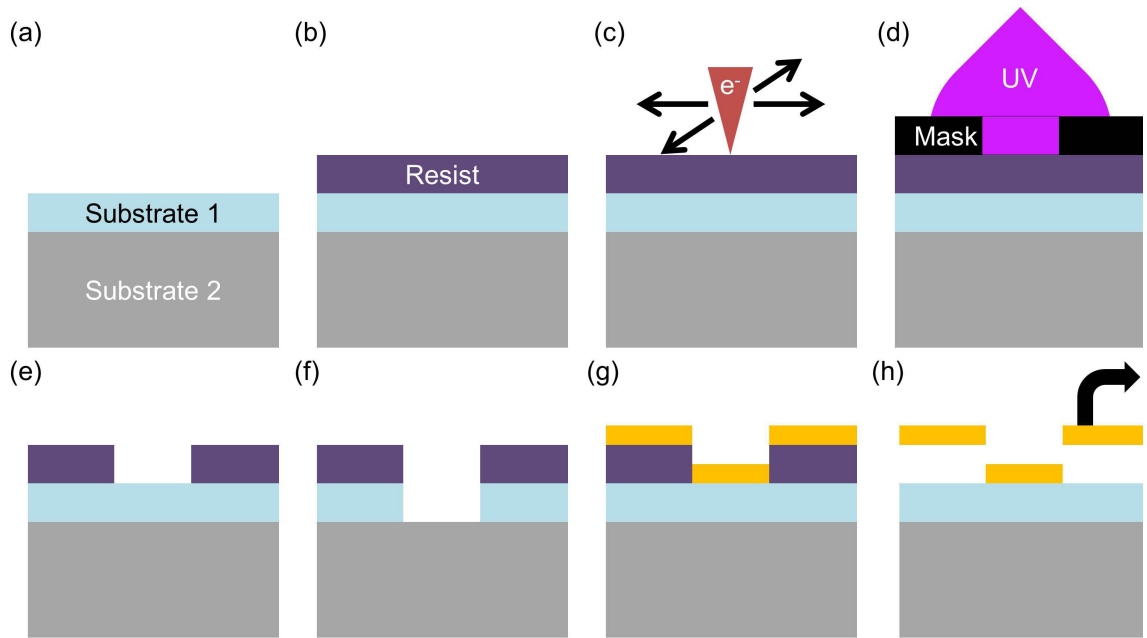


Figure 5.1.1: (a) The initial substrate before resist-based lithography. (b) resist is spun onto the substrate. (c) In electron beam lithography, a high-energy electron beam is rastered across the sample to expose patterned areas of resist. (d) In photolithography, a transparent mask with patterned regions blacked out is placed between the sample and a UV source, and the UV source is turned on, exposing the areas of resist under the transparent portions of the mask. (e) The resist is developed in a weak solvent to remove the more-soluble portions of the resist. The patterned substrate can now be etched with processes such as plasma or chemical etching (f) or material can be added to the sample with processes such as metal evaporation (g). (h) The resist is removed (and if materials were deposited, the material deposited over the resist is removed with the resist), leaving a patterned sample.

Below are the recipes used over the course of this work. AZ5412-E is a special resist that can be either positive or negative. It requires an additional flood exposure (an exposure without a photomask) to turn from a positive to a negative resist.

Photolithography		
Photoresist	NR7	AZ5214-E
Resist Type	Negative	Positive or Negative
Spin Speed	4000 rpm	4000 rpm
Pre-Bake Temperature	115°C	100°C
Pre-Bake Time	3 min	2 min
Photolithography System Used	Karl Suss MA4	Karl Suss MA4
Wavelength Used	365 nm	365 nm
UV Dose	170 mJ	20 mJ
Post-Bake Temperature	115°C	120°C
Post-Bake Time	3 min	2 min
Flood Exposure Dose	none	120 mJ
Developer Used	RD6	AZ726
Development Time	7 s	30 s

Electron Beam Lithography		
Electron Beam Resist	C2 950 PMMA	C2 950 PMMA
Spin Speed	4000 rpm	4000 rpm
Pre-Bake Temperature	180°C	180°C
Pre-Bake Time	10 min	10 min
System Used	Elionix ELS-7500EX	JEOL JSM 6400
Beam Spot Diameter	187.5 nm	54 nm
Beam Current	20 pA	10 pA
Dose	853 μAs/cm <sup>3</sup>	750 μAs/cm <sup>3</sup>
Developer Used	3:1 Isopropanol:MIBK	3:1 Isopropanol:MIBK
Development Time	60 s	60 s

Table 5.1: Photolithography and electron beam lithography recipes

## 5.2 Plasma and Reaction Ion Etching

Plasma and Reactive Ion Etching (RIE) both remove material from a sample using a reactive ionized gas in a high voltage chamber. Figure 5.2.1 shows a schematic of a plasma etching system. Two plates create a high bias in a chamber with a sample located on one plate, and gas is flowed through the chamber. The bias is large enough to ionize the gas molecules, which move towards the plate. In the example shown,  $\text{CF}_4 \longrightarrow \text{CF}_3^+ + \text{F}^-$ . When free radicals from this ionization reaction reach the sample, they react with the sample material to form new gaseous compounds. These compounds then desorb from the surface and are carried out of the chamber. In this example, the  $\text{F}^-$  reacts with the surface silicon to form  $\text{SiF}_4$ . An additional etching mechanism is ion bombardment. As accelerated ions hit the sample surface, they can cause lattice defects that make atoms easier to remove, or physically knock out atoms. When chemical reactions are the primary source of etching, the process is called plasma etching. When ion bombardment is the primary mechanism, the process is called reactive ion etching.

Below are the recipes used to thin silicon nitride and clean carbon contamination from samples.

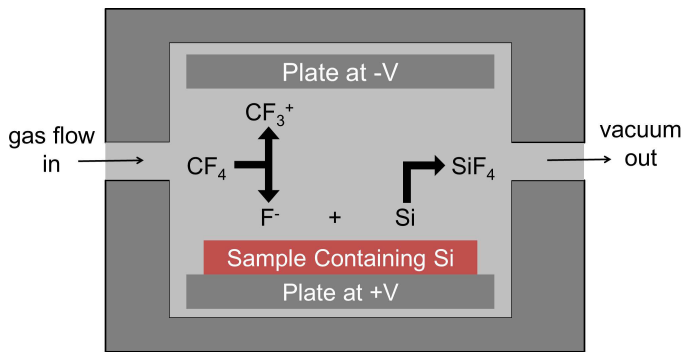


Figure 5.2.1: Schematic of the plasma etching process. Gas flows into a chamber containing two parallel plates at high bias. The sample is placed on one of the plates. The bias ionizes the gas, and pulls the charged ions towards the plates. The ions pulled toward the sample adsorb on the sample and react with it to form volatile compounds. These compounds desorb from the sample and are removed from the chamber with a vacuum pump.

Etcher Used	Oxford Plasmalab 80+	Technics PEII	Technics PEII-A
Material Etched	$\text{SiN}_x$	$\text{SiN}_x$	$\text{SiN}_x$
Gas Used	$\text{CHF}_3, \text{O}_2$	$\text{SF}_6$	$\text{SF}_6$
Vacuum Pressure	20 mTorr	400 mTorr	50 mTorr
Gas Flow	50 sccm, 5 sccm	n/a	n/a
Gas Pressure	n/a	150 mTorr	350 mTorr
Power (W)	150	50	50
Etch Rate	1 nm/s	1.4 nm/s	0.3 nm/s

Table 5.2: Recipes for plasma etching of silicon nitride

Etcher Used	Technics PEII	Gatan Solarus 950
Material Etched	graphene	cleaning
Gas Used	$\text{O}_2$	$\text{O}_2$
Vacuum Pressure	50 mTorr	70 mTorr
Gas Flow	n/a	27.5 sccm
Gas Pressure	150 mTorr	n/a
Power (W)	50	50

Table 5.3: Recipes for plasma etching of organics

## 5.3 STEM Thinning

In scanning transmission electron microscopy, the condensed beam of a TEM is rastered across a sample to generate an image. The image can either be composed of electrons that pass through the membrane without interacting with it (light-field mode) or electrons that interact with the membrane and are deflected (dark-field mode). In the first case, denser or thicker materials will appear darker in the image because fewer electrons passed through the material without interacting. In the latter case, denser or thicker materials appear lighter in the image because more electrons were deflected off of the sample.

STEM thinning relies on a high dose of high energy electrons to cause knock-on damage to the membrane, which slowly thins the material. Simply put, the electron energy is high enough to overcome the energy barrier required to remove atoms from the membrane. By setting the beam intensity high enough, atoms can be removed from the sample during STEM rastering.

Nitrogen is a lighter element (atomic number seven) than silicon (atomic number fourteen) and thus has a lower knock out energy. Due to this effect, nitrogen is preferentially removed from the thinned region and membranes thinned using this method have thinned areas composed primarily of silicon.

Below is the recipe used to thin samples during the course of this work.

TEM Used	JEOL 2010F
Accelerating Voltage	200kV
Aperture Diameter	70 $\mu\text{m}$
Electron Beam Diameter	1.0 nm
Mode	EELS1
Condenser 1 Setting Modification	3.66
Condenser 3 Setting Modification	4.87
Magnification	4 Mx
Field Size	20 nm
Image Dimensions	256 x 256 pixels
Pixel Dwell Time	20 $\mu\text{s}$
Electron Beam Dose	890 kAs/cm <sup>3</sup>

Table 5.4: TEM settings for STEM thinning of silicon nitride membranes

## 5.4 Atomic Layer Deposition

Atomic layer deposition (ALD) is used to create very thin, conformal layers of material on a sample. ALD works by adding alternating gaseous reactive materials to a vacuum chamber. As the first material is pumped into the chamber, it adsorbs onto the sample surface and reacts. Using developed surface chemistries and recipes, the first molecule will adsorb to the sample surface, but not onto itself. This creates a single atomic layer of the first molecules reactant. As an example, take atomic layer deposition of aluminum oxide ( $\text{Al}_2\text{O}_3$ ) onto silicon. This process is diagrammed in Figure 5.4.1. The first molecule pumped into the vacuum chamber is water vapor, which reacts with the silicon substrate to form  $\text{OH}^-$  groups on the surface, but water molecules will not bind or react with  $\text{OH}^-$  groups. Once a complete atomic layer of the first material is formed, the chamber is pumped and the second material is added, and

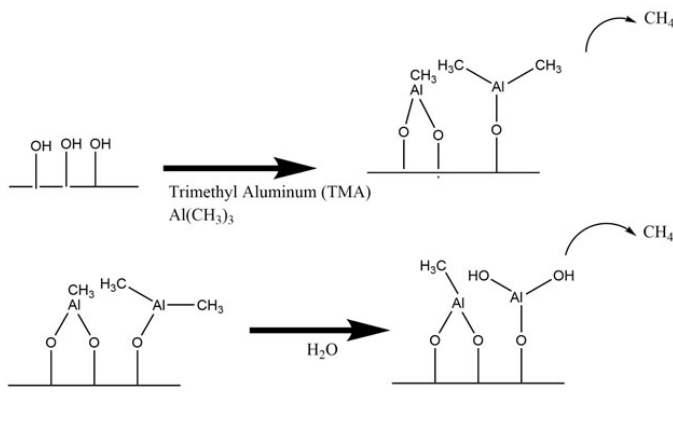
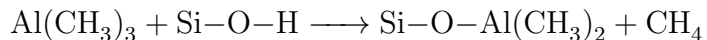


Figure 5.4.1: Diagram of the growth procedure in ALD. Each time TMA is introduced to a surface coated with  $\text{OH}^-$  groups, it adsorbs and reacts, releasing  $\text{CH}_4$  molecules. Each time water vapor is introduced to a surface coated with methyl groups, it adsorbs and reacts, releasing  $\text{CH}_4$  molecules. Image credit: User: Mcat chem446 / Wikimedia Commons / CC-BY-SA-3.0

the molecule is once again chosen to adsorb and react with the first molecule, but not itself. In this example, trimethyl aluminum (TMA,  $\text{Al}(\text{CH}_3)_3$ ) is added to the chamber. TMA attaches to an  $\text{OH}^-$  group and releases a methane molecule in the following reaction:



However, TMA will not bind or react with the bound aluminum molecules or methyl groups. Another complete atomic layer is formed, and the system is again pumped. When the first molecule is again added to the system, it reacts with the new surface, and the process cycles. In this example,  $\text{OH}^-$  groups from the water vapor replace methyl groups on the aluminum surface, creating a new surface of  $\text{OH}^-$  for the TMA to react with. The process is cycled until the desired thickness is reached.

Below is the recipe used to deposit  $\text{TiO}_2$  on graphene.

ALD tool used	Cambridge Nanotech Savannah 200 ALD
Material deposited	TiO <sub>2</sub>
Substrate material	graphene (C)
Precursor 1	Ti(NMe <sub>2</sub> ) <sub>4</sub>
Precursor 2	H <sub>2</sub> O
Temperature	200°C
Pulse time for Precursor 1	0.1 s
Pulse time for precursor 2	0.015 s
Vacuum pump time	10 s

Table 5.5: Recipe for Atomic Layer Deposition of TiO<sub>2</sub>

## 5.5 Chemical Vapor Deposition

Chemical vapor deposition (CVD) was used in this work to create large-area graphene sheets on copper substrates. CVD works on similar principles as ALD, with a few modifications. In CVD graphene growth on copper, methane gas flows through a tube containing the copper substrate at high temperature. The methane adsorbs onto the copper, which acts as a catalyst for methane decomposition. As each methane molecule decomposes, the hydrogen atoms bind to form H<sub>2</sub> gas and are carried out of the tube by the gas flow. The carbon atoms stay adsorbed on the copper surface and self-align to form a graphene sheet. The copper foil can then be dissolved in iron chloride, leaving a floating graphene sheet behind. Hydrogen can be added to the methane to alter the concentration of hydrogen gas and thus the growth rate, and Argon can be added to increase the tube pressure using an inert gas.

Below is the recipe used to create graphene sheets using a Thermo Scientific Lindberg Blue M CVD oven with a 1" diameter quartz tube.

Step	Temperature	CH <sub>4</sub> flow	Ar flow	H <sub>2</sub> flow	Duration
Purging nitrogen	25°C	35 sccm	600 sccm	500 sccm	8 min
Purging methane	25°C	0 sccm	600 sccm	500 sccm	2 min
Annealing copper	900°C	0 sccm	600 sccm	500 sccm	10 min
Graphene growth	1000°C	35 sccm	0 sccm	1000 sccm	10 min

Table 5.6: Recipe for Chemical Vapor Deposition of graphene using a Thermo Scientific Lindberg M oven

# Bibliography

- [1] J. Aarik, A. Aidla, T. Uustare, K. Kukli, V. Sammelselg, M. Ritala, and M. Leskela. Atomic layer deposition of TiO<sub>2</sub> thin films from TiI<sub>4</sub> and H<sub>2</sub>O. *Applied Surface Science*, 193(1-4):277–286, JUN 5 2002.
- [2] M. Akeson, D. Branton, J. J. Kasianowicz, E. Brandin, and D. W. Deamer. Microsecond time-scale discrimination among polycytidylic acid, polyadenylic acid, and polyuridylic acid as homopolymers or as segments within single RNA molecules. *Biophysical Journal*, 77(6):3227–3233, DEC 1999.
- [3] A. Aksimentiev, J. B. Heng, G. Timp, and K. Schulten. Microscopic kinetics of DNA translocation through synthetic nanopores. *Biophysical Journal*, 87:2086, 2004.
- [4] Y. Astier, O. Braha, and H. Bayley. Toward single molecule DNA sequencing: Direct identification of ribonucleoside and deoxyribonucleoside 5'-monophosphates by using an engineered protein nanopore equipped with a molecular adapter. *Journal of the American Chemical Society*, 128(5):1705–1710, FEB 8 2006.
- [5] L. Bacri, A. G. Oukhaled, B. Schiedt, G. Patriarche, E. Bourhis, J. Gierak,

- J. Pelta, and L. Auvray. Dynamics of colloids in single solid-state nanopores. *Journal of Physical Chemistry B*, 115(12):2890–2898, MAR 31 2011.
- [6] G. K. Batchelor. *An introduction to fluid dynamics*. Cambridge University Press, 2000.
- [7] G. Bellapadrona, A. B. Tesler, D. Gruenstein, L. H. Hossain, R. Kikkeri, P. H. Seeberger, A. Vaskevich, and I. Rubinstein. Optimization of localized surface plasmon resonance transducers for studying carbohydrate-protein interactions. *Analytical Chemistry*, 84(1):232–240, JAN 3 2012.
- [8] J. Bjerrum. *Stability constants of metal-ions complexes, with solubility products of inorganic substances*. The Chemical Society, 1957.
- [9] A. Bouchet, E. Descamps, P. Mailley, T. Livache, F. Chatelain, and V. Haguet. Contactless electrofunctionalization of a single pore. *Small*, 5(20):2297–2303, OCT 16 2009.
- [10] D. Branton, D. W. Deamer, A. Marziali, H. Bayley, S. A. Benner, T. Butler, M. Di Ventra, S. Garaj, A. Hibbs, X. Huang, S. B. Jovanovich, P. S. Krstic, S. Lindsay, X. S. Ling, C. H. Mastrangelo, A. Meller, J. S. Oliver, Y. V. Pershin, J. M. Ramsey, R. Riehn, G. V. Soni, V. Tabard-Cossa, M. Wanunu, M. Wiggin, and J. A. Schloss. The potential and challenges of nanopore sequencing. *Nature Biotechnology*, 26(10):1146–1153, OCT 2008.
- [11] M. Brust, M. Walker, D. Bethell, D. J. Schiffrian, and R. Whyman. Synthesis of

- thiol-derivatized gold nanoparticles in a 2-phase liquid-liquid system. *Journal of the Chemical Society - Chemical Communications*, (7):801–802, APR 7 1994.
- [12] T. Z. Butler, M. Pavlenok, I. M. Derrington, M. Niederweis, and J. H. Gundlach. Single-molecule DNA detection with an engineered MspA protein nanopore. *Proceedings of the National Academy of Sciences of the United States of America*, 105(52):20647–20652, DEC 30 2008.
- [13] E. Campos, C. E. McVey, R. P. Carney, F. Stellacci, Y. Astier, and J. Yates. Sensing single mixed-monolayer protected gold nanoparticles by the alpha-hemolysin nanopore. *Analytical Chemistry*, 85(21):10149–10158, NOV 5 2013.
- [14] S. Chang, S. Huang, J. He, F. Liang, P. Zhang, S. Li, X. Chen, O. Sankey, and S. Lindsay. Electronic signatures of all four DNA nucleosides in a tunneling gap. *Nano Letters*, 10(3):1070–1075, MAR 2010.
- [15] P. Chen, J. J. Gu, E. Brandin, Y. R. Kim, Q. Wang, and D. Branton. Probing single DNA molecule transport using fabricated nanopores. *Nano Letters*, 4(11):2293–2298, NOV 2004.
- [16] P. Chen, T. Mitsui, D. B. Farmer, J. Golovchenko, R. G. Gordon, and D. Branton. Atomic layer deposition to fine-tune the surface properties and diameters of fabricated nanopores. *Nano Letters*, 4(7):1333–1337, JUL 2004.
- [17] G. M. Cherf, K. R. Lieberman, H. Rashid, C. E. Lam, K. Karplus, and M. Ake-

- son. Automated forward and reverse ratcheting of DNA in a nanopore at 5-angstrom precision. *Nature Biotechnology*, 30(4):344–348, APR 2012.
- [18] S. Cho, Y. F. Chen, and M. S. Fuhrer. Gate-tunable graphene spin valve. *Applied Physics Letters*, 91(12), SEP 17 2007.
- [19] J. Clarke, H. C. Wu, L. Jayasinghe, A. Patel, S. Reid, and H. Bayley. Continuous base identification for single-molecule nanopore DNA sequencing. *Nature Nanotechnology*, 4(4):265–270, APR 2009.
- [20] J. Comer, V. Dimitrov, Q. Zhao, G. Timp, and A. Aksimentiev. Microscopic mechanics of hairpin DNA translocation through synthetic nanopores. *Biophysical Journal*, 96(2):593–608, JAN 21 2009.
- [21] W.H. Coulter and W. R. Hogg. Apparatus and method for measuring a dividing particle size of a particulate system. *US Patent*, 3557352, 1971.
- [22] H. G. Craighead and G. A. Niklasson. Characterization and optical properties of arrays of small gold particles. *Applied Physics Letters*, 44(12):1134–1136, 1984.
- [23] B. Cressiot, A. Oukhaled, G. Patriarche, M. Pastoriza-Gallego, J. M. Betton, L. Auvray, M. Muthukumar, L. Bacri, and J. Pelta. Protein transport through a narrow solid-state nanopore at high voltage: Experiments and theory. *ACS Nano*, 6(7):6236–6243, JUL 2012.

- [24] M. De, P. S. Ghosh, and V. M. Rotello. Applications of nanoparticles in biology. *Advanced Materials*, 20(22):4225–4241, NOV 18 2008.
- [25] D. W. Deamer and M. Akeson. Nanopores and nucleic acids: prospects for ultrarapid sequencing. *Trends in Biotechnology*, 18(4):147–151, APR 2000.
- [26] D. W. Deamer and D. Branton. Characterization of nucleic acids by nanopore analysis. *Accounts of Chemical Research*, 35(10):817–825, OCT 2002.
- [27] C. Dekker. Solid-state nanopores. *Nature Nanotechnology*, 2(4):209–215, APR 2007.
- [28] A. V. Delgado, F. Gonzalez-Caballero, R. J. Hunter, L. K. Koopal, and J. Lykema. Measurement and interpretation of electrokinetic phenomena. *Journal of Colloid and Interface Science*, 309(2):194–224, MAY 15 2007. International Electrokinetics Conference (Elkin), Nancy, FRANCE, JUN 25-29, 2006.
- [29] I. M. Derrington, T. Z. Butler, M. D. Collins, E. Manrao, M.l Pavlenok, M. Niederweis, and J. H. Gundlach. Nanopore DNA sequencing with MspA. *Proceedings of the National Academy of Sciences of the United States of America*, 107(37):16060–16065, SEP 14 2010.
- [30] O. K. Dudko, J. Mathe, A. Szabo, A. Meller, and G. Hummer. Extracting kinetics from single-molecule force spectroscopy: Nanopore unzipping of DNA hairpins. *Biophysical Journal*, 92(12):4188–4195, JUN 2007.

- [31] M. Faller, M. Niederweis, and G. E. Schulz. The structure of a mycobacterial outer-membrane channel. *Science*, 303(5661):1189–1192, FEB 20 2004.
- [32] M. Firnkes, D. Pedone, J. Knezevic, M. Doeblinger, and U. Rant. Electrically facilitated translocations of proteins through silicon nitride nanopores: Conjoint and competitive action of diffusion, electrophoresis, and electroosmosis. *Nano Letters*, 10(6):2162–2167, JUN 2010.
- [33] M. D. Fischbein and M. Drndić. Sub-10 nm device fabrication in a transmission electron microscope. *Nano Letters*, 7(5):1329–1337, MAY 2007.
- [34] M. D. Fischbein and M. Drndić. Electron beam nanosculpting of suspended graphene sheets. *Applied Physics Letters*, 93(11), SEP 15 2008.
- [35] D. Fologea, M. Gershow, B. Ledden, D. S. McNabb, J. A. Golovchenko, and J. L. Li. Detecting single stranded DNA with a solid state nanopore. *Nano Letters*, 5(10):1905–1909, OCT 2005.
- [36] J. L. Fraikin, T. Teesalu, C. M. McKenney, E. Ruoslahti, and A. N. Cleland. A high-throughput label-free nanoparticle analyser. *Nature Nanotechnology*, 6(5):308–313, MAY 2011.
- [37] W. Gotschy, K. Vonmetz, A. Leitner, and F. R. Aussenegg. Thin films by regular patterns of metal nanoparticles: Tailoring the optical properties by nanodesign. *Applied Physics B - Lasers and Optics*, 63(4):381–384, OCT 1996.

- [38] G. Goyal, K. J. Freedman, and M. J. Kim. Gold nanoparticle trans location dynamics and electrical detection of single particle diffusion using solid-state nanopores. *Analytical Chemistry*, 85(17):8180–8187, SEP 3 2013.
- [39] M. E. Gracheva, D. V. Melnikov, and J. P. Leburton. Multilayered semiconductor membranes for nanopore ionic conductance modulation. *ACS Nano*, 2(11):2349–2355, NOV 2008.
- [40] M. E. Gracheva, J. Vidal, and J. P. Leburton. P-n semiconductor membrane for electrically tunable ion current rectification and filtering. *Nano Letters*, 7(6):1717–1722, JUN 2007.
- [41] P. Guo, C. R. Martin, Y. Zhao, J. Ge, and R. N. Zare. General method for producing organic nanoparticles using nanoporous membranes. *Nano Letters*, 10(6):2202–2206, JUN 2010.
- [42] A. R. Hall, J. M. Keegstra, M. C. Duch, M. C. Hersam, and C. Dekker. Translocation of single-wall carbon nanotubes through solid-state nanopores. *Nano Letters*, 11(6):2446–2450, JUN 2011.
- [43] K. M. Halverson, R. G. Panchal, T. L. Nguyen, R. Gussio, S. F. Little, M. Misakian, S. Bavari, and J. J. Kasianowicz. Anthrax biosensor, protective antigen ion channel asymmetric blockade. *Journal of Biological Chemistry*, 280(40):34056–34062, OCT 7 2005.
- [44] G. Han, P. Ghosh, and V. M. Rotello. Functionalized gold nanoparticles for drug

- delivery. *Nanomedicine*, 2(1):113–123, FEB 2007. Symposium on Advances in Nanomedicine held at the 233rd National American-Chemical-Society Meeting, San Francisco, CA, SEP, 2006.
- [45] M. Y. Han, B. Oozyilmaz, Y. Zhang, and P. Kim. Energy band-gap engineering of graphene nanoribbons. *Physical Review Letters*, 98(20), MAY 18 2007.
- [46] A. Hashimoto, K. Suenaga, A. Gloter, K. Urita, and S. Iijima. Direct evidence for atomic defects in graphene layers. *Nature*, 430(7002):870–873, AUG 19 2004.
- [47] C. L. Haynes, A. D. McFarland, M. T. Smith, J. C. Hulteen, and R. P. Van Duyne. Angle-resolved nanosphere lithography: Manipulation of nanoparticle size, shape, and interparticle spacing. *Journal of Physical Chemistry B*, 106(8):1898–1902, FEB 28 2002.
- [48] K. Healy. Nanopore-based single-molecule DNA analysis. *Nanomedicine*, 2(4):459–481, AUG 2007.
- [49] J. B. Heng, A. Aksimentiev, C. Ho, P. Marks, Y. V. Grinkova, S. Sligar, K. Schulten, and G. Timp. Stretching DNA using the electric field in a synthetic nanopore. *Nano Letters*, 5(10):1883–1888, OCT 2005.
- [50] C. Ho, R. Qiao, J. B. Heng, A. Chatterjee, R. J. Timp, N. R. Aluru, and G. Timp. Electrolytic transport through a synthetic nanometer-diameter pore. *Proceedings of the National Academy of Sciences of the United States of America*, 102(30):10445–10450, JUL 26 2005.

- [51] F. N. Hooge. 1/f noise is no surface effect. *Physics Letters A*, A 29(3):139–&, 1969.
- [52] S. Howorka and Z. Siwy. Nanopore analytics: sensing of single molecules. *Chemical Society Reviews*, 38(8):2360–2384, 2009.
- [53] X. H. Huang, I. H. El-Sayed, W. Qian, and M. A. El-Sayed. Cancer cell imaging and photothermal therapy in the near-infrared region by using gold nanorods. *Journal of the American Chemical Society*, 128(6):2115–2120, FEB 15 2006.
- [54] J. C. Hulteen and R. P. Vanduyne. Nanosphere lithography - A materials general fabrication process for periodic particle array surfaces. *Journal of Vacuum Science and Technology A - Vacuum Surfaces and Films*, 13(3, 2):1553–1558, MAY-JUN 1995.
- [55] L. Innes, M. R. Powell, I. Vlassiouk, C. Martens, and Z. S. Siwy. Precipitation-induced voltage-dependent ion current fluctuations in conical nanopores. *Journal of Physical Chemistry C*, 114(18):8126–8134, MAY 13 2010.
- [56] T. Ito, L. Sun, and R. M. Crooks. Simultaneous determination of the size and surface charge of individual nanoparticles using a carbon nanotube-based coulter counter. *Analytical Chemistry*, 75(10):2399–2406, MAY 15 2003.
- [57] T. Ito, L. Sun, R. R. Henriquez, and R. M. Crooks. A carbon nanotube-based Coulter nanoparticle counter. *Accounts of Chemical Research*, 37(12):937–945, DEC 2004.

- [58] R. J. B. Kalescky, W. Shinoda, P. B. Moore, and S. O. Nielsen. Area per ligand as a function of nanoparticle radius: A theoretical and computer simulation approach. *Langmuir*, 25(3):1352–1359, 2009.
- [59] J. J. Kasianowicz, E. Brandin, D. Branton, and D. W. Deamer. Characterization of individual polynucleotide molecules using a membrane channel. *Proceedings of the National Academy of Sciences of the United States of America*, 93(24):13770–13773, NOV 26 1996.
- [60] J. J. Kasianowicz, J. W. F. Robertson, E. R. Chan, J. E. Reiner, and V. M. Stanford. Nanoscopic porous sensors. *Annual Review of Analytical Chemistry*, 1:737–766, 2008.
- [61] A. P. Kaushik and P. Clancy. Solvent-driven symmetry of self-assembled nanocrystal superlatticesa computational study. *Journal of Computational Chemistry*, 34:523, 2013.
- [62] R. Kawano, A. E. P. Schibel, C. Cauley, and H. S. White. Controlling the translocation of single-stranded DNA through alpha-hemolysin ion channels using viscosity. *Langmuir*, 25(2):1233–1237, JAN 20 2009.
- [63] U. F. Keyser. Controlling molecular transport through nanopores. *Journal of the Royal Society Interface*, 8(63):1369–1378, OCT 7 2011.
- [64] U. F. Keyser, B. N. Koeleman, S. Van Dorp, D. Krapf, R. M. M. Smeets, S. G.

- Lemay, N. H. Dekker, and C. Dekker. Direct force measurements on DNA in a solid-state nanopore. *Nature Physics*, 2(7):473–477, JUL 2006.
- [65] K. S. Kim, Y. Zhao, H. Jang, S. Y. Lee, J. M. Kim, K. S. Kim, J. H. Ahn, P. Kim, J. Y. Choi, and B. H. Hong. Large-scale pattern growth of graphene films for stretchable transparent electrodes. *Nature*, 457(7230):706–710, FEB 5 2009.
- [66] M. J. Kim, M. Wanunu, D. C. Bell, and A. Meller. Rapid fabrication of uniformly sized nanopores and nanopore arrays for parallel DNA analysis. *Advanced Materials*, 18(23):3149+, DEC 4 2006.
- [67] S. W. Kowalczyk, A. Y. Grosberg, Y. Rabin, and C. Dekker. Modeling the conductance and DNA blockade of solid-state nanopores. *Nanotechnology*, 22(31), AUG 5 2011.
- [68] S. W. Kowalczyk, A. R. Hall, and C. Dekker. Detection of local protein structures along DNA using solid-state nanopores. *Nano Letters*, 10(1):324–328, JAN 2010.
- [69] S. W. Kowalczyk, D. B. Wells, A. Aksimentiev, and C. Dekker. Slowing down DNA translocation through a nanopore in lithium chloride. *Nano Letters*, 12(2):1038–1044, FEB 2012.
- [70] D. Kozak, W. Anderson, R. Vogel, S. Chen, F. Antaw, and M. Trau. Simultaneous size and zeta-potential measurements of individual nanoparticles in

dispersion using size-tunable pore sensors. *ACS Nano*, 6(8):6990–6997, AUG 2012.

- [71] D. Krapf, M. Y. Wu, R. M. M. Smeets, H. W. Zandbergen, C. Dekker, and S. G. Lemay. Fabrication and characterization of nanopore-based electrodes with radii down to 2 nm. *Nano Letters*, 6(1):105–109, JAN 2006.
- [72] S. Kumar, C. Tao, M. Chien, B. Hellner, A. Balijepalli, J. W. F. Robertson, Z. Li, J. J. Russo, J. E. Reiner, J. J. Kasianowicz, and J. Ju. PEG-labeled nucleotides and nanopore detection for single molecule DNA sequencing by synthesis. *Scientific Reports*, 2, SEP 21 2012.
- [73] U. Landman and W. D. Luedtke. Small is different: energetic, structural, thermal, and mechanical properties of passivated nanocluster assemblies uzi landman. *Royal Society of Chemistry*, 125:1–22, 2004.
- [74] M. Langecker, V. Arnaut, T. G. Martin, J. List, S. Renner, M. Mayer, H. Dietz, and F. C. Simmel. Synthetic lipid membrane channels formed by designed DNA nanostructures. *Science*, 338(6109):932–936, NOV 16 2012.
- [75] J. Larkin, R. Y. Henley, M. Muthukumar, J. K. Rosenstein, and M. Wanunu. High-bandwidth protein analysis using solid-state nanopores. *Biophysical Journal*, 106(3):696–704, FEB 4 2014.
- [76] J. Li, D. Stein, C. McMullan, D. Branton, M. J. Aziz, and J. A. Golovchenko.

Ion-beam sculpting at nanometre length scales. *Nature*, 412(6843):166–169, JUL 12 2001.

- [77] J. L. Li, D. Folgea, R. Rollings, and B. Ledden. Characterization of protein unfolding with solid-state nanopores. *Protein and Peptide Letters*, 21(3):256–265, MAR 2014.
- [78] J. L. Li, M. Gershoff, D. Stein, E. Brandin, and J. A. Golovchenko. DNA molecules and configurations in a solid-state nanopore microscope. *Nature Materials*, 2(9):611–615, SEP 2003.
- [79] X. Li, W. Cai, J. An, S. Kim, J. Nah, D. Yang, R. Piner, A. Velamakanni, I. Jung, E. Tutuc, S. K. Banerjee, L. Colombo, and R. S. Ruoff. Large-area synthesis of high-quality and uniform graphene films on copper foils. *Science*, 324(5932):1312–1314, JUN 5 2009.
- [80] K. R. Lieberman, G. M. Cherf, M.l J. Doody, F. Olasagasti, Y. Kolodji, and M. Akeson. Processive replication of single DNA molecules in a nanopore catalyzed by phi29 DNA polymerase. *Journal of the American Chemical Society*, 132(50):17961–17972, DEC 22 2010.
- [81] K. R. Lieberman, J. M. Dahl, A. H. Mai, M. Akeson, and H. Wang. Dynamics of the translocation step measured in individual DNA polymerase complexes. *Journal of the American Chemical Society*, 134(45):18816–18823, NOV 14 2012.

- [82] K. Liu, Z. and Suenaga, P. J. F. Harris, and S. Iijima. Open and closed edges of graphene layers. *Physical Review Letters*, 102(1), JAN 9 2009.
- [83] X. Liu, J. G. Worden, Q. Huo, and J. R. Brennan. Kinetic study of gold nanoparticle growth in solution by Brust-Schiffrin reaction. *Journal of Nanoscience and Nanotechnology*, 6(4):1054–1059, APR 2006.
- [84] H. Lodish, A. Berk, C. A. Kaiser, M. Krieger, M. P. Scott, A. Bretscher, H. Ploegh, and P. Matsudaira. *Molecular cell biology*. W. H. Freeman and Company, 6 edition, 2008.
- [85] B. Lu, D. P. Hoogerheide, Q. Zhao, H. Zhang, Z. Tang, D. Yu, and J. A. Goloychenko. Pressure-controlled motion of single polymers through solid-state nanopores. *Nano Letters*, 13(7):3048–3052, JUL 2013.
- [86] B. Luan, D. Wang, R. Zhou, S. Harrer, H. Peng, and G. Stolovitzky. Dynamics of DNA translocation in a solid-state nanopore immersed in aqueous glycerol. *Nanotechnology*, 23(45), NOV 16 2012.
- [87] E. A. Manrao, I. M. Derrington, A. H. Laszlo, K. W. Langford, M. K. Hopper, N. Gillgren, M. Pavlenok, M. Niederweis, and J. H. Gundlach. Reading DNA at single-nucleotide resolution with a mutant MspA nanopore and phi29 DNA polymerase. *Nature Biotechnology*, 30(4):349–U174, APR 2012.
- [88] E. R. Mardis. A decade’s perspective on DNA sequencing technology. *Nature*, 470(7333):198–203, FEB 2011.

- [89] V. Marx. The genome jigsaw. *Nature*, 501(7466):263–268, SEPT 2013.
- [90] A. McMullen, H. W. de Hann, J. X. Tang, and D. Stein. Stiff filamentous virus translocations through solid-state nanopores. *Nature Communications*, 5(1):1–10, JUN 2014.
- [91] A. Meller and D. Branton. Single molecule measurements of DNA transport through a nanopore. *Electrophoresis*, 23(16):2583–2591, AUG 2002.
- [92] A. Meller, L. Nivon, E. Brandin, J. Golovchenko, and D. Branton. Rapid nanopore discrimination between single polynucleotide molecules. *Proceedings of the National Academy of Sciences of the United States of America*, 97(3):1079–1084, FEB 1 2000.
- [93] A. Meller, L. Nivon, and D. Branton. Voltage-driven DNA translocations through a nanopore. *Physical Review Letters*, 86(15):3435–3438, APR 9 2001.
- [94] C. A. Merchant, K. Healy, M. Wanunu, V. Ray, N. Peterman, J. Bartel, M. D. Fischbein, K. Venta, Z. Luo, A. T. C. Johnson, and M. Drndić. DNA translocation through graphene nanopores. *Nano Letters*, 10(8):2915–2921, AUG 2010.
- [95] J. C. Meyer, A. K. Geim, M. I. Katsnelson, K. S. Novoselov, T. J. Booth, and S. Roth. The structure of suspended graphene sheets. *Nature*, 446(7131):60–63, MAR 1 2007.
- [96] B. N. Miles, A. P. Ivanov, K. A. Wilson, F. Dogan, D. Japrung, and J. B. Edel.

- Single molecule sensing with solid-state nanopores: Novel materials, methods, and applications. *Chemical Society Reviews*, 42(1):15–28, 2013.
- [97] C. B. Murray, C. R. Kagan, and M. G. Bawendi. Synthesis and characterization of monodisperse nanocrystals and close-packed nanocrystal assemblies. *Annual Review of Materials Science*, 30:545–610, 2000.
- [98] S. W. Nam, M. J. Rooks, K. B. Kim, and S. M. Rossnagel. Ionic field effect transistors with sub-10 nm multiple nanopores. *Nano Letters*, 9(5):2044–2048, MAY 2009.
- [99] D. J. Niedzwiecki, R. Iyer, P. N. Borer, and L. Movileanu. Sampling a biomarker of the human immunodeficiency virus across a synthetic nanopore. *ACS Nano*, 7(4):3341–3350, APR 2013.
- [100] K. S. Novoselov, A. K. Geim, S. V. Morozov, D. Jiang, Y. Zhang, S. V. Dubonos, I. V. Grigorieva, and A. A. Firsov. Electric field effect in atomically thin carbon films. *Science*, 306(5696):666–669, OCT 22 2004.
- [101] National Institute of Health. National Human Genome Research Institute, 2010.
- [102] H. Ohshima. *Theory of colloid and interfacial electric phenomena*. Academic Press, 2006.
- [103] T. Ohshiro, K. Matsubara, M. Tsutsui, M. Furuhashi, M. Taniguchi, and T. Kawai. Single-molecule electrical random resequencing of DNA and RNA. *Scientific Reports*, 2, JUL 10 2012.

- [104] A. Oukhaled, B. Cressiot, L. Bacri, M. Pastoriza-Gallego, J. M. Betton, E. Bourhis, R. Jede, J. Gierak, L. Auvray, and J. Pelta. Dynamics of completely unfolded and native proteins through solid-state nanopores as a function of electric driving force. *ACS Nano*, 5(5):3628–3638, MAY 2011.
- [105] J. Polte, R. Erler, A. F. Thuenemann, S. Sokolov, T. T. Ahner, K. Rademann, F. Emmerling, and R. Krahnert. Nucleation and growth of gold nanoparticles studied via in situ small angle X-ray scattering at millisecond time resolution. *ACS Nano*, 4(2):1076–1082, FEB 2010.
- [106] H. W. C. Postma. Rapid sequencing of individual DNA molecules in graphene nanogaps. *Nano Letters*, 10(2):420–425, FEB 2010.
- [107] A. S. Prabhu, T. Z. N. Jubery, K. J. Freedman, R. Mulero, P. Dutta, and M. J. Kim. Chemically modified solid state nanopores for high throughput nanoparticle separation. *Journal of Physics - Condensed Matter*, 22(45), NOV 17 2010.
- [108] E. Rabani. Structure and electrostatic properties of passivated cdse nanocrystals. *Journal of Chemical Physics*, 115:1493–1497, 2001.
- [109] J. E. Reiner, A. Balijepalli, J. W. F. Robertson, J. Campbell, J. Suehle, and J. J. Kasianowicz. Disease detection and management via single nanopore-based sensors. *Chemical Reviews*, 112(12):6431–6451, DEC 2012.
- [110] J. E. Reiner, J. J. Kasianowicz, B. J. Nablo, and J. W. F. Robertson. Theory

- for polymer analysis using nanopore-based single-molecule mass spectrometry. *Proceedings of the National Academy of Sciences of the United States of America*, 107(27):12080–12085, JUL 6 2010.
- [111] F. J. Richards. A flexible growth function for empirical use. *Journal of Experimental Botany*, 10(29):290–300, 1959.
- [112] K. Robbie and M. J. Brett. Sculptured thin films and glancing angle deposition: Growth mechanics and applications. *Journal of Vacuum Science and Technology A - Vacuum Surfaces and Films*, 15(3, 2):1460–1465, MAY-JUN 1997. 43rd American-Vacuum-Society Symposium, PHILADELPHIA, PA, OCT 14-18, 1996.
- [113] J. W. F. Robertson, C. G. Rodrigues, V. M. Stanford, K. A. Rubinson, O. V. Krasilnikov, and J. J. Kasianowicz. Single-molecule mass spectrometry in solution using a solitary nanopore. *Proceedings of the National Academy of Sciences of the United States of America*, 104(20):8207–8211, MAY 15 2007.
- [114] J. K. Rosenstein, M. Wanunu, C. A. Merchant, M. Drndić, and K. L. Shepard. Integrated nanopore sensing platform with sub-microsecond temporal resolution. *Nature Methods*, 9(5):487–U112, MAY 2012.
- [115] F. Sanger, S. Nicklen, and A. R. Coulson. DNA sequencing with chain-terminating inhibitors. *Proceedings of the National Academy of Sciences of the United States of America*, 74(12):5463–5467, 1977.

- [116] R. Sharabani, S. Reuveni, G. Noy, E. Shapira, S. Sadeh, and Y. Selzer. Fabrication of very high aspect ratio metal nanowires by a self-propulsion mechanism. *Nano Letters*, 8(4):1169–1173, APR 2008.
- [117] F. J. Sigworth. Electronic design of the patch clamp. In B. Sakmann and E. Neher, editors, *Single Channel Recording*. Springer, 2009.
- [118] J. M. Simmons, B. M. Nichols, S. E. Baker, M. S. Marcus, O. M. Castellini, C. S. Lee, R. J. Hamers, and M. A. Eriksson. Effect of ozone oxidation on single-walled carbon nanotubes. *Journal of Physical Chemistry B*, 110(14):7113–7118, APR 13 2006.
- [119] G. M. Skinner, M. van den Hout, O. Broekmans, C. Dekker, and N. H. Dekker. Distinguishing single- and double-stranded nucleic acid molecules using solid-state nanopores. *Nano Letters*, 9(8):2953–2960, AUG 2009.
- [120] R. M. M. Smeets, U. F. Keyser, N. H. Dekker, and C. Dekker. Noise in solid-state nanopores. *Proceedings of the National Academy of Sciences of the United States of America*, 105(2):417–421, JAN 15 2008.
- [121] R. M. M. Smeets, U. F. Keyser, D. Krapf, M. Y. Wu, N. H. Dekker, and C. Dekker. Salt dependence of ion transport and DNA translocation through solid-state nanopores. *Nano Letters*, 6(1):89–95, JAN 2006.
- [122] R. M. M. Smeets, U. F. Keyser, M. Y. Wu, N. H. Dekker, and C. Dekker.

Nanobubbles in solid-state nanopores. *Physical Review Letters*, 97(8), AUG 25 2006.

- [123] L. Z. Song, M. R. Hobaugh, C. Shustak, S. Cheley, H. Bayley, and J. E. Gouaux. Structure of staphylococcal alpha-hemolysin, a heptameric transmembrane pore. *Science*, 274(5294):1859–1866, DEC 13 1996.
- [124] J. Sonnefeld. Determination of surface charge density parameters of silicon nitride. *Colloids and Surfaces A - Physicochemical and Engineering Aspects*, 108(1):27–31, MAR 8 1996.
- [125] A. J. Storm, J. H. Chen, X. S. Ling, H. W. Zandbergen, and C. Dekker. Fabrication of solid-state nanopores with single-nanometre precision. *Nature Materials*, 2(8):537–540, AUG 2003.
- [126] A. J. Storm, J. H. Chen, H. W. Zandbergen, and C. Dekker. Translocation of double-strand DNA through a silicon oxide nanopore. *Physical Review E*, 71(5, 1), MAY 2005.
- [127] A. J. Storm, C. Storm, J. H. Chen, H. Zandbergen, J. F. Joanny, and C. Dekker. Fast DNA translocation through a solid-state nanopore. *Nano Letters*, 5(7):1193–1197, JUL 2005.
- [128] S. H. Sun, C. B. Murray, D. Weller, L. Folks, and A. Moser. Monodisperse FePt nanoparticles and ferromagnetic FePt nanocrystal superlattices. *Science*, 287(5460):1989–1992, MAR 17 2000.

- [129] B. Tinland, A. Pluen, J. Sturm, and G. Weill. Persistence length of single-stranded DNA. *Macromolecules*, 30(19):5763–5765, SEP 22 1997.
- [130] E. H. Trepagnier, A. Radenovic, D. Sivak, P. Geissler, and J. Liphardt. Controlling DNA capture and propagation through artificial nanopores. *Nano Letters*, 7(9):2824–2830, SEP 2007.
- [131] M. van den Hout, A. R. Hall, M. Y. Wu, H. W. Zandbergen, C. Dekker, and N. H. Dekker. Controlling nanopore size, shape and stability. *Nanotechnology*, 21(11), MAR 19 2010.
- [132] B. M. Venkatesan and R. Bashir. Nanopore sensors for nucleic acid analysis. *Nature Nanotechnology*, 6(10):615–624, OCT 2011.
- [133] B. M. Venkatesan, B. Dorvel, S. Yemenicioglu, N. Watkins, I. Petrov, and R. Bashir. Highly sensitive, mechanically stable nanopore sensors for DNA analysis. *Advanced Materials*, 21(27):2771+, JUL 20 2009.
- [134] B. M. Venkatesan, A. B. Shah, J. M. Zuo, and R. Bashir. DNA sensing using nanocrystalline surface-enhanced  $\text{Al}_2\text{O}_3$  nanopore sensors. *Advanced Functional Materials*, 20(8):1266–1275, APR 23 2010.
- [135] K. Venta, G. Shemer, M. Puster, J. A. Rodriguez-Manzo, A. Balan, J. K. Rosenstein, K. Shepard, and M. Drndić. Differentiation of short, single-stranded DNA homopolymers in solid-state nanopores. *ACS Nano*, 7(5):4629–4636, MAY 2013.

- [136] K. Venta, M. Wanunu, and M. Drndić. Electrically controlled nanoparticle synthesis inside nanopores. *Nano Letters*, 13(2):423–429, FEB 2013.
- [137] D. M. Vlassarev and J. A. Golovchenko. Trapping DNA near a solid-state nanopore. *Biophysical Journal*, 103:352–356, 2012.
- [138] R. Wang, K. Hashimoto, A. Fujishima, M. Chikuni, E. Kojima, A. Kitamura, M. Shimohigoshi, and T. Watanabe. Light-induced amphiphilic surfaces. *Nature*, 388(6641):431–432, JUL 31 1997.
- [139] S. Wang, Y. Zhang, N. Abidi, and L. Cabrales. Wettability and surface free energy of graphene films. *Langmuir*, 25(18):11078–11081, SEP 15 2009.
- [140] M. Wanunu. Nanopores: Past, present and future. *Physics of Life Reviews*, 9(2):174–176, JUN 2012.
- [141] M. Wanunu, S. Bhattacharya, Y. Xie, Y. Tor, A. Aksimentiev, and M. Drndić. Nanopore analysis of individual RNA/antibiotic complexes. *ACS Nano*, 5(12):9345–9353, DEC 2011.
- [142] M. Wanunu, T. Dadash, V. Ray, J. Jin, L. McReynolds, and M. Drndić. Rapid electronic detection of probe-specific microRNAs using thin nanopore sensors. *Nature Nanotechnology*, 5(11):807–814, NOV 2010.
- [143] M. Wanunu, W. Morrison, Y. Rabin, A. Y. Grosberg, and A. Meller. Electrostatic focusing of unlabelled DNA into nanoscale pores using a salt gradient. *Nature Nanotechnology*, 5(2):160–165, FEB 2010.

- [144] M. Wanunu, J. Sutin, B. McNally, A. Chow, and A. Meller. DNA translocation governed by interactions with solid-state nanopores. *Biophysical Journal*, 95(10):4716–4725, NOV 15 2008.
- [145] R. Weast. *CRC handbook of chemistry and physics*. Chemical Rubber Company, 53rd edition, 1972.
- [146] R. Wei, T. G. Martin, U. Rant, and H. Dietz. DNA origami gatekeepers for solid-state nanopores. *Angewandte Chemie - International Edition*, 51(20):4864–4867, 2012.
- [147] M. T. Wolfram, M. Burger, and Z. S. Siwy. Mathematical modeling and simulation of nanopore blocking by precipitation. *Journal of Physics - Condensed Matter*, 22(45), NOV 17 2010.
- [148] X. Ye, L. Jin, H. Caglayan, J. Chen, G. Xing, C. Zheng, Vicky D. N., Y. Kang, N. Engheta, C. R. Kagan, and C. B. Murray. Improved size-tunable synthesis of monodisperse gold nanorods through the use of aromatic additives. *ACS Nano*, 6(3):2804–2817, MAR 2012.
- [149] L. H. Yeh, M. Zhang, S. W. Joo, and S. Qian. Slowing down DNA translocation through a nanopore by lowering fluid temperature. *Electrophoresis*, 33(23, SI):3458–3465, DEC 2012.
- [150] M. B. Zanjani and J. R. Lukes. Size dependent elastic moduli of CdSe nanocrystals. *Journal of Nanoparticle Research*, 14(1), FEB 2012.

- tal superlattices predicted from atomistic and coarse grained models. *Journal of Chemical Physics*, 139:144702, 2013.
- [151] M. B. Zanjani and J. R. Lukes. Phonon dispersion and thermal conductivity of nanocrystal superlattices using three-dimensional atomistic models. *Journal of Applied Physics*, 115:143515, 2014.
- [152] Y. Zhang and H. J. Dai. Formation of metal nanowires on suspended single-walled carbon nanotubes. *Applied Physics Letters*, 77(19):3015–3017, NOV 6 2000.
- [153] Q. Zhao, J. Comer, V. Dimitrov, S. Yemenciooglu, A. Aksimentiev, and G. Timp. Stretching and unzipping nucleic acid hairpins using a synthetic nanopore. *Nucleic Acids Research*, 36(5):1532–1541, MAR 2008.
- [154] M. Zwolak and M. Di Ventra. Electronic signature of DNA nucleotides via transverse transport. *Nano Letters*, 5(3):421–424, MAR 2005.